Stress evolution during growth of InAs on GaAs measured by an in-situ cantilever beam setup

DISSERTATION

zur Erlangung des akademischen Grades
doctor rerum naturalium
(Dr. rer. nat.)
im Fach Physik

eingereicht an der
Mathematisch-Naturwissenschaftlichen Fakultät I
Humboldt-Universität zu Berlin

von
Frau M.Sc. Dongzhi Hu
geboren am 2.10.1971 in Qixiaying, Inner Mongolia, China

Präsident der Humboldt-Universität zu Berlin:
Prof. Dr. Christoph Markschies

Dekan der Mathematisch-Naturwissenschaftlichen Fakultät I:
Prof. Dr. Christian Limberg

Gutachter:

1. Prof. Dr. Klaus H. Ploog
2. Prof. Dr. W. Ted Masselink
3. Prof. Dr. Eric Tournié

eingereicht am: 31. August 2006
Tag der mündlichen Prüfung: 13. Februar 2007

Zusammenfassung

Der Einfluss der Verspannung während des Wachstums von InAs auf GaAs mittels Molekularstrahlepitaxie wird in dieser Arbeit untersucht. Eine Biegebalkenapparatur wurde benutzt, um den Verlauf der Filmkraft während des Wachstums und dem nachfolgenden Anlassen bei Wachstumstemperaturen zu messen. Die Steigung in einer Darstellung von Filmkraft gegen Filmdicke ist gleich der Verspannung, die sich während des heteroepitaktischen Wachstums bildet. Filmkraft-Kurven wurden während des InAs Wachstums unter As-reichen und In-reichen Bedingungen gemessen. Das Wachstum unter As-reichen Bedingungen verläuft im Stranski-Krastanov Modus, d. h. es bilden sich Quantenpunkte auf einer Benetzungsschicht. Bei nachfolgenden Wachstumsunterbrechungen oder absichtlichen Anlassprozeduren bei der Wachstumstemperatur reifen die Quantenpunkte. Um den Einfluss der Verspannung auf den Wachstumsprozess zu verstehen wurden die Filmkraft-Kurven analysiert und mit den morphologischen Veränderungen während des Wachstums und des Anlassens korreliert. Dieses wurde durch die Entwicklung von neuen Modellen für den Verlauf der Filmkraft erreicht.

Während des Wachstums von InAs auf GaAs(001) unter As-reichen Bedingungen zeigt die Filmkraft eine lineare Steigung bis zu einem Wert von 2.3 N/m. Dieser lineare Verlauf entspricht dem Aufdampfen der Benetzungsschicht (WL). Nach Erreichen der kritischen Schichtdicke von ca 1.5-1.6 Monolagen verläuft die Filmkraft mit geringerer Steigung, was auf einen Abbau der Verspannung durch das Auftreten von Quantenpunkten hindeutet. Werden die Quantenpunkte nachfolgend angelassen, nimmt die Filmkraft wieder ab was durch Reifung der QDs und durch Desorption von InAs hervorgerufen wird. Modelle wurden entwickelt um die Filmkraft-Kurven, die während des Anlassens gemessen wurden, anzupassen.

Die Quantenpunkte reifen unter Standard-Ostwald-Bedingungen für Temperaturen unterhalb 470 °C. Verschiedene Mechanismen, die z.B. kinetisch oder diffusiv limitiert sein können, bestimmen den Reifungsprozess. Die Filmkraft-Relaxationskurven wurden mit Modellen basierend auf solchen Mechanismen angepasst. Es zeigt sich, dass die Relaxationskurve, aufgenommen bei 440 °C, eigentlich durch alle Modelle relativ gut beschrieben werden kann. Allerdings liefert die Anpassung eines Modells, das durch Diffusion entlang der Quantenpunktoberfläche limitiert ist, das beste Resultat. Die Relaxationskurven gemessen bei 455 °C und 470 °C können jedoch nur gut durch ein Modell angepasst werden, in dem die Reifung durch Anlagerung/Ablagerung von Atomen an der Quantenpunktoberfläche limitiert ist.

Beim Anlassen bei höheren Temperaturen zeigt sich ein anderes Verhalten. Die Verspannung der Quantenpunkte baut sich auf Werte unterhalb der Verspannung ab, die durch das Aufbringen der Benetzungsschicht entstanden ist. Rasterkraftmikroskop-Aufnahmen zeigen, dass die Quantenpunkte zuerst reifen und sich dann nach ca. 450 s - 600 s wieder auflösen. Diese Beobachtungen werden durch eine Kombination von In-Desorption und In-Ga Interdiffusion erklärt. Photolumineszenzaufnahmen von Quantenpunkten, hergestellt bei verschiedenen Anlasszeiten, bestätigen diese Erklärung.
Im Unterschied zum Wachstum unter As-reichen Bedingungen führt das Wachstum unter In-reichen Bedingungen nicht zur Ausbildung von Quantenpunkten sondern verläuft im Lagenwachstumsmodus. Filmkraft-Kurven wurden ebenfalls unter diesen Bedingungen gemessen und zeigen, wie erwartet, eine deutliche Abweichungen von Kurven, die während des Stranski-Krastanov-Wachstums gemessen wurden. Es wird beobachtet, dass die Verspannungen relativ früh während des Wachstums abgebaut werden, was auf die Ausbildung von Versetzungen hindeutet. Weiterhin zeigen die Filmkraft-Kurven eine Anisotropie im Vergleich zu denen aufgenommen unter As-reichen Bedingungen. Eine erste vorläufige Analyse dieser Filmkraft-Kurven wird beschrieben.

Schlagwörter:
InAs Quantenpunkte, Molekularstrahlepitaxie, Verspannung, Anlassen

Abstract

The influence of stress on the growth of InAs on GaAs(001) by molecular beam epitaxy (MBE) is investigated in this thesis. An *in-situ* cantilever beam measurement (CBM) setup was used to measure the evolution of the film force during deposition and subsequent annealing at the growth temperature. The slope in a plot of film force versus film thickness is equal to the stress that builds up during heteroepitaxial growth. Film force curves were measured for InAs deposition under As-rich as well as In-rich growth conditions. The growth under As-rich conditions proceeds in the Stranski-Krastanov growth mode, meaning that quantum dots are formed after the initial growth of a wetting layer. During subsequent growth interruptions or intentional annealing at the growth temperature, the quantum dots undergo ripening. This growth mode of InAs films and the subsequent annealing behavior were studied in detail in this thesis. To understand the influence of strain on the growth mechanisms, the film force curves were analyzed and correlated to the morphological evolution of the InAs films during deposition and especially during annealing. This was achieved by developing new models for the evolution of the film force during annealing.

During the growth of InAs on GaAs(001) under As-rich conditions, the film force shows a linear slope up to a value of 2.3 N/m. This linear increase in film force corresponds to the deposition of the wetting layer. Beyond the critical thickness of 1.5-1.6 monolayers, the film force proceeds with a decreasing slope, indicating a strain release by the formation of quantum dots. When the samples are subsequently annealed, the film force decreases again due to the ripening of the quantum dots and the desorption of InAs. Models were developed to fit and explain the relaxation of the film force measured during the annealing of InAs quantum dots.

At temperatures lower than 470 °C, quantum dots undergo standard Ostwald ripening. Different mechanisms, such as kinetic and diffusion limited, determine the ripening process. Fits of models based on these mechanisms to the film force relaxation curves, show, that although the relaxation curve for annealing at 440 °C can be fitted reasonably well with all the models, the model describing ripening limited by the diffusion along dot boundaries yields a slightly better fit. The relaxation curves obtained at 455 °C and 470 °C can be fitted very well only with the model in which the ripening is controlled by the attachment/detachment of atoms on the dot surface.

Annealing of quantum dots at temperatures higher than 500 °C shows a very different behavior. The film force accumulated during the quantum dot formation relaxes below the value which was built-up by the wetting layer growth. Atomic force microscopy images reveal that the quantum dots ripen first and then dissolve after 450 s - 600 s annealing. These observations are explained by a combination of In desorption and interdiffusion between Ga and In. The photoluminescence spectra of quantum dots at different annealing stages corroborate our explanation.

In contrast to the growth under As-rich conditions, the growth under In-rich conditions does not lead to the formation of quantum dots but proceeds rather in a layer-by-layer growth mode. The film force curves were also measured during this deposition mode. As expected, the curves are quite different from those obtained during Stranski-Krastanov growth. It is observed that the stress is relieved early on during the deposition. Further, the film force curves are anisotropic as compared to the growth under As-rich conditions. A preliminary analysis of the film force curves is presented.

Keywords:
InAs quantum dots, molecular beam epitaxy, stress, annealing

Parts of this work has been published or submitted for publication:

D. M. Schaadt, D. Z. Hu, and K. H. Ploog, *Stress evolution during ripening of self-assembled InAs/GaAs quantum dots*, J. Vac. Sci. Technol. B 24(4), 2069 (2006).

D. Z. Hu, D. M. Schaadt, and K. H. Ploog, *Stress development during annealing of self-assembled InAs/GaAs quantum dots measured in-situ with a cantilever beam setup*, J. Crystal Growth 293, 546 (2006).

D. M. Schaadt, D. Z. Hu, and K. H. Ploog, *Stress evolution during ripening of self-assembled InAs/GaAs quantum dots*, Virt. J. Nano. Sci. Technol. August 7th (2006).

D. Z. Hu, D. M. Schaadt, A. Trampert, and K. H. Ploog, *Stress relaxation during annealing of InAs/GaAs quantum dots: influence of interdiffusion and In desorption*, Appl. Phys. A, submitted.

D. Z. Hu, D. M. Schaadt, and K. H. Ploog, "InGaAs quantum dots on GaAs(001) prepared by annealing during growth interruption," submitted.

D. Z. Hu, D. M. Schaadt, A. Trampert, and K. H. Ploog, "Stress evolution during layer-by-layer growth of InAs on GaAs(001)," submitted.

Conference contributions:

D. M. Schaadt, D. Z. Hu, and K. H. Ploog, *Stress Evolution During Ripening of Self-assembled InAs/GaAs Quantum Dots*, 33st Conference on the Physics and Chemistry of Semiconductor Interfaces, Cocoa Beach, FL, USA, Jan 15-19 (2006).

Abbreviations

AFM	Atomic Force Microscopy
CBM	Cantilever Beam Measurement
CVD	Chemical Vapor Deposition
DOS	Density of States
FF	Film Force
FM	Frank-van der Merwe
HRTEM	High Resolution Transmission Electron Microscopy
LSW	Lifshitz, Slyozov and Wagner
MBE	Molecular Beam Epitaxy
ML	Monolayer
MOVPE	Metal Organic Vapour Phase Epitaxy
PL	Photoluminescence
PVD	Physical Vapor Deposition
QD(s)	Quantum Dot(s)
QW(s)	Quantum Well(s)
RHEED	Reflection High Energy Electron Diffraction
SK	Stranski-Krastanov
SPA-LEED	Spot Profile Analysis Low Energy Electron Diffraction
STM	Scanning Tunneling Microscopy
TEM	Transmission Electron Microscopy
UHV	Ultra High Vacuum
VCSEL	Vertical Cavity Surface Emitting Laser
VW	Volmer-Weber
XRD	X-ray Diffraction
μ PL	Micro-photoluminescence
2D	Two Dimensional
3D	Three Dimensional

Contents

List of Figures

Chapter 1

Introduction

Semiconductor optoelectronic devices form the heart of today´s communication industry [1]. Their fabrication methods and the control of the optoelectronic properties have to be constantly adjusted to the needs of the industry. One example of an optoelectronic device is the quantum well (QW) laser diodes. The emergence of these semiconductor devices marks a new stage at energy band engineering and has reflected the new optical properties pertinent to a two dimensional (2D) system which has a step-like density of states (DOS). Following the successful application of QW devices, it is natural to desire electronic and optoelectronic devices with even more reduced DOS structures. In quantum dots, the strong confinement imposed in all three spatial dimensions results in a delta function-like DOS and is similar to atoms. Therefore they are frequently referred to artificial atoms. These quantum dots have found applications in a variety of optoelectronic devices such as lasers and photodetectors. In some cases, these quantum dot devices show superior performances in comparison to their QW counterparts [2, 3, 4, 5, 6].

Complete quantization of the electrons in a quasi-zero-dimensional quantum dot was first achieved by Reed et al. [7] who reported the creation of a square quantum dot with a side length of 250 nm, etched by means of lithography. However, optical lithography or etching used so far cannot provide the needed confinement of the charge carriers at room temperature. A simple approach to form QD is to use self-assembled crystal growth which occurs during heteroepitaxy of lattice mismatched systems in processes such as molecular beam epitaxy (MBE), chemical vapour deposition (CVD) and metal-organic vapour phase epitaxy (MOVPE). Quantum dots formed by self-assemble were observed in different epitaxial systems such as III-V InAs/GaAs, InAs/InP, GaSb/GaAs, InP/GaP; IV-IV Ge/Si; II-VI

CdSe/ZnSe, and CdTe/ZnTe [6, 8].

One of the most widely studied and most interesting system is In(Ga)As quantum dots grown on either GaAs or InP-related substrates. These quantum dots structures are promising for optical devices due to their possibly wide range of emission wavelengths [9, 10]. Especially important for the telecommunication industry are here the wavelengths of zero dispersion and lowest absorption in quartz optical fibres 1.3 and 1.55 μm, respectively. So far, lasers operating at these two wavelengths are based on InP substrates. The low conduction band discontinuity of InGaAsP leads to a relative poor thermal stability of laser operation, caused by electron escape. This phenomenon is especially strong in lasers operating at 1.3 μm, since the confinement is smaller. In contrast, lasers based on GaAs substrates provide a larger temperature stability due to the larger conduction band discontinuity. Moreover, GaAs substrates provide a possibility to realize monolithic vertical cavity surface emitting lasers (VCSEL) using highly effective AlO_x/GaAs Bragg reflectors. In(Ga)As quantum dots on GaAs substrate also open up a possibility to obtain an emission wavelength over a very wide range from 0.95 μm up to 1.55 μm. Such long wavelengths cannot be achieved using InGaAs QWs due to the formation of misfit dislocations caused by the misfit strain. The longest lasing wavelength in the conventional laser structures is about 1.2 μm [11]. The lasing wavelength up to 1233 nm was achieved by using a strain compensation [12]. By now the operation of lasers based on InGaAs/GaAs quantum dots with wavelength up to 1.35 μm is demonstrated, and up to 1.55 μm using an InGaAs metamorphic buffer on GaAs substrate. On the other hand, lasers based on quantum dots were claimed to have a very long operation lifetime.

In order to control the emission wavelength, the dot size, the dot distribution and the dot composition have to be controlled with great care. In lattice-mismatched systems such as InAs on GaAs or InP, the dot formation occurs in the Stranski-Krastanov growth mode. Further morphological changes occur during a subsequent growth interruption or an overgrowth. For instance, during a growth interruption at the deposition temperature, InAs quantum dots typically undergo Ostwald-ripening, but can also dissolve at higher temperatures. Both processes will change the dot size distribution and the dot composition drastically and will therefore heavily influence the emission wavelength. Although growth interruptions appear to be avoidable by switching the material supply quickly, still the quantum dots are not covered immediately and therefore are not frozen in their initial state. Without a detailed understanding of the involved mechanisms in the dot formation, dot ripening and dot dissolution, a careful control of the emission wavelength of devices based on quantum dots cannot be achieved. Due to the strong lattice mismatch between InAs and the typically used substrates, stress plays a major role during the formation, the annealing and the overgrowth of the dots. It is therefore necessary to first study the stress evolution on a simple model system, namely InAs on GaAs(001). By comparing different growth regimes such as As-rich, where Stranski-Krastanov takes place, and In-rich, where no quantum dots are formed due to a layer-by-layer growth mode, additional insight can be obtained.

This thesis focuses on the study of the stress evolution of InAs films on GaAs(001). Both As-rich and In-rich growth conditions are investigated and a major part of the study focuses on the investigation of the annealing behavior of InAs quantum dots. It will be shown that an intentional annealing can have even benefits in trying to control the dot size and therefore the emission wavelengths. To investigate the stress evolution, InAs quantum dots were fabricated in a MBE chamber equipped with an *in-situ* cantilever beam measurement setup. This setup was used to measure a film force during experiments. In a plot of the film force versus nominal deposited film thickness, the slope is equal to the stress built-up in the films. In combination with other *ex-situ* characterization techniques, such as atomic force microscopy (AFM) and transmission electron microscopy (TEM), the controlling mechanism for the annealing behavior of the dots at various temperatures can be determined.

The thesis starts with general background (chapter 2) on thin film growth and stress accommodation during heteroepitaxy. For InAs growth on GaAs(001), the formation of InAs quantum dots and their annealing behavior are described in detail. Next (chapter 3), the growth procedure and experimental methods are introduced with special focus on the *in-situ* cantilever beam measurement setup and the measurement of film force curves.

The first three results chapters (chapters 4 to 6) focus on the growth and annealing of InAs thin films under As-rich conditions, while the last result chapter (chapter 7) discusses some investigations performed under In-rich growth conditions. The film force evolution during InAs quantum dot growth is presented in Chapter 4. A comparison of film force for wetting layer and quantum dot samples annealed at various temperatures is presented and discussed. In chapter 5, the annealing of InAs quantum dots at low temperatures under standard Ostwald ripening conditions is investigated. A new approach to determine the ripening process is presented. Instead of fitting only the average dot radius obtained by atomic force microscopy (AFM) or x-ray measurements, fitting the complete time evolution of the dot radius distribution-function to the experimental data is performed. In combination with AFM images taken at various times during annealing, it is possible to determine the involved ripening mechanism.

Chapter 6 will present the effect of annealing at high temperature on InAs quantum dots, at which InAs quantum dots first ripen but then dissolve. Quite interestingly, over a certain range of annealing time, the dot size remains constant and relatively narrow, while just the dot density decreases with annealing time. This provides a new approach to a better control of the dot size distribution. Further, the fabrication of dots under such conditions allows the control of the dot density to very low values as a function of annealing time while other factors such as dot size do not change strongly. This is beneficial for some studies such as micro-photoluminescence, where the investigation of an individual dot is only possible by lithographically defining windows with a small enough number of dots. To understand the observed annealing behavior, the film force curve measurements were analyzed together with AFM images and high resolution transmission electron microscope (HRTEM) images. It was found that, although In desorption influences the behavior of quantum dots seriously, the dissolution of quantum dots is a result of the combined In desorption and interdiffusion between Ga and In. Therefore, for explaining the dissolution of quantum dots, the classical ripening theory must be extended by incorporating these effects.

In the last result chapter (chapter 7), the focus is shifted away from the quantum dot growth under As-rich conditions to the layer-by-layer growth under In-rich conditions. The film force curves reveal, that the stress is relieved early on along the [110] direction during deposition. Further, the film force measurements performed with the substrate aligned in the [110] and [$1\bar{1}0$] directions show an asymmetry. These preliminary results will be discussed.

Finally, all results are summarized with regard to the importance of the control of the annealing of quantum dots and an outlook is given on possible further studies.

Chapter 2

Background

This thesis deals with molecular beam epitaxial growth of InAs on GaAs(001) substrates and presents a study on the subsequent annealing behavior of InAs quantum dots. To understand and to discuss the involved processes, it is helpful to review epitaxial growth of thin films in general and to highlight some associated processes. Therefore, this chapter will introduce the basics of thin film growth processes, misfit stress and the mechanisms for strain relaxation during heteroepitaxy, especially during an important phenomenon, Ostwald-ripening, which 3D dots generally experience during post-growth annealing.

2.1 Thin film growth processes

All of the commonly used thin film growth techniques supply the atoms or molecules to the substrates from the vapor phase. The major differences among the techniques are the methods used to produce the vapor and the pressure in the chamber in which the growth takes place. Vaporization of species can be realized by the physical or chemical means. Physical vapor deposition (PVD) processes involve the evaporation by heating or sputtering by impact of high energy particles. The PVD processes generally produce the vapors of atomic or small molecular species. The chemical vapor deposition (CVD) methods use the materials that are intrinsically gases under certain conditions in the reactor and are often supplied through pipes and valves from storage containers. The events necessary for film nucleation and growth from the vapor phase are shown schematically in Fig. 2.1.

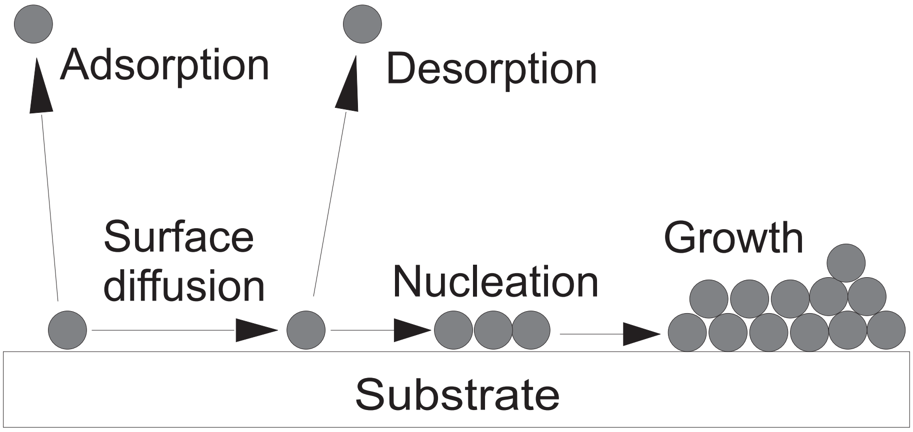

Figure 2.1: Events in a typical vapor phase thin film growth process.

For III-V compound thin film growth by solid source molecular beam epitaxy (MBE), commonly effusion cells are used for evaporation of the source materials that are pure elemental materials. A gallium or an indium atomic beam and an arsenic cluster beam composed of As_4 or As_2 molecules are irradiated onto a GaAs surface which is kept at an elevated temperature in a vacuum chamber. The gallium (or indium) and arsenic atomic layers grow alternatively. In the following subsection the growth procedure by heating-based vaporization (evaporation) during the growth of GaAs and InAs will be introduced.

Once the atoms or molecules have been produced, the following steps needed to grow the film are adsorption of atoms or molecules on the growing surface, migration of adatoms and molecules, reaction to form the film, coalescence of the reacted material into the islands and desorption (re-evaporation) of any product or unused adatoms or molecules from the surface. Since the desorption plays a major role in the following study of the stress evolution during annealing at high temperature, all of the kinetic perspectives for film growth will be reviewed in detail in the following sections to help understand the experimental results.

2.1.1 Adsorption and incorporation

The first event in the film growth, as shown in Fig. 2.1, is the adsorption. The essential step in adsorption is to reduce the energy of the adsorbing species on the surface below the energy in its vapor phase to prevent its escape. Typically, this happens in a series of stages. The atoms in the gas phase have a kinetic energy of approximately k_BT where the temperature is same to that of vapor source. If an attractive interaction, such as bonding, exists between the adatoms and the surface, the adatoms accelerate under the attractive force and gain kinetic energy. This kinetic energy is usually much greater than the gas phase kinetic energy. The arriving adatoms will leave the surface if there are no other atoms available or there is no efficient process available to transfer the excess energy of the adatoms. This also is the reason that the reactions normally do not occur between pairs of atoms in the gas phase. Adsorption on a surface is much simpler as the surface itself is a reservoir of energy (in the form of heat) and momentum with which the arriving adatoms can exchange these conserved quantities. This is the case in MBE growth of InAs and GaAs.

For a growth process with a given flux of atoms F arriving at the surface, the flux of gas ζ actually adsorbed is:

$$\zeta = F\alpha, \tag{2.1}$$

where α is the probability for remaining on the surface after adsorption and is dependent upon the local chemistry and structure of the surface. It is relatively constant for a given gas and a given surface. However, as adsorption continues the surface becomes covered with the adsorbate and the adsorption probability may change dramatically.

In the case of growth of GaAs and InAs compounds, arsenic is volatile and usually is supplied excessively. The controlling step for film growth is the incorporation of Ga or In. However, the adsorption of As_4 or As_2 and their reactions play an important role during growth. Kinetic studies of III-V compounds have been done by Arthur [13] and Foxon et al. [14, 15] using reaction rate theory. They showed that the adsorption of the As_4 and As_2 clusters is different and is temperature dependent. In the case of As_4, at temperatures of 300-450 K, As_4 is physically adsorbed with an adsorption energy of 0.38 ± 0.03 eV (8.8 kcal/mol) [13, 16]. At an active Ga site, the molecularly adsorbed species is dissociated and a new As layer grows on the surface. At temperatures above 600 K, the probability of As_4 molecules for remaining on the surface after adsorption increases, due to additional Ga on the surface which is formed by increased desorption of As from the GaAs in the form of As_2. When two As_4 clusters migrating on the surface collide with each other, they may form a state of coadsorption. The coadsorption state is decomposed into four dissociatively adsorbed As atoms and an As_4 cluster which is relieved into vacuum. Thus, the As layer grows with making an As island region on a Ga surface.

As_2 molecules also adsorb physically on the GaAs(001) surface. This rather weakly bound state of As_2 is not sufficiently long-lived at standard growth temperatures to give rise to incorporation of molecules, but lead to temporary trapping of molecules close to the surface. However, with Ga adatoms present on the surface, stronger binding sites for the As_2 molecules arise that are accessible from the gas phase without a barrier [17].

For the adsorption of Ga, according to the calculation results obtained by Kley et al. [18], it was found that Ga has its strongest adsorption site inside As surface dimers, thereby breaking the dimer bond. The picture evolving from these computational results suggests that a possible role of the Ga atoms in growth could be the breaking up of existing As surface dimers, and the formation of locally Ga-rich environments that act as selective sites for adsorption of As_2 molecules from the gas phase. The adsorption probability of Ga atoms is unity with an arsenic molecule influx [19]. This has been substantiated by Kratzer and Morgan et al. [17, 20]. Ga adatoms were found to bind strongly (between 1.5 and 2.1 eV at various surface sites) [21].

The homoepitaxial growth of InAs(001) behaves analogously to homoepitaxial growth of GaAs(001). The differences, which are nearly quantitatively accounted for, are simple bond energy arguments. The activation energies of In and Ga incorporating into InAs and GaAs are 4.0 eV and 4.8 eV, respectively. Considering the growth of InAs and GaAs is that one layer In or Ga and one layer As grow alternatively, incorporation of In and Ga is time dependent for submonolayer surface coverage. The probability of incorporation of In or Ga decreases with submonolayer In or Ga growth. The same situation occurs in the growth of InAs on GaAs. Additionally, the adsorption of In on GaAs(001) is temperature dependent. The activation energy is 2.6 eV for our work temperature region (above 600 K) [22]. This energy is lower than the energy for homoepitaxial growth. The decrease of the activation energy is a result of misfit strain accommodated during epitaxial growth.

2.1.2 Desorption

Desorption is the reverse process of adsorption. The desorption of adatoms requires the surface heat and momentum reservoir to supply enough kinetic energy. In general the rate per unit area of desorption will depend upon the areal concentration of adatoms on the surface:

$$r_d = A^n \omega e^{-\frac{H}{k_B T}}, \tag{2.2}$$

where r_d is the desorption rate, A is the concentration of desorbing species on a surface, n is the order of the desorption process, ω is the attempt frequency, k is Boltzmann's constant, t is the temperature, and H is the desorption energy. Atoms may leave a surface alone or in groups. Simple desorption of an adatom is thermally activated and concentration independent. Associative desorption involves multiple atoms and is concentration dependent. Additionally, desorption from chemically different areas proceeds with different rates.

The desorption of arsenic from GaAs(001) surface without Ga beam is investigated by Foxon and Joyce with As_2 [23] and As_4 [15] incident flux. The desorption rate of As_2 decreases with the temperatures below 600 K while it remains constant at higher temperatures. At temperatures below 600 K, an association reaction occurs with the formation of As_4. The desorption rate of As_4 reaches the maximum at about 450 K. As does not desorb in the form of As_4 at temperatures higher than 600 K and the total As_2 flux from the surface is independent of the temperature in the range 600-900 K with an incident As_2 beam. Considering the backbonding energy of As, the activation energy for As_2 desorption is about 1.9 eV [24].

The desorption of Ga and In from GaAs and InAs was investigated by Zhang et al. [25]. With the constant incident As_2 flux, the activation energy for Ga desorption from GaAs surface is approximately 4.0 eV. While with As_4 incident flux, the activation energy for Ga desorption from GaAs surfaces is about 3.6 eV. The activation energy for In desorption from InAs surface is temperature dependent according to Zhang et al. With the As_2 incident flux, it is 4.0 eV for the temperatures above 460 °C while it is 0.8 eV for temperatures below 460 °C. The difference of activation energy for In desorption is attributed to different process. At high temperature, the desorption of In involves the dissociation of InAs while the desorption of In at low temperature is dependent on the surface In adatom population and likely the source for In desorption is small In clusters. The activation energy for In desorption from GaAs(001) is about 1.5 eV and it significantly lower than that of InAs and GaAs homoepitaxial system above 460 °C due to the high degree misfit strain. This misfit strain reduces the cation-surface bond strength. In desorbs from the In-rich part of InAs quantum dots at certain high annealing temperature, namely 500 °C, will be shown at chapter 6.

2.1.3 Sticking coefficient and surface coverage

The sticking coefficient is the ratio of the rate of adsorption to the rate at which the adsorptive strikes the total surface, i.e. covered and uncovered. It is usually a function of surface coverage, a function of temperature and a function of the details of the surface structure of the adsorbent. The surface coverage at steady state can be determined by the balance of the adsorption rate and the desorption rate:

$$R\alpha = \xi^n \omega e^{-\frac{H}{k_B T}}, \tag{2.3}$$

where the unitless fractional surface coverage $\xi = A/N_s$ replaces the concentration of adsorbate A, N_s is the number of surface sites per unit area, the flux F was replaced with the average arrival rate (in units of inverse seconds) per site, $R = F/N_s$. The equation is in area-independent units. This equation may be solved for ξ^n to get the steady-state surface coverage:

$$\xi^n = R\phi\tau \tag{2.4}$$

with

$$\frac{1}{\tau} = \omega e^{-\frac{H}{k_B T}}, \tag{2.5}$$

in which τ is the average residence time of an adatom on the surface. In the case of growth, a steady-state adsorption rate that exceeds the desorption rate leads to a net deposition.

In the absence of a Ga beam, the sticking coefficient of As_2 and As_4 on GaAs(001) surfaces with constant incident As_2 flux (1×10^{13} $molecules\ cm^{-2}\ s^{-1}$) and As_4 flux (3×10^{11} $molecules\ cm^{-2}\ s^{-1}$ and 2×10^{12} $molecules\ cm^{-2}\ s^{-1}$) is temperature dependent as shown by Foxon et al. [15, 23]. In their work, the sticking coefficient of As_2 increases linearly from 0 to 0.84 with the temperature increasing from 600 K to 900 K. While the increase of the sticking coefficient of As_4 is not linear with the increase of temperature. Considering the incorporation mechanism of As_4 into the growing film, two As_4 clusters are involved and only one survives in the reaction, the sticking coefficient is always less than 0.5. With supplication of Ga, the sticking coefficient of

As_2 and As_4 will be enhanced and can reach unity for As_2 and 0.5 for As_4. The sticking coefficient of Ga and In on GaAs in normal MBE operating conditions is approximately unity in the case of excess As is supplied.

2.1.4 Surface diffusion

An adatom absorbed by low binding energy has a high probability of desorption. However, if it can migrate to a step or a kink site it will be bound more strongly. The diffusion distance before desorption is:

$$x_d = (D\tau)^{1/2}, \tag{2.6}$$

where $D = \nu_d exp(-e_d/kT)$ is the diffusion coefficient, ν_d is a hop in a particular direction, and e_d is the surface diffusion energy. The adatoms on surfaces have preferred locations relative to the underlying atoms. The preferred location is determined by the electronic structure of the surface and the possible bonding configurations. In reality, surface usually consists of relatively smooth terraces, various smaller structures including free adatoms and surface steps. All these features are the preferred or repulsive locations for adatoms. The consequence of these predictions is that adatoms will tend to attach to these features or will stay away from them and enhance nucleation of new adatom islands in the surrounding region.

The surface migration energy barrier of As_4 on GaAs(001) is about 0.24 eV (5.5 kcal/mol) [13, 16]. For GaAs(001) surface, the most technologically important and most studied surface is the (2×4) reconstructed surface. The diffusion of Ga atoms on a GaAs(001)-(2×4) reconstructed surface at various substrate temperatures under a constant As_4 beam equivalent pressure of 10^6 Torr was investigated by using a combination of MBE and scanning tunneling microscopy (STM) [26]. The activation energy is about 1.7 eV. According to the first-principals total-energy calculations of Kley et al. [18], the Ga diffusion on an arsenic-free environment is anisotropic. The activation energy is 1.5 eV along the [110] direction and it is 1.2 eV along the $[1\bar{1}0]$ direction.

An anisotropic diffusion is expected for In and might lead to an anisotropic stress relief as measured in film force curves along different substrate direction during growth of InAs on GaAs(001) under In-rich conditions, as will be described in chapter 7.

2.1.5 Nucleation and growth of GaAs on GaAs(001)

Nucleation is a process of adding atoms to a small cluster until the cluster becomes stable. When the cluster is large enough, it is unlikely to disappear. The nucleation rate R, is the number of nucleation events per second which occur in a given population:

$$R = \nu N^n e^{-E/kT}, \tag{2.7}$$

with ν is an attempt frequency (constant), N is the number of atoms per unit area, E is the nucleation barrier and n is the effective reaction order. Thus, higher energy barriers and lower temperatures delay nucleation. Higher concentration of adatoms increases nucleation rate.

The quantitative nucleation kinetic studies of GaAs on GaAs surfaces have been investigated by Joyce et al. [27] with *in-situ* STM. The start GaAs(001) surface is under 2 × 4 reconstruction with two As dimers and two missing dimers in the topmost layer and with the exposed As atoms in the third layer at the bottom of the dimer trenches which are dimerised too [28, 29]. The missing dimer rows provide the favored sites for the initial Ga nucleation. Such a process likely produces anisotropic string along missing dimer rows. However, according to the investigation for GaAs growth from As_4 and Ga by Foxon and Joyce [15], the growth of GaAs requires pair of adjacent Ga adatoms to be available to react with two As_2 produced by pairwise dissociation of As_4 molecules. The possibility of pair of Ga atoms forming or adding to an existing chain and remaining undissociated long enough to interact with As_4 would be comparatively small. Therefore, the long chain would not be likely formed. On the other hand, the growth of GaAs perpendicular to the missing dimer rows proceeds with same process. The pair attachment of Ga adatoms is required. The pair attachment of Ga occurs only when the site in adjacent dimer trenches are filled, which will be an rare event. Consequently an enhancement of GaAs growth along dimer rows more likely occurs. However, the pairing between adjacent dimer rows switches in alternate layers so that an atom pair in the topmost layer straddles two pairs in the penultimate layer. This makes nucleation in the topmost layer only in regions where a filled trench is located. Homoepitaxial growth of GaAs on GaAs(001), once 2D nuclei have been formed, they grow by collection of atoms or molecules and transfer of atoms between the nuclei, or coalesce by moving as a unit until two nuclei meet till cover the whole surface and while new 2D nuclei forms on the new surface.

2.1.6 Nucleation and growth of InAs on GaAs(001)

The lattice mismatch of about 7% between InAs and GaAs has important consequences for the growth of InAs on GaAs substrate. Classically, the classification of heteroepitaxial growth modes is based on thermodynamic considerations. Under thermodynamic considerations, three growth modes are distinguished (Fig. 2.2): the Frank-van der Merwe (FM) growth mode (Fig. 2.2b), in which the epi-layer grows in a 2D layer-by-layer way, the Volmer-Weber (VW) growth mode, in which the three-dimensional (3D) islands are developed (Fig. 2.2a), and the Stranski-Krastanov (SK) growth mode (Fig. 2.2c), in which the initial epilayer(s) grows in the 2D layer-by-layer mode forming the so-called wetting layer before the formation of 3D islands (crystallites) starts.

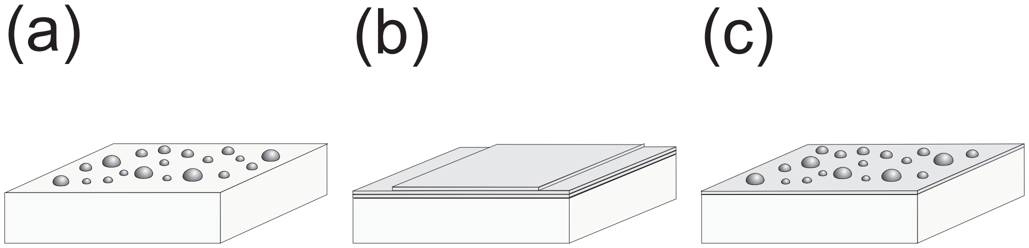

Figure 2.2: Crystal growth modes according to the classical classification. (a) Volmer-Weber (VW) growth mode, (b) Frank-van der Merwe (FM) growth mode, and (c) Stranski-Krastanov (SK) growth mode.

These three growth modes can be predicted in the terms of an interplay between surface and interface energetics. For a given system including substrate A and epi-growth material B, suppose γ_A, γ_B and $\gamma_{(AB)}$ are the surface free energy of substrate A, epi-layer B and interface between A and B, respectively. If the inequality

$$\gamma_A + \gamma_{(AB)} > \gamma_B \tag{2.8}$$

is fulfilled, B grows on A in the FM mode. In the opposite case, B grows on A in the VW mode. The SK growth mode, however, is generally accepted to be strain related, because the accommodation of misfit strain between epilayer and substrate requires the strain energy increases with film thickness. This means that, while the balance is initially in favor of two-dimensional growth, it subsequently becomes unstable and 3D islands are formed. The transition thickness, also called critical thickness, depends on the lattice mismatch between two materials and the surface properties of the epitaxy. More details about the critical thickness will be introduced in the following section. In the case of InAs on GaAs(001), in terms of the observed surface morphology, initially a 2D wetting layer, which is characterized by the formation of a pseudomorphic InAs film, grows on GaAs(001) with stress accumulated with thickness. After about 1.5-1.8 ML InAs growth, accumulated stress in the wetting layer is relieved by forming the coherent 3D islands, i.e. dislocation free and strained, as observed by TEM examination, both plan-view and cross-section view [30, 31]. The 2D to 3D transition is very rapid, occurring over < 0.1 ML of incremental deposition, with some evidence for the existence of a precursor state. Moreover, according to the results obtain by Joyce et al. [32, 33, 34, 35, 36, 37, 38], the wetting layer does not consist of pure InAs but is rather of $\mathrm{In}_x\mathrm{Ga}_{1-x}\mathrm{As}$ alloy with $x = 0.2 - 0.6$. Also it was found that the integrated volume of 3D dots exceeds the amount of InAs deposited after the transition from wetting layer to dots at all substrate temperatures ≥ 400 °C [35, 36, 38, 39]. This indicates that the QDs are not composed by pure InAs, even though no other material is being deposited, but are an (In, Ga)As alloy, whose In concentration increases with decreasing In flux. It is clear that Ga is being incorporated from wetting layer and/or the substrate.

2.2 Strain accommodation

The epilayer growth of a semiconductor with a lattice constant a_{epi} on a thick substrate with a lattice constant a_{sub} which is different from a_{epi} is illustrated in Fig. 2.3. The lattice mismatch is measured by the misfit parameter f_m, where

$$f_m = \frac{a_{epi} - a_{sub}}{a_{sub}}. \tag{2.9}$$

If both the misfit parameter f_m and the thickness h of the epilayer are small, the misfit between the two semiconductors is accommodated by a tetragonal strain of the epilayer as shown in Fig 2.3. For $a_{epi} > a_{sub}$, a compressive strain is stored and for $a_{epi} < a_{sub}$, a tensile strain is stored in the epilayer. The strain is homogeneous and is known as the 'misfit strain'.

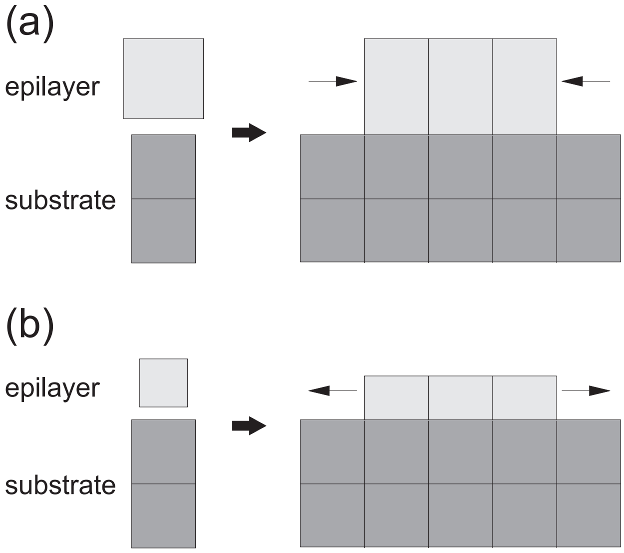

Figure 2.3: Biaxial stress of a crystal that is epitaxially deposited on a substrate with different lattice constant. (a) Compressive: the lattice constant of the epi-material is larger than the lattice constant of the substrate, (b) Tensile: the lattice constant of the epi-material is smaller than the lattice constant of the substrate. Here the lattice mismatch is small enough so that elastic compression or tension is possible and the epitaxy is pseudomorphic.

For cubic structure, a strain tensor is used to describe the distortion of the unit cell with respect to the equilibrium structure. The primitive translational vectors can be expressed in terms of the unstrained lattice constants a by

$$\begin{aligned} a_1 &= a\mathbf{e}_x, \\ a_2 &= a\mathbf{e}_y, \\ a_3 &= a\mathbf{e}_z, \end{aligned}$$

with a set of orthonormal basis vectors $(\mathbf{e}_x, \mathbf{e}_y, \mathbf{e}_z)$ in a Cartesian coordinate space (Fig. 2.4).

Under strain, the lengths and/or the directions of the primitive translational vectors are modified. The modified basis vectors ($\mathbf{e}'_x, \mathbf{e}'_y$, and $\mathbf{e}'_z$) are related to the original set of vectors according to

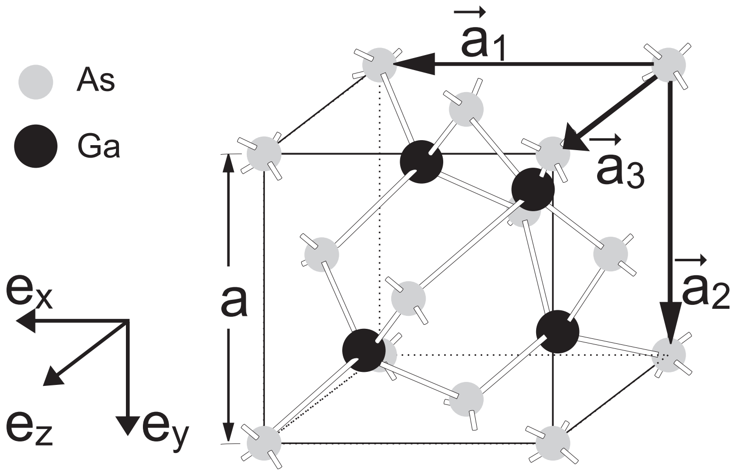

Figure 2.4: Scheme of the unstrained unit cell of GaAs with the primitive translation vectors a_i and the set of Cartesian unit vectors $(\mathbf{e}_x, \mathbf{e}_y, \mathbf{e}_z)$. a is the unstrained lattice constant.

$$\begin{aligned}
\mathbf{e}'_x &= (1+\epsilon_{xx})\mathbf{e}_x + \epsilon_{xy}\mathbf{e}_y + \epsilon_{xz}\mathbf{e}_z,\\
\mathbf{e}'_y &= \epsilon_{yx}\mathbf{e}_x + (1+\epsilon_{yy})\mathbf{e}_y + \epsilon_{yz}\mathbf{e}_z,\\
\mathbf{e}'_z &= \epsilon_{zx}\mathbf{e}_x + \epsilon_{zy}\mathbf{e}_y + (1+\epsilon_{zz})\mathbf{e}_z,
\end{aligned}$$

with the strain tensor elements ϵ_{ij}. The tensors consist of normal strain components ϵ_{xx}, ϵ_{yy} and ϵ_{zz} as well as shear strain components ϵ_{xy}, ϵ_{xz} and ϵ_{yz}. The stress tensor is related to the strain tensor via the elastic constants according to Hooke's law:

$$\sigma_{ij} = \sum_{kl} c_{ijkl} \cdot \epsilon_{kl}, \tag{2.10}$$

$$\epsilon_{ij} = \sum_{kl} s_{ijkl} \cdot \sigma_{kl}, \tag{2.11}$$

where c_{ijkl} is elastic stiffness and s_{ijkl} is elastic compliance. The subscripts i, j, k, l run from 1 to 3. Therefore, c_{ijkl} and s_{ijkl} have 3^4 components. Fortunately, the symmetry of the elasticity $c(s)_{ij} = c(s)_{ji}$ and the strain tensor

$\epsilon_{ij} = \epsilon_{ji}$ reduces the components to 36. Further, considering the elastic energy density E_{EL} as a function of the elements of the elastic stiffness and strain tensors:

$$E_{EL} = \frac{1}{2} c_{ijkl} \epsilon_{ij} \epsilon_{kl}. \tag{2.12}$$

The elastic stiffness tensors must satisfy:

$$c_{ijkl} = c_{klij}. \tag{2.13}$$

This symmetry continues to reduce the number of its independent components to 21. Further, the number of independent components reduces to three for cubic classes due to the symmetry of cubic structure. They are c_{1111}, c_{1122} and c_{1212}. Then

$$\begin{pmatrix} \sigma_{11} \\ \sigma_{22} \\ \sigma_{33} \\ \sigma_{12} \\ \sigma_{23} \\ \sigma_{13} \end{pmatrix} = \begin{pmatrix} c_{1111} & c_{1122} & c_{1122} & 0 & 0 & 0 \\ c_{1122} & c_{1111} & c_{1122} & 0 & 0 & 0 \\ c_{1122} & c_{1122} & c_{1111} & 0 & 0 & 0 \\ 0 & 0 & 0 & c_{1212} & 0 & 0 \\ 0 & 0 & 0 & 0 & c_{1212} & 0 \\ 0 & 0 & 0 & 0 & 0 & c_{1212} \end{pmatrix} \begin{pmatrix} \epsilon_{11} \\ \epsilon_{22} \\ \epsilon_{33} \\ 2\epsilon_{12} \\ 2\epsilon_{23} \\ 2\epsilon_{13} \end{pmatrix}$$

and

$$\begin{pmatrix} \epsilon_{11} \\ \epsilon_{22} \\ \epsilon_{33} \\ 2\epsilon_{12} \\ 2\epsilon_{23} \\ 2\epsilon_{13} \end{pmatrix} = \begin{pmatrix} s_{1111} & s_{1122} & s_{1122} & 0 & 0 & 0 \\ s_{1122} & s_{1111} & s_{1122} & 0 & 0 & 0 \\ s_{1122} & s_{1122} & s_{1111} & 0 & 0 & 0 \\ 0 & 0 & 0 & s_{1212} & 0 & 0 \\ 0 & 0 & 0 & 0 & s_{1212} & 0 \\ 0 & 0 & 0 & 0 & 0 & s_{1212} \end{pmatrix} \begin{pmatrix} \sigma_{11} \\ \sigma_{22} \\ \sigma_{33} \\ \sigma_{12} \\ \sigma_{23} \\ \sigma_{13} \end{pmatrix}$$

For pseudomorphic epilayer growth on a substrate with square lattice which is studied in this work, no shear strains are found in the film, i.e. $\epsilon_{12} = \epsilon_{23} = \epsilon_{13} = 0$. The strain and stress in the film are: $\epsilon_{11} = \epsilon_{22} = f_m$ and $\sigma_{11} = \sigma_{22} = \sigma$. The stress along the direction perpendicular to the film is relieved: $\sigma_{33} = 0$. Then it follows:

$$\sigma = \frac{(c_{1111} - c_{1212})(c_{1111} + 2c_{1212})}{c_{1111}} f_m. \tag{2.14}$$

For the evaluation of the film tensions, Young´s modulus Y and Poisson´s ratio ν (direction-controlled) can also be used. For the cubic class,

$$\frac{1}{Y} = s_{11} - 2(s_{11} - s_{12} - \frac{1}{2}s_{44})(l_1^2 l_2^2 + l_2^2 l_3^2 + l_3^2 l_1^2) \tag{2.15}$$

$$\nu = -\frac{s_{12} + (s_{11} - s_{12} - \frac{1}{2}s_{44})(l_1^2 m_1^2 + l_2^2 m_2^2 + l_3^2 m_2^2)}{s_{11} - 2(s_{11} - s_{12} - \frac{1}{2}s_{44})(l_1^2 l_2^2 + l_2^2 l_3^2 + l_3^2 l_1^2)} \tag{2.16}$$

in which l_1, l_2, l_3 and m_1, m_2, m_3 are the direction cosines of vector $\vec{l}$ and $\vec{m}$. The vector $\vec{l}$ is parallel to the strain along e_x, whereas $\vec{m}$ is perpendicular to the strain along e_x and gives the direction of stress along e_y as the Poison-type contribution to the stress along e_x [40, 41, 42]. These are needed for calculation of the theoretical value of film force and stress for bulk structure for comparison to experimental results as will discuss in chapter 3 and 4.

2.3 Strain relief

Due to lattice mismatch between epilayer and substrate, the elastic energy E_{epi} per unit area stored in the epilayer for cubic class (001) surfaces is:

$$E_{epi} = E_{EL} \cdot h, \tag{2.17}$$

in which E_{EL} is the elastic energy density and h is the thickness of the grown film. Therefore, the elastic energy is proportional to the thickness of epilayer. As the thickness of epilayer increases and reaches to a certain critical value, strain starts to relieve. In the case of heteroepitaxial growth, two possibilities exist: either defects such as misfit dislocations are introduced to relieve the stress, or the surface of the film will buckle to relieve the stress (SK growth). In the first case, the film remains flat as in the case of InAs grown on GaAs(001) under In-rich conditions. In the second case, QDs form as in the case of InAs grown on GaAs(001) under As-rich conditions.

Two theories have been developed to calculate the equilibrium critical thickness h_c. The first theory originated in the work of Frank and Van der Merwe [43] and has been developed further by Van der Merwe and collaborators

[44]. It is based on the principle of energy minimization. The second is due to Matthews and Blakeslee [45, 46] and is known as the force balance theory. Initially these two theories gave different numerical values of the critical thickness for the same epilayer. However, if these two theories are formulated correctly, they are equivalent and always give identical numerical values of the critical thickness. In the force balance theory, Matthews and Blakeslee considered a substrate-epilayer structure in which threading dislocations crossing the interface are present and move to produce the misfit dislocations. The threading dislocation experiences two competing forces. When the threading dislocation propagates through the layer, a segment of misfit dislocation is created reducing the strain and the energy of the epilayer. This provides the driving force for the motion. The force is equal to Bhf_mb_1. The line tension E_D^{∞} (which is equal to the energy per unit length) of the misfit dislocation opposes the motion. The net force G acting on the threading dislocation is

$$G = Bh|f_mb_1| - E_D^{\infty}. \tag{2.18}$$

Below the critical thickness, G is negative and the layer remains pseudomorphic. As h increases, the driving force given by $Bh|f_mb_1|$ increases faster than the opposing force given by E_D^{∞}. Matthews and Blakeslee assumed that $G = 0$ at $h = h_c$. For $h > h_c$, G is positive and the threading dislocation moves, depositing the misfit dislocation. The critical thickness is obtained from $G = 0$ by the Matthews and Blakeslee equation,

$$h_c = \frac{1}{8\pi(1+\nu)b_1f_m}(a_0 + a_1 ln\frac{2\rho_c h_c}{q} - a_3), \tag{2.19}$$

which can be written using the form for the dislocation energy used by Ball and Van der Merwe [44] and Matthews [45, 46] as

$$h_c = \frac{b^2(1-\nu cos^2\beta)}{8\pi(1+\nu)b_1f_m} ln\frac{\rho_c h_c}{q}. \tag{2.20}$$

The principal of energy minimization states that below the critical thickness, the energy of the epilayer should increase by the introduction of misfit dislocation and beyond the critical thickness, the energy should decrease.

At the critical thickness, the total energy is a minimum and the change in energy on introducing a dislocation is zero. It can easily be seen that G also represents the change in energy of the epilayer that occurs by the introduction of unit length of the misfit dislocation and should be zero according to the principal of energy minimization.

The basic approach to the physics of SK growth is similar to that of the Matthews-Blakeslee model, except that one has to consider a perfectly strained coherent growth and energy reduction associated with the formation of a partially relaxed surface morphology. The nuance here is that the SK morphology is generally considered to be a kinetic growth instability. Once the critical thickness (different from that derived above) is attained, an array of islands with a particular periodicity is found to be maximally unstable. Thus, rather than individual dislocations getting inject, as above, the surface spontaneously starts to form an island array that grow in amplitude. Sometimes, even, the instability can undercut into the wetting layer.

After the formation of coherent dots and keeping the sample at an elevated temperature, coarsening or ripening of dots occurs. The coarsening of dots also relieves the stress which is still stored in the dots. However, the driving force for this stress relief is the decrease in total surface energy, different from the driving force for formation of dots, which is misfit stress. The next section will introduce this phenomenon in detail.

2.4 Ostwald ripening

Ostwald ripening describes a transformation process which has been observed in a large number of metallic and non-metallic systems where particles are dispersed in a matrix with various sizes. The driving force of this process is the decrease in total surface free energy. The process occurs in a such way that many small crystals form in a system initially but slowly disappear except for a few that grow larger on the expense of the small crystals. This process was first quantitatively described by Ostwald for small molecules [47] and was then named as Ostwald ripening.

During the ripening process, as the larger crystals grow, the area around them is depleted of smaller crystals. This is a spontaneous process that occurs because larger crystals are energetically more favored than smaller crystals. While the formation of many small crystals is kinetically favored (i.e. they nucleate more easily), large crystals are thermodynamically favored. Thus, from a stand point of kinetics, it is easier to nucleate many small crystals. However, due to Gibbs-Thompson effect, small crystals have a larger surface area to volume ratio than large crystals. Molecules on the surface are energetically less stable than the ones already well ordered and packed in the interior. Large crystals, with their greater volume to surface area ratio, represent a lower energy state. Thus, many small crystals will attain a lower energy state if transformed into large crystals and this is what one sees in Ostwald ripening.

After the qualitative description by Ostwald, Greenwood [48] derived a differential equation for the time dependence of particle radii. A detailed theory for particle ripening has been first developed simultaneously and independently by Lifshiz and Slyozov [49, 50] and Wagner [51]. Their theory, which is well accepted in the literature, is now often referred to as a classical LSW theory. According to the LSW theory, competitive growth takes place among precipitates when particles with various size are dispersed in a matrix. At any stage during ripening there is a so-called critical particle radius r_c being in equilibrium with the mean matrix composition. Particles with $r > r_c$ will grow and particles with $r < r_c$ will shrink. The growth originates from the concentration gradients around the particles caused by the thermodynamic demand, i.e. Gibbs-Thomson effect. The concentration at the surface of particles in equilibrium with larger particles is lower than that with smaller particles.

Any system of disperse particles statistically distributed in a medium and possessing certain solubility in it will be thermodynamically unstable due to a large interface area. Its decrease in approaching equilibrium is accompanied by particle ripening whose solubility depends on their radii and is described by the well known Gibbs-Thomson relation

$$C_r = C_e exp(\frac{2\gamma\Omega}{R_b T} \cdot \frac{1}{r}) \approx C_e(1 + \frac{2\gamma\Omega}{R_b T} \cdot \frac{1}{r}), \tag{2.21}$$

where C_e is the solute concentration at a plane interface in the matrix in equilibrium with particle of infinite radius, C_r is the solubility at the surface of a sphere particle with radius r, γ is the specific interfacial energy of the matrix-precipitate particle boundary, Ω is the main atomic (or molar) volume of the particle, R_b is the universal gas constant $(8.314 \times 10^3 J/(K \cdot kmol))$ and

T is the absolute temperature. The difference between C_r and C_e induces a diffusive flux of atoms from the smaller particles to the larger particles. Thus the average radius of particle increases and the total number of particles decreases with time. The Gibbs-Thomson relationship is the basic equation for further analysis.

Theories of particle ripening must be statistical in nature since experimental data are essentially statistical. There are three equations to be considered. The kinetic equation which describes the growth or shrinkage rate of an individual particle, the continuity equation which describes the temporal evolution of distribution function of particle size, and the mass conversation equation which requires the total volume of particle remains constant during ripening.

These three equations are the fundamental equations for quantitatively describing the ripening process and are the basis for the LSW and Vengrenovich's theories. They are also used to develop new models to simulate and explain the experimental results in this work.

2.4.1 The kinetic equation

The equilibrium concentration C_r at the boundary of a particle is related to the particle radius by

$$C_r = C_\infty + \frac{\alpha}{r}, \tag{2.22}$$

where C_∞ is the concentration of the saturated solution, $\alpha = (2\sigma/kT)\upsilon C_\infty$ is a parameter containing the inter-phase surface tension σ and υ is the atomic volume of solute. Ignoring the interaction between particles, the diffusion current of solute across the particle boundary per unit area is

$$j = D\frac{\partial C}{\partial r}|_{r=r} = \frac{D}{r}(C - C_r) = \frac{D}{r}(\Delta - \frac{\alpha}{r}). \tag{2.23}$$

Then the particle radius varies with time:

$$\frac{dr}{dt} = \frac{D}{r}(\Delta - \frac{\alpha}{r}), \tag{2.24}$$

where Δ is the concentration difference between particle and saturated solution. It is clear that there is a critical radius $r_c = \alpha/\Delta$ with which a particle is in equilibrium with the solution. If $r > r_c$, particle grows, otherwise particle dissolves. Note that both r_c and Δ vary with time. This is the key point that will be used to explain the experimental results which QDs dissolve due to In desorption and In-Ga interdiffusion in chapter 6.

2.4.2 The continuity equation

The morphology of the dispersed particles is characterized in terms of particle radius distribution $f(r,t)$. The particle radius distribution $f(r,t)$ is the number of particles per unit volume at time t in a size class r to $r + dr$. Thus, the flux of particle passing through a size class r to $r + dr$ is $f \cdot dr/dt$. Therefore, the time rate of change of f is given by the following continuity equation [52]

$$\frac{\partial f}{\partial t} + \frac{\partial(f dr/dt)}{\partial r} = 0. \tag{2.25}$$

The value of the mean-field concentration in the matrix required in the kinetic equation follows from a constraint that the total number of particle must be conserved and the mass conservation condition must be added explicitly.

2.4.3 The mass conservation equation

For all theories describing the Ostwald ripening of particles, the total volume of particles remains constant and can be expressed as:

$$Q = G \int_0^\infty r^3 f(r,t) dr, \tag{2.26}$$

where G is a geometrical factor depending on the particle morphology and $f(r,t)$ is the distribution function of particle size.

During post-growth annealing of InAs QDs at low temperatures, the mass conservation of particles is satisfied and Vengrenovitch's theory can be used (chapter 5). While the total mass of particles decreases with annealing time for InAs QDs annealed at high temperature. At present, no theory considering the change of total mass of particles during ripening is developed. However, the results can be explained by using the kinetic equation (chapter 6).

2.4.4 The results of LSW theory

Based on above three fundamental equations, LSW gives the volume distribution function and a mean radius of particle as a function of time. With large time, the mean radius of particle tends asymptotically to depend on time as $t^{\frac{1}{n+1}}$. $n = 1, 2$ or 3 corresponds to different ripening mechanisms. The distribution function of particle size approaches a certain universal function with the passage of time.

For obtaining these conclusions, it is assumed that the shape of particles is sphere, no strain and interaction between particles were considered, and the degree of supersaturation is small (i.e. $\triangle = C - C_\infty \ll 1$). Lifshitz et al. claimed that the effects of the non-spherical nature and the effect of internal strain can all be taken into account simply by the use of effective parameters in place of certain quantities. The form of the distribution function is unaffected by these assumptions. However, the assumption that the degree of supersaturation is small (i.e. $\triangle = C - C_\infty \ll 1$) limits the theory to describe the dilute systems.

2.4.5 The theory for semiconductor dots

In the frame of LSW theory, Vengrenovich developed the theory further to the solid crystalline phase [53, 54]. For obtaining the maximum radius r_g of particle during annealing, he used

$$\frac{d}{dr}(\frac{\dot{r}}{r})|_{r=r_g} = 0, \tag{2.27}$$

instead of

$$\frac{d}{dr}(\dot{r})|_{r=r_g} = 0, \tag{2.28}$$

with

$$\dot{r} = \frac{dr}{dt} = \frac{\Lambda_n}{r^n}(\frac{r}{r_k} - 1), \tag{2.29}$$

where r_k is the critical radius, Λ_n is a constant that is different for different ripening mechanisms n. For $n = 1$, describes that coarsening is limited by a kinetic process. For $n = 2$ and 3, ripening is controlled by diffusion on the surface and along the dot boundaries, respectively. At the end, the maximum radius of particle is

$$r_g^{n+1} - r_{0g}^{n+1} = \Lambda_n \cdot \frac{n+1}{n} \cdot t, \tag{2.30}$$

where r_{0g} is the initial value of the upper particle size. Therefore, the mean dot size $\bar{r}$ as a function of time are derived as $\bar{r} \propto t^{\frac{1}{n+1}}$, $n = 1, 2$ and 3 corresponds to three ripening mechanisms.

To get the distribution function of particle radii $f(r, t)$, it is convenient to choose the ratio of the particle radius to its maximum radius as a dimensionless variable. Then the distribution function can be written as

$$f(r, t) = \phi(r_g) \cdot g(u), \tag{2.31}$$

where $u = r/r_g$. r_g can be determined from the mass conservation equation. Instead of using assumption as LSW theory, Vengrenovich uses $dC_{ave}/dt = 0$ as a basis for equation (2.29) and removes the restriction that the theory is limited to dilute systems. Using the mass conservation written as

$$\varphi = \frac{4}{3}\pi \int_0^{r_g} r^3 f(r, t) dt. \tag{2.32}$$

and substitution of (2.31) into (2.32) yields

$$\phi(r_g) = \frac{Q}{r_g^4}, \tag{2.33}$$

where

$$Q = \varphi / [\frac{4}{3}\pi \int_0^1 u^3 g(u) du]. \tag{2.34}$$

Finally using

$$f(r,t) = \frac{Q}{r_g^4} g(u), \quad \dot{r} = \frac{(\frac{r}{r_k} - 1)\Lambda_n}{r^n} \tag{2.35}$$

and substituting the corresponding variable in the continuity equation, $g(u)$ is obtained. The detailed structure of $g(u)$ will be given in chapter 5 where it will be used to fit the film force curves.

Chapter 3

Experimental procedure

In this chapter, the MBE system and the growth process will be presented. Some perspectives of the techniques which were used for *in-situ* and *ex-situ* characterization during growth and post-growth procedures will be described. Especially the *in-situ* intrinsic stress measurement (ISM) which is the major technique will be introduced in a detail.

3.1 Sample preparation

3.1.1 Molecular beam epitaxy system

All experiments were performed in a CreaTec custom-built solid source ultra-high-vacuum (UHV) MBE system equipped with a cantilever beam measurement (CBM) setup to measure the stress evolution *in-situ* during film deposition, growth interruptions and annealing. The MBE system is composed of a load lock chamber, a transfer chamber, a bake chamber, and a growth chamber, as shown in Fig. 3.1. The load lock chamber is used to load a new substrate which is mounted on a special sample holder. Two turbo molecular pumps were used to achieve the pressures down to 10^{-8} mbar in the chamber. The transfer chamber is a mediate chamber for transferring samples from the load lock chamber to the bake chamber and to the growth chamber and vice versa. An ion getter pump was used to pump it. Both the baking and the growth chambers are equipped with an ion getter pump together with a sublimation getter pump. The baking chamber was used to degas and to desorb water from the substrates prior to growth. To achieve this, the samples were heated up to about 300 °C for about one to two hours. The growth chamber is designed for growth InAs and GaAs materials and is equipped with three solid source effusion cells for gallium, arsenic and indium, respectively.

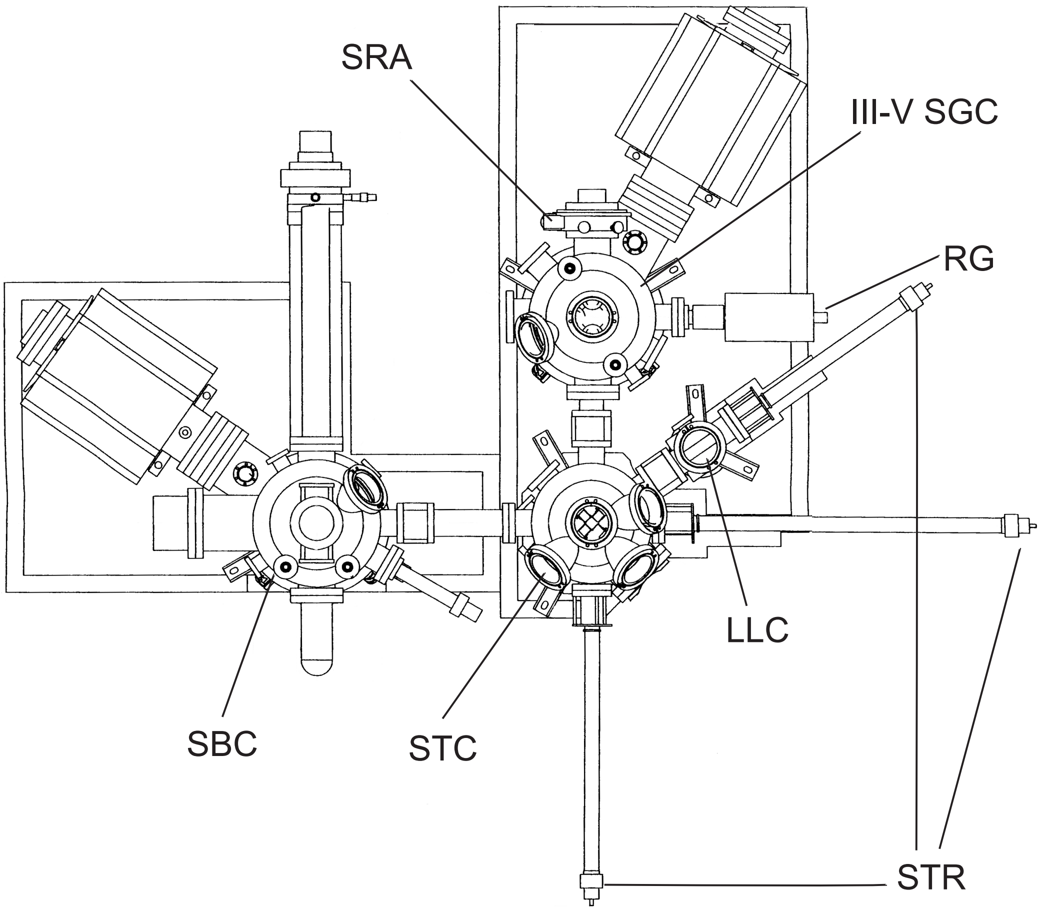

Figure 3.1: Top-view of the custom-built molecular beam epitaxy system showing different chambers. III-SGC: III-V compound semiconductor growth chamber, STC: sample transfer chamber, SBC: sample bake chamber, LLC: load lock chamber, STR: sample transfer rod, SRA: sample rotation assembly, and RG: RHEED gun.

Two standard single heating zone cells were used for Ga and In source materials while a valved dual heating zone cell was used for As source material. The entire inner surface of the growth chamber is encompassed by a cryoshroud which was cooled by liquid nitrogen in order to prevent the desorption of particles from the chamber walls and to achieve a better base pressure, which was on the order of 10^{-10} mbar with the effusion cells at standby temperatures (600 °C for Ga, 300 °C for In and 100 °C/150 °C for As, respectively). By increasing the temperature of the effusion cells, thermally induced atomic or molecular beams of the constituent elements are generated. The growth is proceeding by these atomic or molecular beams impinging on the surface of the substrate which is kept at an elevated temperature, which was measured by a thermocouple. Samples were typically grown with the temperatures of the effusion cells around 1000-1100 °C for Ga, 750-850 °C for In and 300-350 °C/ 450-550 °C for As, respectively. The growth was monitored by reflection high energy electron diffraction (RHEED) to determine the film quality, to calibrate an approximate substrate temperature and to monitor the transition from two-dimensional to three-dimensional growth during the deposition of QD structures. More details on the film growth and the calibration will be given in the next section.

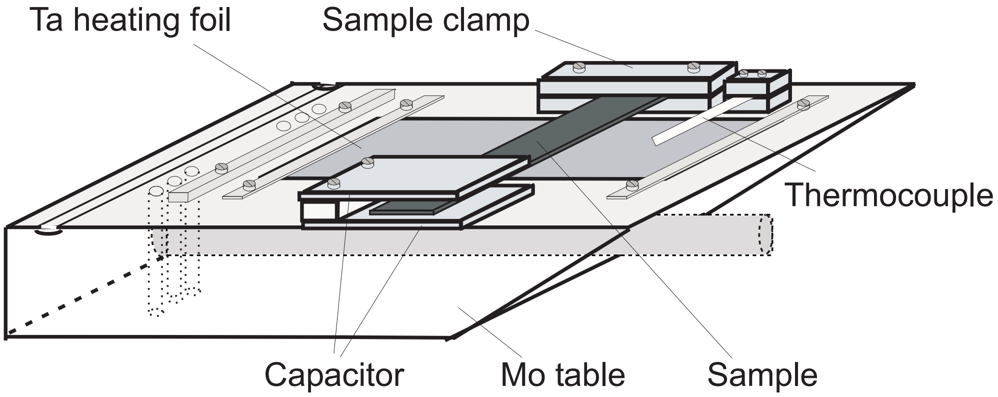

Figure 3.2: Schematic drawing of a sample holder for the cantilever beam measurement.

In order to measure the stress evolution *in-situ*, a cantilever beam technique was used in this thesis for which a special sample holder is needed, as shown Fig. 3.2. A Mo table that can be easily transferred between the chambers is used to fix the substrate, the substrate heater and the CBM setup. During stress measurements, the substrate is clamped on one side and the other side is allowed to bend freely. Due to the lattice mismatch between the substrates and epi-films, the substrates bend and this deflection is measured with a capacitive technique, i.e. the freely movable end of the substrate is placed within two capacitor plates. Enough space should be left from sample to the two plates because the sample should not touch the two plates during measurements. A thin Ta foil is located underneath the sample as a heating unit. A thermocouple and all electrical connections are further fixed on the sample holder. Although the CBM setup has shown to yield high resolution with the capability to calibrate the deflection carefully by measuring the self-deflection of the substrate without deposited film, there are several issues with this concept. The major disadvantages are the highly complex setup which stops functioning in some simple cases such as a disconnected wire, the inability to rotate the substrate during growth, which reduces the capability to grow homogeneous films, especially on the substrates such as GaAs(110) or GaAs(111)A or GaAs(111)B, and the difficulties in aligning the electron beam of RHEED through the capacitor and shielding mask. However, the still smooth and uniform films can be achieved by keeping the deposition area fairly small (3×4 mm^2) in this work. It could be shown by several techniques that the films obtained in this thesis were uniform.

3.1.2 Growth procedure

Prior to the growth, the epi-ready substrates were loaded in load lock chamber. When the vacuum in load lock chamber is lower than 5.0 $\times 10^{-8}$ mbar, the sample was transferred through the transfer chamber into the baking chamber. There the substrate was degassed for one to two hours at around 300 °C. After degassing, the sample was then transferred to the growth chamber followed by heating at 605-610 °C for 15 minutes to remove the top oxide layer under an As pressure of about 2×10^{-6} mbar. The exact temperature during this step varied slightly depending on which sample holder was used. Using RHEED, one can determine if the oxide layer has been removed and therefore can correlate this fixed, well known oxide desorption temperature to the measured thermocouple temperature. RHEED is widely used as an *in-situ* analytical technique in MBE systems because it allows direct measurements of the surface structure of the substrate wafers and the already grown epilayers during deposition, as it doesn't block the growth direction which is vertical to the surface of the crystal. For doing RHEED measurements, a high energy electron beam is directed to the sample surface at a grazing angle. The electrons are diffracted by the crystal structure of the sample and then impinge on a phosphor screen mounted opposite to the electron gun. The energy of electron beam is typically in the range of 5-40 KeV and the incident angle is 1°-3° to the substrate surface. Due to grazing incident angle, the penetration of the beam into the surface is low, being restricted to the outermost few atomic layers. Most geometrical aspects of the diffraction pattern can be interpreted on the basis of a limited penetration scattering model, i.e., a model which is kinematic in the diffraction sense. In this model, the RHEED features (in another word, RHEED pattern) is obtained when the following condition is satisfied:

$$k_e - k_0 = G, \tag{3.1}$$

where k_e is the wave vector of the diffracted electron beam and k_0 is the wave vector of the incident electron beam, G is the reciprocal lattice vector of the sample surface. Therefore, for an amorphous top layer such as an oxide, no diffraction pattern shows and only a diffuse background is visible. However, once the oxide is desorbed, bright spots appear on the RHEED phosphor screen wherever the above diffraction condition is satisfied. After removal of the oxide, a buffer layer was deposited in order to obtain a smooth layer for the subsequent InAs growth. Again, RHEED was used to obtain another temperature calibration point by observing a change in the surface reconstruction taking place around 450 °C depending on the substrate holder. All the temperatures in the following are adjusted to the real value by using the above RHEED/temperature calibrations. The GaAs buffer layers on the GaAs(001) substrates were grown by two steps. In the first step, a 180 nm thick GaAs film was deposited at 480 °C, then, in the second step, 360 nm GaAs were grown at 585 °C followed by annealing at 605-610 °C for 10 minutes. This two-step procedure has been shown to yield very smooth surfaces with a roughness less than 1 nm over (10 μm)^2 as obtained from the atomic force microscopy (AFM) measurements. To confirm that the films were flat and smooth, RHEED was used after the annealing step. Conceptually, perfectly flat surfaces result in a diffraction pattern which exhibits spots arranged on Laue rings. However, no experimentally prepared surface is perfectly flat but is somewhat rough. For such surfaces, the diffraction pattern is produced by transmission through the non-idealities on the surface and streaks appear instead of spots [55, 56]. These streaks, however get shortened again to spots if the surface becomes too rough again. Detailed theories on RHEED can be found in [56, 57] and will not be discussed here. Observing streaks in RHEED during MBE growth is typically considered as a good sign of a smooth surface. In this study, by observing the diffraction patterns of RHEED, the surface quality of samples was characterized for further epi-growth of InAs. The top part of Fig. 3.3 shows the typically observed RHEED patterns of a sample with a smooth surface. In this case, it is measured during the deposition of the smooth two-dimensional InAs wetting layer on the GaAs buffer prepares as described above.

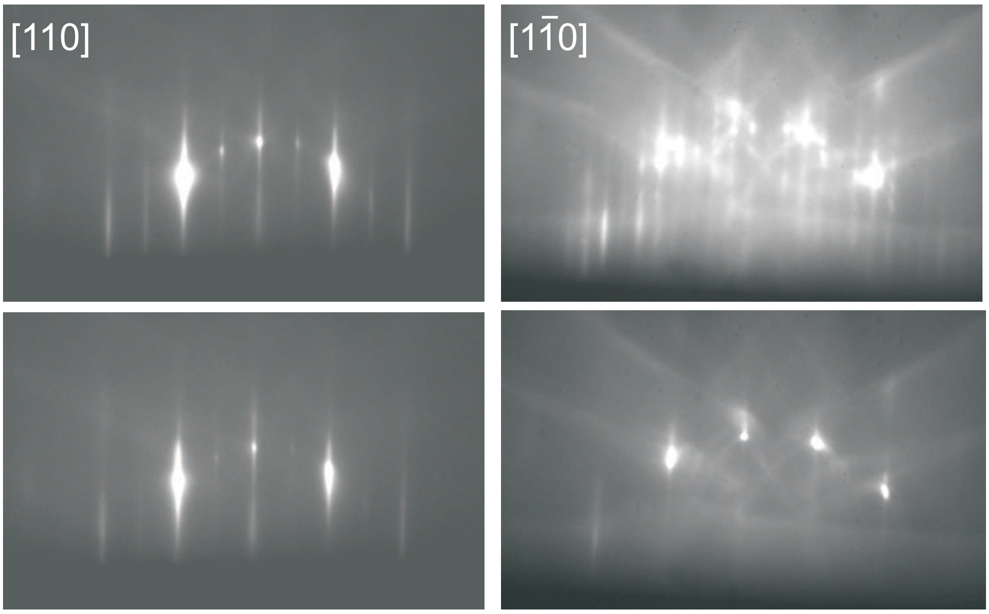

Figure 3.3: Images of RHEED patterns taken in two azimuths before growth (top row) and after deposition of 2.1 nm InAs (bottom row) on GaAs(001) surface.

After deposition of the GaAs buffer layers, InAs layers were deposited. These layers were grown at various substrate temperatures and As pressures for different studies. Under As-rich conditions, InAs quantum dots were formed on top of a wetting layer in a SK growth mode. The exact critical thickness was obtained by monitoring the RHEED transition from streaky to spotty patterns as shown in Fig. 3.3. Furthermore, a corresponding kink was observed during measuring the cantilever deflection. A more detailed description of this measurement technique follows in the next section. Under In-rich conditions, no such transition was observed in RHEED due the continued layer-by-layer growth mode. The detailed growth conditions will be given in the corresponding chapters.

The deposition of the GaAs buffer layers and especially the InAs layers required a detailed and careful calibration of the growth rates. The growth rates were determined by depositing a sequence of alternating layers of GaAs and InGaAs with low content In. The In content in the InGaAs layers had to be low to avoid the formation of defects or to avoid a transition from a 2D smooth film growth to a 3D island growth due to the large lattice mis-

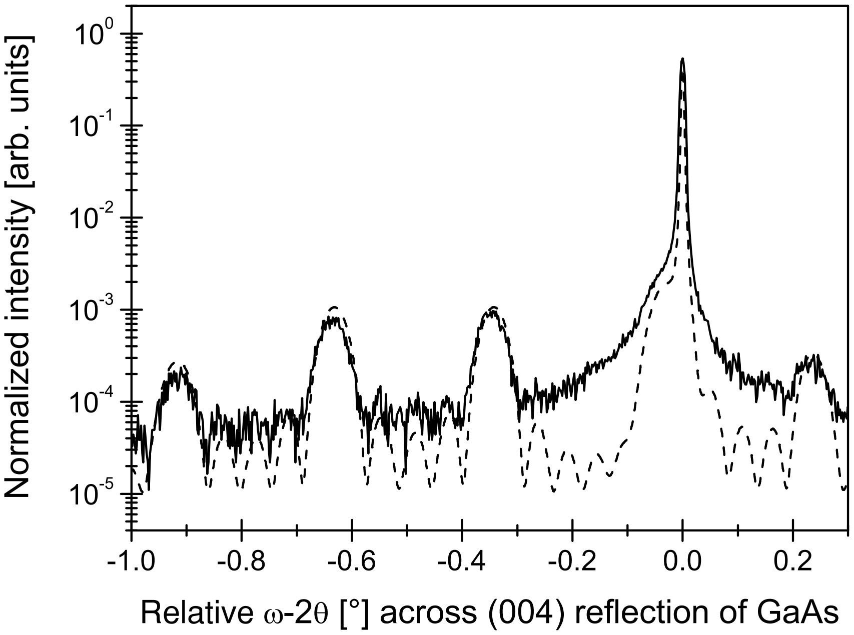

Figure 3.4: ω-2θ x-ray diffraction measurement (solid line) around the (004) diffraction peak of a structure containing five sequences of $In_xGa_{1-x}As$ on GaAs(001). The interference peaks left of the main peak are clearly visible. Using a simulation (dotted line) with the MadMax software, the composition and the individual film thicknesses can be obtained.

match between InAs and GaAs. Using the CBM setup, it was possible to determine if the samples were defect free during growth. This result will be shown in the next chapter. The thickness of the epitaxial layers with deposition time is controlled by the arrival rates of III (Ga and In) group materials if the background is kept under As-ambient condition. The arrival rates of III group materials are a function of the temperature of corresponding solid source which is characterized by the thermocouple reading temperature of the sources. For the thickness calibration, the above layers were grown under As-rich conditions. By using x-ray diffraction and a corresponding simulation, as shown in Fig. 3.4, it is possible to determine the thicknesses of the GaAs and $In_xGa_{1-x}As$ layers as well as the $In_xGa_{1-x}As$ composition. For this purpose, a ω-2θ scan was performed across the (004) reflection of GaAs. The intention is to measure the interference peaks to the left of the main peak and then to simulate the x-ray pattern with the software, such as MadMax. By fitting a simulated pattern to the experimental pattern, a fairly accurate determination of the individual layer thickness and the In content is possible. By knowing the deposition time for each layer, the growth rates can then be calculated. In order to obtain good results, the interfaces between the layers need to be abrupt. This also is one reason that the In content should be low. For the films prepared for this thesis with the corresponding effusion cell temperatures given above, the growth rates were determined to be 0.3 nm/s for GaAs and 0.01 nm/s for InAs, respectively.

3.2 Intrinsic stress measurement using a cantilever beam measurement setup

There are several methods to measure the stress in thin films. For instance, by using electron diffraction such as Spot Profile Analysis Low Energy Electron Diffraction (SPA-LEED) or RHEED to determine the interatomic distance. The strain of the sample can be calculated by measuring the change in distance between atoms, and then can be converted into the mechanical stress [58]. However, this method suffers in the resolution and can not be used for the study of sub-monolayer films. Therefore, another method was developed according to Stony theory: the strain of a film is inversely proportional to the curvature radius of the film [59].

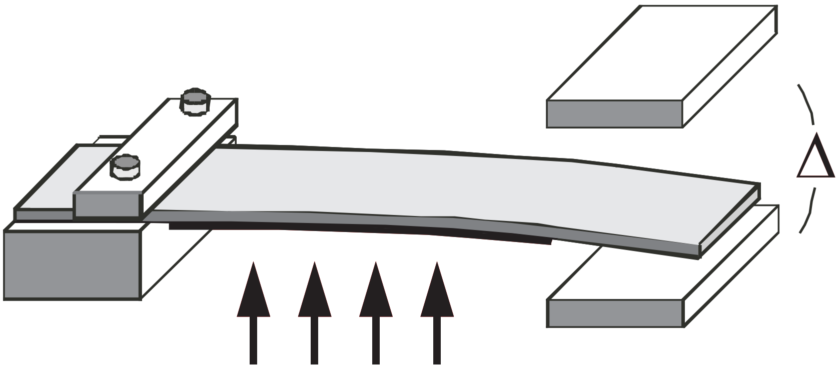

Figure 3.5: Stress measurement with the cantilever beam measurement setup. The deflection at the free end of the substrate is detected by means of a differential capacitor setup.

The curvature radius of the bending of a substrate is measured, then using Stony equation to relate it to the stain on the substrate. The bending curvature radius of the substrate can either be measured by optical method [60, 61, 62] or electronic method [63]. The optical measurement is performed with a set of laser beams [64]. In this study, the electronic method was used. The details of this way is explained in the following. The deflection of cantilever is measured in such a way: the substrate is clamped on one side and the other side can bend freely. As shown in Fig. 3.5. The deflection of the substrate is measured using a capacitance technique combined with a lock-in assisted signal detection. The freely bendable end of the substrate is placed between two plates of a capacitor and acts as a third plate, whose position can be determined accurately by a phase-sensitive lock-in setup which yields a high accuracy. In the case of heteroepitaxial growth, the deflection of substrate is directly correlated to the strain in the epitaxial film. A quantitative description about the mechanical strain of the grown material can be obtained as the following. Assuming that the film thickness t_f is small compared to the substrate thickness t_s, the resulting strain in the film σ_F is inversely proportional to the curvature radius R of the substrate [59]. For a cantilever beam (substrate) with the length of about 25 mm, the smallest deflection that can be measured accurately is about 0.5 nm which corresponds to a torque of about $2.5 \times 10^{-10} N/m$. This means that even the intrinsic stress of sub-monolayer thick films can be measured. Considering the strain in the direction perpendicular to the clamped end of substrate υ_s, the strain σ_x along the long axis of the cantilever is given by [65, 66, 67, 68]:

$$\sigma_x = \frac{Y_s \cdot t_s^2}{6 \cdot (1 - \upsilon_s) \cdot t_f} \cdot \frac{1}{R_x}, \tag{3.2}$$

where Y_s is the Youngs modulus of the substrate.

The deflection of the cantilever ∇_z inside the capacitor is composed of two parts, z_R and z_{cmeas}. z_R is caused by the deflection of the substrate due to the strain from the deposited film. z_{cmeas} is due to the not covered end piece of the cantilever which continues with the slope at the end part of the film, as depicted in Fig. 3.6.

$$\triangle_z = z_R + z_{cmeas} \approx \frac{l_f^2}{2 \cdot R_x} + \frac{l_f}{R_x} \cdot l_{cmeas} = \frac{1}{2 \cdot R_x}(l_f + 2 \cdot l_{cmeas}) \cdot l_f, \tag{3.3}$$

where l_f is the film length, l_{cmeas} is the distance between the end of the

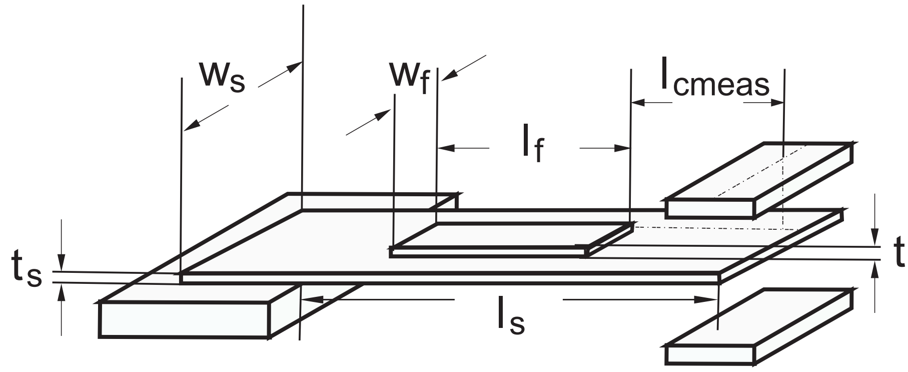

Figure 3.6: Geometry of the cantilever used for quantitative evaluation. Only a part of the cantilever is covered by the epi-film.

film and the middle of the cantilever. For extracting the deflection caused by the epitaxial thin film, the deflection due to the weight of substrate itself should be subtracted. The corresponding torque of a cantilever beam under its own weight is given by

$$T_g(x) = -\frac{1}{2} \cdot \rho_s \cdot g \cdot w_s \cdot t_s \cdot (l_s - x)^2, \tag{3.4}$$

where w_s is the width of the substrate, t_s is the thickness of the substrate, l_s is the length of the substrate and ρ_s is the density of the cantilever beam. g is the acceleration due to gravity [69]. The deflection leads to a moment:

$$T_B = \int_{-\frac{d}{2}}^{+\frac{d}{2}} z \cdot \sigma_x dA = \frac{Y_s \cdot w_s \cdot t_s^3}{12 \cdot (1 - \upsilon_s^2)} \cdot (\frac{1}{R_x} + \upsilon_s \cdot \frac{1}{R_y}) = \frac{Y_s \cdot w_s \cdot t_s^3}{12} \cdot \frac{1}{R_x} \tag{3.5}$$

where Y_s is the Youngs modulus of the substrate, σ_x is the stress with respect to the x-axis. υ_s is the lateral constraction of the substrate, d_A the cross-sectional area of the substrate. Since no deflection are acting in the y-direction, it follows:

$$\frac{1}{R_y} = -\frac{\upsilon_s}{R_x}. \tag{3.6}$$

For the curvature radius, one can use the following approximation:

$$\frac{1}{R_x} \approx \frac{d^2 z}{dx^2}. \tag{3.7}$$

Finally, the deflection of the cantilever beam due to its own weight during the calibration measurement is given by:

$$z_{cal} = \frac{3}{2} \cdot \frac{\rho_s \cdot g}{Y_s \cdot d_s^2} \cdot l_s^4 \cdot (1 - \frac{4}{3} \cdot \frac{l_{ccal}}{l_s}), \tag{3.8}$$

where l_{ccal} is the half length of the piece of substrate inside the capacitor plates. During the calibration measurement, one rotates the substrate by 180 degrees and therefore measures $2 \cdot z_{cal}$.

Finally, combining the equations 3.2 and 3.3 and considering a calibration signal strength S_{cal}, one obtains the quantity $FF = F_F/w_s$, which is called film force, as a function of the measurement signal S_{mess}:

$$\frac{F_F}{w_s} = \frac{\rho_s \cdot g \cdot l_s^4 \cdot (1 - \frac{4}{3} \cdot \frac{l_{ccal}}{l_s})}{2 \cdot (1 - \upsilon_s^{meas}) \cdot l_f \cdot (l_f + 2 \cdot l_{cmeas})} \cdot \frac{Y_s^{meas}}{Y_s^{cal}} \cdot \frac{w_s}{w_f} \cdot \frac{1}{S_{cal}} \cdot S_{meas}. \tag{3.9}$$

A closer look at the formula, the film force FF ($FF = F_F/w_s$) is the force per unit width of the substrate and is measured in this study. A plot of the film force as a function of the film thickness yields a slope which corresponds to the film stress σ_f. Additionally, to use the above equation, it requires the calibration to be performed at the same temperature as the experiment. However, the Youngs modulus does not change strongly with temperature and the calibration measurements performed at various temperatures have shown that there is a negligible influence of the calibration temperature.

3.3 *ex-situ* characterization

All samples were further characterized by *ex-situ* methods such as atomic force microscopy (AFM), transmission electron microscopy (TEM) and photoluminescence (PL). These methods were proved to be very useful to determine the surface morphology, the defect structure and the optical properties of the investigated films. Furthermore, only through the unique combination of these *ex-situ* techniques with the *in-situ* ISM, a detailed analysis and understanding of the growth processes can be obtained. The *ex-situ* methods will be briefly described in a very short manner in the following subsections.

3.3.1 Atomic force microscopy

Typically, an AFM consists of a cantilever with a sharp tip at its end, composed of silicon or silicon nitride with tip sizes in the order of nanometers. When the tip approaches to the close proximity of a sample surface, the Van der Waals force between the tip and the sample leads to a deflection of the cantilever according to Hooke's law, where the spring constant of the cantilever is known. Typically, the deflection of cantilever is measured by using a laser spot reflected from the top of the cantilever into an array of photodiodes. A feedback mechanism is employed to adjust the tip-to-sample distance (or force) to keep the force (or distance) between the tip and the sample constant. Generally, the sample is mounted on a piezoelectric tube, which can move the sample in the z direction for maintaining a constant force, and in the x and y directions for scanning the sample. The resulting maps of the scanning in x-y areas represents the topography of the sample. The primary operation modes of AFM are contact mode, non-contact mode. In the contact operation mode, the force between the tip and the surface is kept constant during scanning by maintaining a constant deflection. In the non-contact mode, the cantilever is externally oscillated at or close to its resonance frequency. The oscillation gets modified by the tip-sample interaction forces. These changes in oscillation with respect to the external reference oscillation provide information about the sample's characteristics.

3.3.2 Transmission electron microscopy

Transmission electron microscopy (TEM) is a powerful instrument to study matter at the nanometer scale. It makes use of high energy electrons to irradiate the thin specimens with the thickness around 0.1 μm or even thinner. The electrons are transmitted and form an image of the specimen magnified by the aid of electron and optical lenses. A high resolution down to atomic dimensions can be reached and a wealth of information about the material structure, such as grain size, crystal defects etc. can be obtained by TEM.

Electron-specimen interaction is the basic of electron microscopy and can be categorized into elastic scattering and inelastic scattering according to energy and momentum conservation. The elastic scattering is caused by the interaction of Coulomb force between the incident electrons and the electrostatic field of the atoms. The elastic scattered electrons are the major source for the image contrast in routine TEM usage such as conventional bright-field, dark-field TEM and high resolution transmission electron microscopy (HRTEM).

The operation mode of TEM is realized by a suitable selection of the size and position of an aperture in the back focal plane of the objective lens. In bright-field imaging, only the transmitted electron beam contributes to the image. The electrons diffracted and scattered at specimen are intercepted by the objective aperture and can not contribute to the image. In the dark-field imaging, the image is generated by the intensity of diffracted electrons.

The size of the objective aperture in bright-field mode directly determines the information to be emphasized in the final image. When the size is chosen so as to exclude the diffracted beams, one has the configuration normally used for low-resolution defect studies, so-called diffraction contrast. In this case, a crystalline specimen is oriented to excite a particular diffracted beam, or a systematic row of reflections, and the image is sensitive to the differences in specimen thickness, distortion of crystal lattices due to defects, strain and bending. Diffraction contrast is a dominant mechanism for imaging dislocations and defects in the specimen.

The diffraction of electrons is purely a result of the wave property of particles. Diffraction contrast mainly reflects the long-range strain field in the specimen and it is unable, to provide high-resolution information about the atom distribution in the specimen. For understanding the HRTEM images, perturbation of the crystal potential on the electron kinetic energy should be considered. Under the phase object approximation (POA), in which the crystal acts as a phase grating filter, the effect of the potential field can be represented by multiplying the wave function by a phase grating function. Thus, the crystal potential is modifying the phase of the incident electron wave. The contrast produced by this mechanism is called phase contrast. Together with the transmitted beam, the structure of the material can be resolved in atomic resolution.

3.3.3 Photoluminescence spectroscopy

Photoluminescence spectroscopy is a contactless, nondestructive method of probing the electronic structure of materials. A laser beam is directed onto a sample, where it is absorbed and imparts excess energy into the material by photo-excitation. The excess energy can be dissipated by the emission of light from the sample. The intensity and spectral content of this photoluminescence is a direct measure of various important material properties. The energy of the emitted light (photoluminescence) relates to the difference in energy levels between the two electron states involved in the transition between the excited state and the equilibrium state. The quantity of the emitted light is related to the relative contribution of the radiative process. The most common radiative transition in semiconductors is between states in the conduction and valence bands, with the energy difference being known as the band gap. Impurity levels and localized defect states in semiconductors also involve into the transition. The photoluminescence energy associated with these levels can be used to identify specific defects, and the intensity of photoluminescence can be used to determine their concentration.

Chapter 4

InAs growth on GaAs(001) under As-stable conditions

The growth of InAs on GaAs(001) under As-rich conditions proceeds in the Stranski-Krastanov (SK) growth mode, i. e. first a two-dimensional wetting layer grows in a layer-by-layer way on top of which InAs quantum dots form after reaching a critical thickness. The critical thickness depends on a number of parameters, such as temperature and flux and it lies at nominal film thicknesses of 1.4-1.8 monolayers for InAs on GaAs(001). During further deposition beyond the critical thickness, the quantum dots grow both due to the arrival of additional material provided by the fluxes as well as due to a ripening process. Without an *in-situ* measurement technique that monitors the growth during deposition, it is very difficult to make conclusions on the growth mechanisms and on the ripening mechanisms. In order to understand the processes involved in the annealing behavior of the dots, it is first required to investigate the processes involved during wetting layer growth and initial dot formation. For this purpose, the stress evolution was measured during the initial growth and was analyzed. In this chapter, the stress evolution is measured by means of the quantity, called film force. Its dependence on the nominal deposited film thickness and on the temporal evolution after growth was analyzed. A correlation of the film force curve to the physical morphology of the epilayers, as well as a comparison of film force curves obtained at different temperature will be shown.

4.1 Stress evolution during InAs wetting layer growth

During the deposition of the InAs wetting layer, a strained film is created on the substrate due to the coherent growth of InAs on GaAs, between which the large lattice mismatch exists. The strained layer results in a bending of the cantilever and is directly measurable with the cantilever beam measurement setup as described in the previous chapter. Figure 4.1 shows a film force curve measured during an initial deposition of roughly 2.1 ML on GaAs(001) at a temperature of 470 °C. As in all following plots of the film force versus nominal film thickness, the slope corresponds to the stress in the epitaxial film. As can be clearly seen, the film force increases linearly up to a thickness of about 1.6 ML.

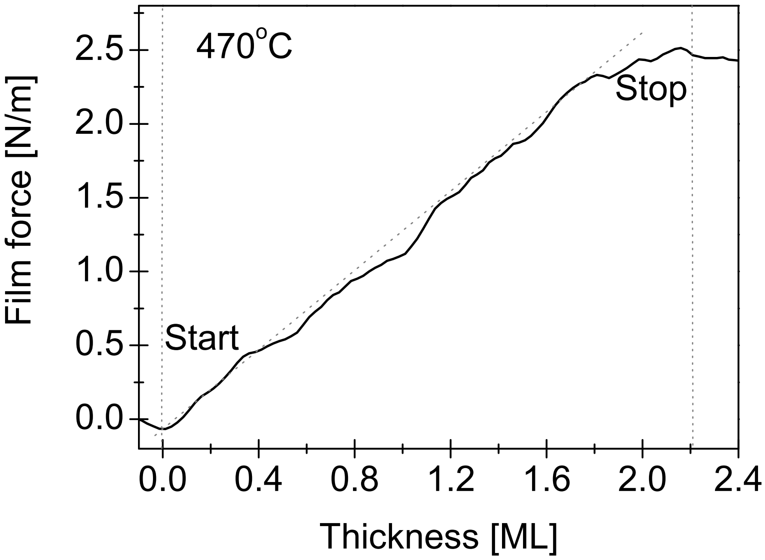

Figure 4.1: Compressive film force measured during initial InAs deposition of roughly 2.1 ML on GaAs(001) at 470 °C.

RHEED (see Fig. 3.3) shows a transition from streaks to spots, indicating a roughening of the surface. Unfortunately, due to special geometry of the sample holder, it was not possible to obtain RHEED pictures good enough to directly measure the critical thickness. Therefore, atomic force microscopy measurements were additionally performed, which show that no quantum dots are visible below this thickness, but are formed above, as shown in Fig. 4.2.

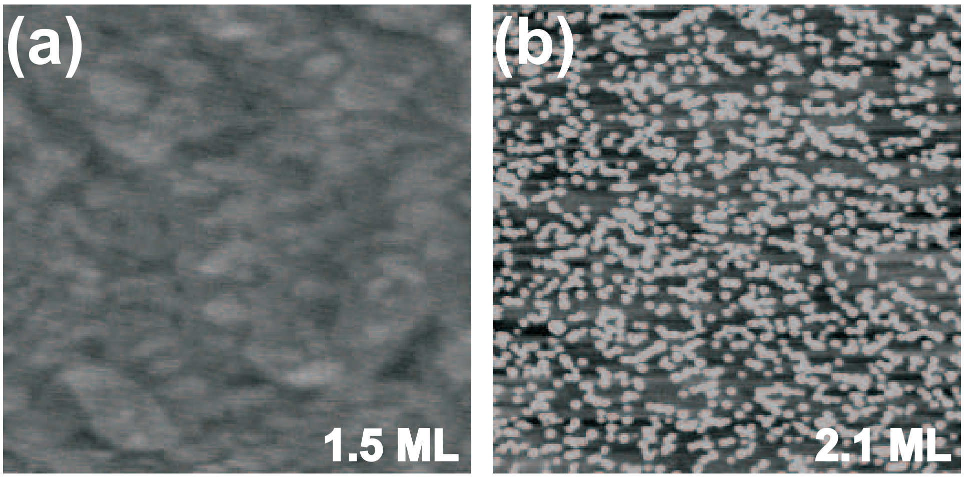

Figure 4.2: 2 × 2 μm^2 AFM images of InAs on GaAs(001) after the deposition of (a) 1.5 ML and (b) 2.1 ML at 470 °C. The grey scale in all images is 2.5 nm.

Using these data, it can be concluded that the kink in the film force curve at around 1.6 ML corresponds to the critical thickness and the linear part below corresponds to the deposition of the wetting layer. Thus, the slope of the linear part of the film force is equal to the stress that is built up in the wetting layer. Quantitatively, the experimental values yield a stress of roughly 4.7 GPa. As introduced in chapter 2, the misfit stress for a coherently grown InAs film on GaAs(001) can be calculated by Eqn. 2.14. Since the measurement was performed at 470 °C, temperature adjusted values for the elastic constants (c_{1111} = 80 GPa and c_{1122} = 45 GPa [70]) and for the lattice parameters(a_{InAs} = 0.607 nm and a_{GaAs} = 0.566 nm, respectively) have to be used, yielding a theoretical misfit stress of about the 5.38 GPa. Given all experimental uncertainty, such as exact measurements of all film dimensions, the calibration method used to relate the cantilever deflection to a film force and the exact film thickness determination, the experimental error can be 10%. Therefore, the experimental value is in fairly good agreement with the theoretical value. This is indeed a surprising result as it seems to imply that the elastic properties of a monolayer are already bulk-like and the influence of surface stress effects is reasonably small, since only a few steps are present on the wetting layer surface, as shown later in Fig. 4.5. The somewhat smaller experimental value might also be explained similar to an argument presented in the literature recently [71], where only a value of 4.1 GPa was measured. A model was used to explain the result, in which not all arriving In is incorporated into the InAs film but rather floats on the surface, thus not contributing to any stress build-up.

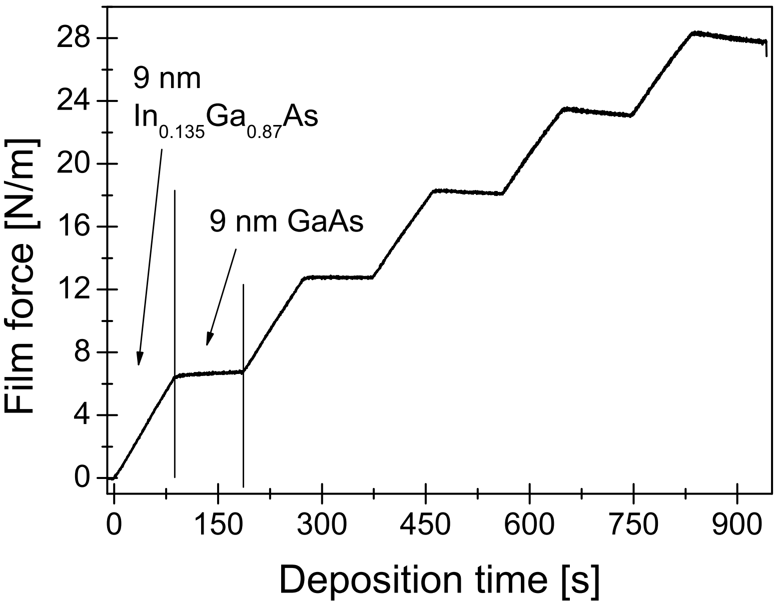

Figure 4.3: Plot of the film force as a function of deposition time measured during the subsequent deposition of five $In_xGa_{1-x}As/GaAs$ double layers. Since both layers grew with different growth rates, the deposition time is used as an x-axis rather than the film thickness. Almost no stress release is detected during the GaAs layer deposition, indicating coherently strained film suitable for x-ray measurements. To obtain the misfit stress in the $In_xGa_{1-x}As$ layers, the film force accumulated during the deposition of this layer needs to be divided by the thickness of the layer obtained from the corresponding x-ray calibration measurement.

Considering the difference between the experimentally observed values of the present work and the above reference, the reference gives a relatively small measured misfit stress. One can assume that different growth conditions did indeed lead to a different amount of In incorporation. Thus, this non-incorporation of In should also have an influence on the samples that were used for growth rate calibration, where a sequence of five alternating $In_xGa_{1-x}As$ and GaAs layers were deposited. Comparing the experimental x-ray measurements with a simulation (see Fig. 3.4), the In composition was determined to around 13.5%. If some In was not incorporated into the film, again this should be detectable in film force curves recorded during the fabrication of these samples (Fig. 4.3). Once again, during deposition of the $In_xGa_{1-x}As$ layer, a linear increase in the film force curve is visible due to the build-up of misfit stress. During the subsequent deposition of GaAs, no further stress is introduced, indicating a coherently grown film structure that is suitable for growth rate calibration. Furthermore, following the above analysis of the misfit stress, it turns out that the experimentally observed value is consistent with an In composition of around 13.5% (within experimental error). Therefore, either more In is incorporated during the growth of an alloy, or the deviation of the measured value from the theoretically is a result of experimental error of the stress measurement method. For the interpretation of the following experiments, no quantitative absolute values are necessary, but rather a comparison between normalized film force curves.

4.1.1 Stress evolution during InAs quantum dot growth

Once the wetting layer is deposited and the critical thickness is reached, the stress in the film is relaxed by the formation of quantum dots. Therefore, with further InAs deposition, the increase of the film force becomes slower and it proceeds with a smaller slope. As can be seen in Fig. 4.1, the average stress after further growth up to 2.1 ML InAs is 3.5 GPa, which is much lower than the theoretical misfit stress. This clearly shows that the formation of dots relieves a great amount of stress.

4.2 Evolution of the film force during annealing

As mentioned in the previous chapter, after the formation of the InAs quantum dots, ripening of quantum dots can occur when the sample is kept at an elevated temperature. Through ripening, partial stress is relieved. Correspondingly the film force accumulated during epilayer growth will decrease. Besides ripening, additional structural rearrangements can occur in the wetting layer that may lead to further reduction of the stress. Possible processes are the introduction of defects such as misfit dislocations or even the desorption of some of the material. In order to analyze the ripening of the quantum dots, it is important to first study the annealing behavior of the wetting layer itself and then to compare it to the annealing behavior of the quantum dots before any detailed model can be introduced. The following sections will give an overview of the annealing behavior of the wetting layer and the quantum dots as a function of annealing temperature. A more detailed investigation on the quantum dots itself will then be presented in the subsequent chapters.

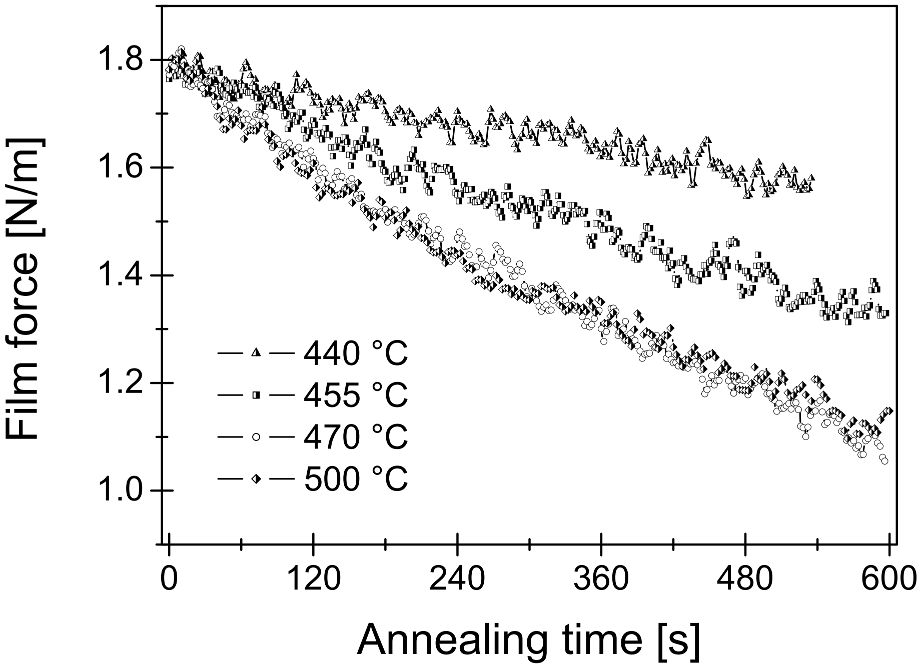

Figure 4.4: Film force curves obtained during annealing of the 1.5 ML thick InAs films, i.e. samples consisting of the wetting layer only. A decrease in the film force during annealing is visible, this effect becomes more pronounced with the increasing annealing temperatures.

4.2.1 Wetting layer

Figure 4.4 shows the film force curves measured during annealing of 1.5 ML thick InAs films, i.e. films composed of the wetting layer only. A decrease of the compressive film force from 1.8 N/m to 1.6 N/m, 1.35 N/m, 1.1 N/m and 1.0 N/m for annealing at 440 °C, 455 °C, 470 °C and 500 °C is observed, respectively.

This decrease corresponds to a relief of the misfit stress accumulated during growth. The small decrease of film force for annealing at low temperatures indicates that the pseudomorphic wetting layer does not change during annealing. This is confirmed by an AFM image taken after annealing for 600s at 440 °C (Fig. 4.5), which shows large terraces on the surface and an identical morphology to AFM images recorded before annealing (not shown).

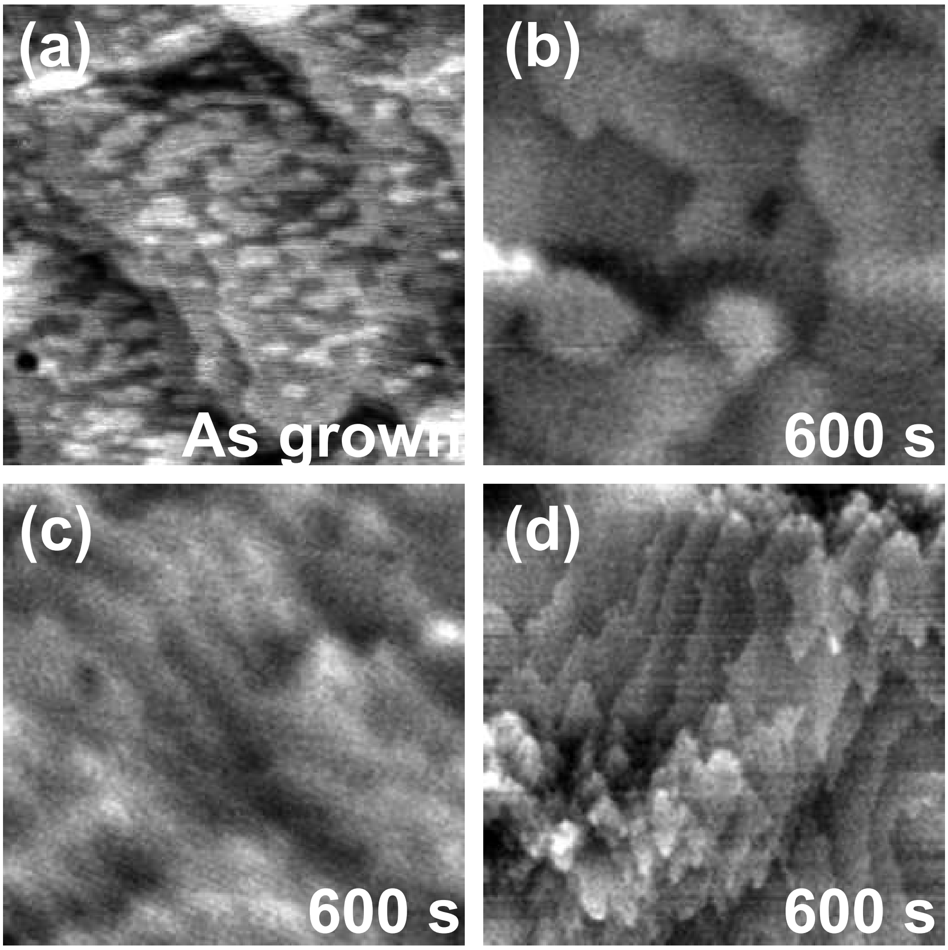

Figure 4.5: 2 × 2 μm^2 AFM images of the wetting layer samples taken (a) before annealing and after annealing for 600 s at (b) 440 °C, (c) 470 °C, and (d) 500 °C, respectively. The grey scale is 1 nm for all the images.

On the other hand, the higher the annealing temperature, the larger the decrease in film force. Corresponding AFM images taken after 600 s of annealing show that the surface contains more steps the higher the annealing temperature, which might be attributed to a mechanism for stress relief. A larger decrease is observed for annealing at 500 °C for 600 s for which film force decreases to about 62% of its original value. Figures 4.5c, 4.5d and 4.5e show the morphology of the wetting layer films imaged by AFM after annealing. Large terraces are clearly seen in the film annealed at 440 °C, while small islands of about 1-2 ML height are visible on the surface of the film annealed at 500 °C. Similar to the transition from 2D layer-by-layer to 3D island growth, these mounts lead to the reduction of the stress observed in the film force curve. However, the formation of these islands is not primarily driven by misfit stress, but rather can be explained as a result of a dewetting process during annealing [72]. According to a theoretical study [73], InAs forms a liquid-like layer on the surface of GaAs at high temperatures above ~500 °C. The resulting high mobility allows In atoms to rearrange on the surface, thus providing a kinetic mechanism for the formation of these mounts. Furthermore, at higher temperatures, it is known that In can desorb from InAs quantum dots, and a similar process could take place here. Since the step edge density increases and mounts similar to quantum dots are formed, the surface area increases and thus the probability for In desorption increases. This would lead to a reduction of the InAs material on the film and thus a reduction of the total stress as measured by the cantilever beam setup.

4.2.2 Quantum dots

A comparison of the film force curves of the quantum dots samples annealed at different temperatures shows clearly that the higher annealing temperature, the more the film force decreases, as shown in Fig. 4.6. Atomic force microscopy images (Fig. 4.7) reveal that for low temperatures, the quantum dots ripen from many small dots to a few very large dots. At high temperatures, the dots are dissolved, probably due to In desorption. In order to understand how the stress relaxation is related to the morphology change of the quantum dots, it is necessary to compare directly the film force curves measured for annealing of film with and without quantum dots, as shown in Fig. 4.8.

For the sample annealed at 440 °C and at 455 °C for ~600 s, the final film force value of the curve measured for the quantum dots sample is higher than the value measured for the wetting layer sample. The two curves proceed with the same slope after 400 s annealing. This indicates that the ripening of quantum dots occurs without involvement of additional material coming from the wetting layer. For the sample annealed at 470 °C, the final film force

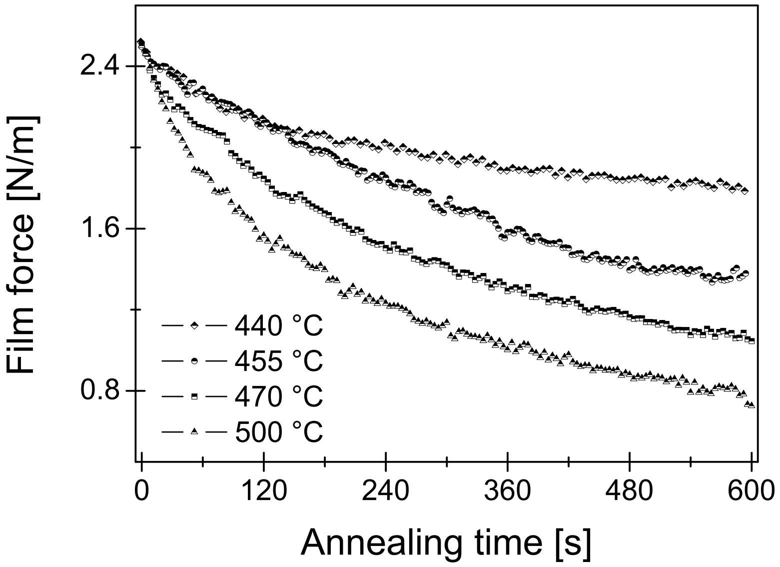

Figure 4.6: Film force curves obtained during annealing of the nominally 2.1 ML thick InAs films, i.e. the samples consisting of the uncapped quantum dots on top of the wetting layer. The film force decreases more with the increasing annealing temperatures.

value of the curve measured for the quantum dots sample is same to the value measured for the wetting layer sample after 600 s annealing, while for the sample annealed at 500 °C, the final film force value of the curve measured for the quantum dots sample is smaller than the value measured for the wetting layer sample after 60 s annealing and continuously drops with annealing time. AFM images of quantum dot samples annealed at 440 °C and 470 °C for 600 s show a typical ripening behavior of quantum dots (Fig. 4.7a and b). The density of dots decreases while the size of dots increases after 600 s annealing. For quantum dot sample annealed at 500 °C, a completely different behavior of quantum dots is observed by AFM image after 600 s annealing. Quantum dots dissolve after 600 s annealing, as shown in Fig. 4.7c. In the following two chapters InAs quantum dots annealed at low temperatures (440 °C, 455 °C and 470 °C) and high temperature (500 °C)will be discussed in detail.
)

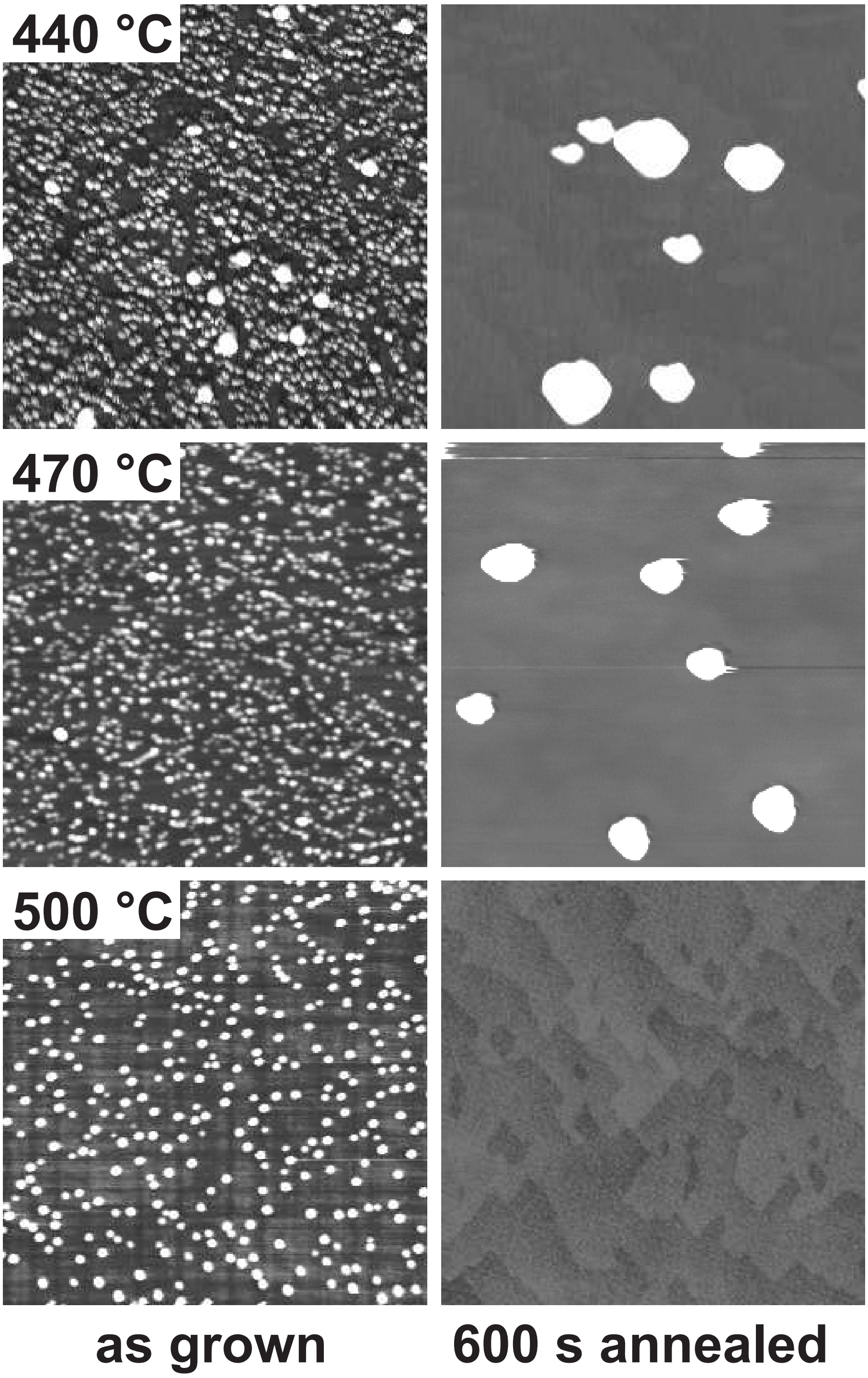

Figure 4.7: $2 \times 2\ \mu m^2$ AFM images of InAs QDs before annealing and after annealing for 600 s at 440 °C, 470 °C and 500 °C.

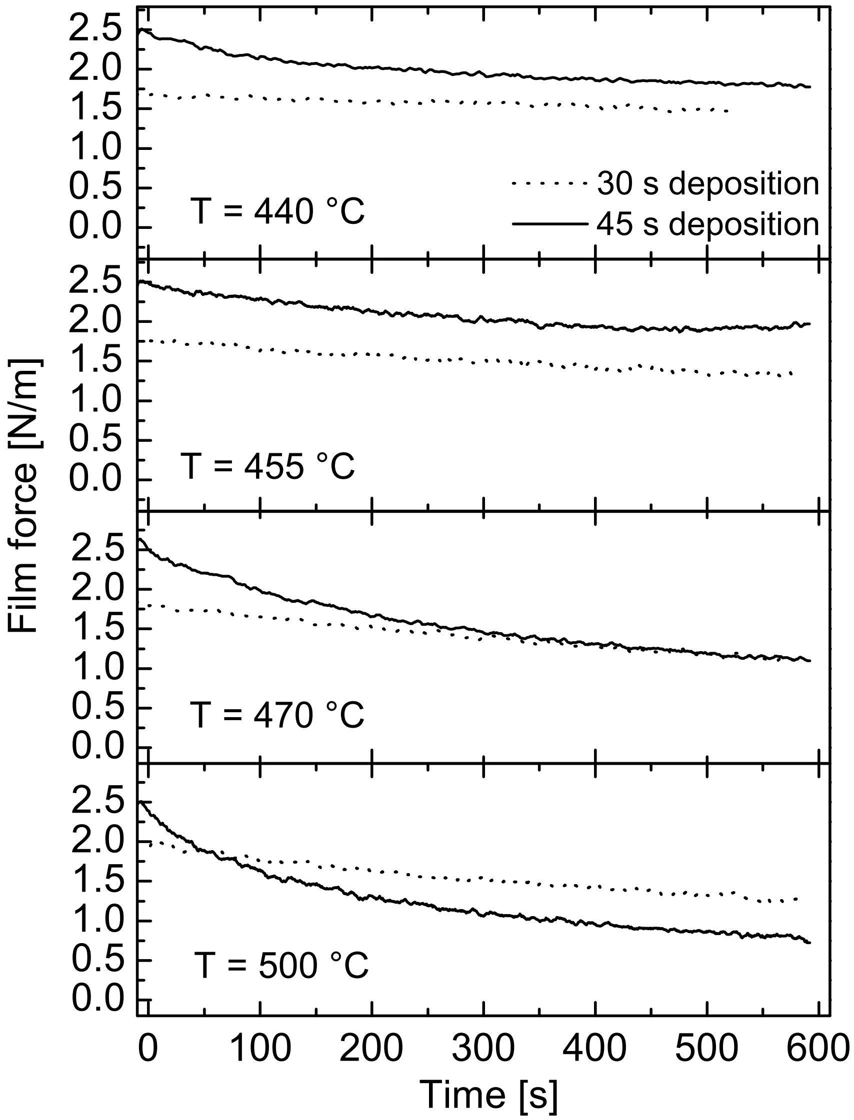

Figure 4.8: Film force curves obtained during annealing of the nominally 1.5 ML and 2.1 ML thick InAs films, i.e. the samples consisting of wetting layers only and wetting layer plus quantum dots, respectively.

4.3 Summary

The film force curves were measured during thin InAs film grown on GaAs(001) under As-stable conditions and the relationship between film force curves and morphology change was explained. The stress obtained by film force curves measurements was compared to the theoretical value for bulk structure. For thin wetting layer, the smaller value of the observed decrease of the film force might be due to the steps on the surface. While for the samples with thicker InAs beyond the critical thickness, formation of dots is an efficient way to relieve the misfit strain. It turns out that at low temperatures, the ripening can be analyzed within the standard Ostwald ripening frame. A detailed modeling of the involved processes is possible and will be presented in the next chapter. However for higher temperatures, a rearrangement of material from the wetting layer and the dots and even In desorption occurs. For these temperatures, modeling of the film force curves is very difficult, even impossible, due to the unknown amount of material transferred between all layers. A qualitative analysis will be given in a later chapter.

Chapter 5

Film force curves obtained during quantum dots annealing at low temperatures

As mentioned in the previous chapter, during annealing of the InAs quantum dots at various temperatures, the film force curves show a relaxation. A quantitative comparison of film force curves of the bare wetting layer films measured at lower temperatures with those of films covered by dots, reveals that the magnitude of relaxation of film force for the films with dots is always larger than that for the wetting layer over the whole annealing range. Since the magnitude of relaxation of film force of the wetting layer films is much smaller compared to the magnitude of relaxation for the quantum dots films during annealing, the major relaxation in the film force curves can be attributed in a first order to morphological changes in the quantum dots layer. As mentioned in the previous chapter, at these low annealing temperatures, the quantum dots experience standard ripening and therefore the film force curves can be analyzed in the standard Ostwald ripening framework. This is consistent with previous reports in the literature where also standard InAs quantum dots ripening was observed [74, 75]. Since individual film force curve can show some deviation in the absolute value, as was in the case of comparing a measured misfit stress with the theoretical equivalent value of a wetting layer, normalized curves will be used in the following analysis, as shown in Fig. 5.1.

An absolute, quantitative treatment would require exact values for the diffusion constant of In and the activation energies for attachment or detachment of material to a quantum dots. Since these values are not known, such an analysis cannot be performed. Fortunately, it turned out that these param-

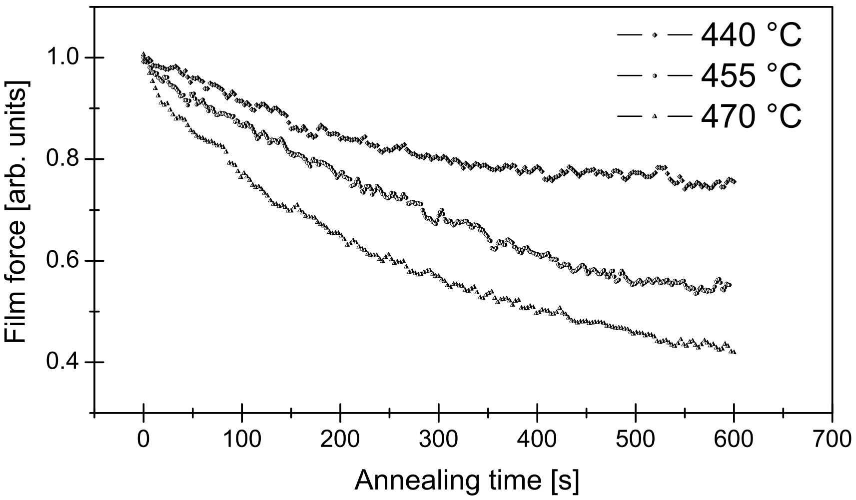

Figure 5.1: Normalized film force curves measured during annealing of 2.1 ML InAs for 600 s at 440°C, 455 °C and 470°C, respectively.

eters are hidden within a scaling factor making it still possible to fit the film force curves. By using such a fitting procedure, it is anticipated that the mechanism for ripening can be determined.

5.1 Experimental results

Figure 5.1 shows the evolution of the normalized film force measured during post growth annealing for 600 s at 440 °C, 455 °C and 470 °C, respectively. Film force of all the three curves decreases with annealing time. After 600 s annealing, the film force decreases from 2.5 N/m which is accumulated during growth to 1.76 N/m and 1.01 N/m for 440 °C and 470 °C, respectively. As mentioned above, the decrease of film force is mainly due to ripening of dots. The ripening behavior is confirmed by a series of AFM images. For the AFM measurements, the samples were annealed for a certain time and then rapidly quenched to room temperature. The AFM data are useful to determine the overall morphological change during ripening, the density of the quantum dots and their size and volume distributions. The AFM images of Fig. 5.2 and Fig. 5.3 show the annealing experiments at 440 °C and 470 °C, respectively.

For both temperatures, a similar morphological evolution is observed. Before annealing, quantum dots are small and the density is high. With annealing

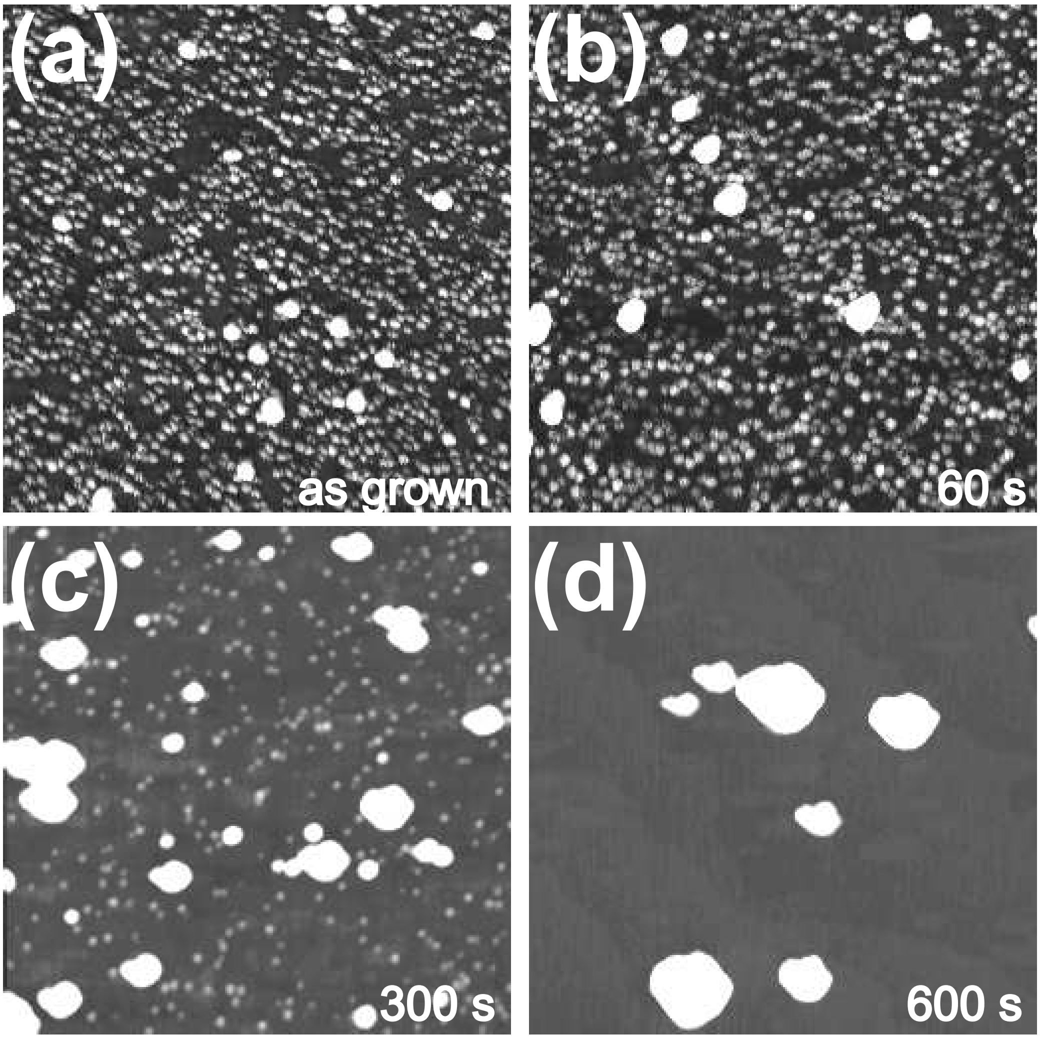

Figure 5.2: $2 \times 2\ \mu m^2$ AFM images of InAs quantum dots deposited for 2.1 ML at 440 °C, taken (a) before annealing, (b) after annealing for 60 s, (c) 300 s, and (d) 600 s. The z-scale in all images is 10 nm.

time, the size and density of big dots increase while the density of small dots decreases. All AFM images reveal a typical ripening behavior of the quantum dots during annealing at these temperatures. A closer look at the AFM images indicates pyramid shaped dots. During ripening, a constant dot height to radius ratio of about 0.2 is measured, yielding an opening of about 11°. This indicates that the dots form initially already as pyramids and then grow by increasing the side facets, yielding a three-dimensional coarsening.

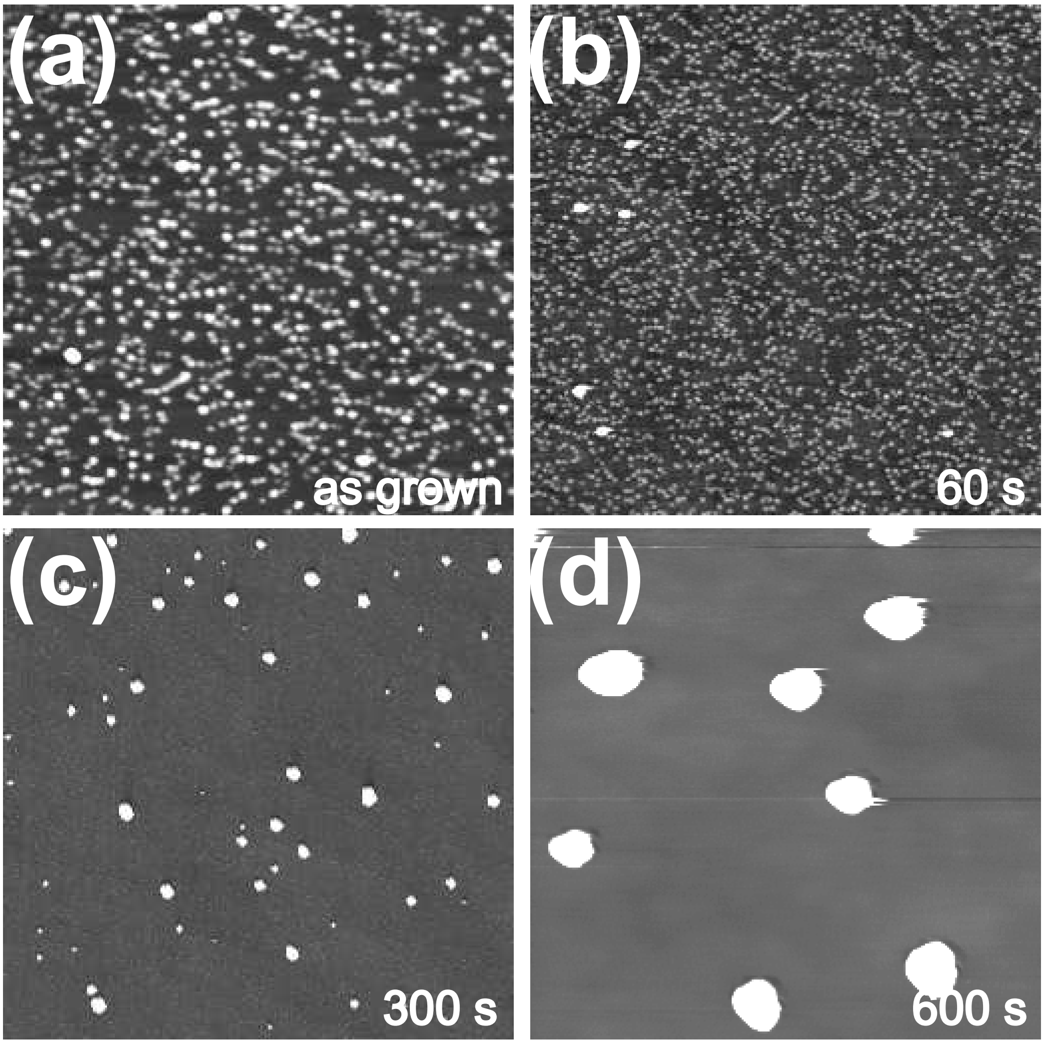

Figure 5.3: 2×2 μm^2 AFM images of InAs quantum dots deposited for 2.1 ML at 470 °C, taken (a) before annealing, (b) after annealing for 60 s, (c) 300 s, and (d) 600 s. The grey scale in all the images is 10 nm.

The film force curves show different degrees of relaxation, but no difference is observed in the atomic force microscopy images of ripened quantum dots at different temperatures. Two possibilities can be considered for the difference in stress relaxation: either defects such as misfit threading dislocations formed in the larger dots during ripening as has been previously published in the literature, or different ripening processes were involved. To exclude the former possibility, several high-resolution transmission electron micrograph studies were performed. However, none of the micrographs showed any sign of dislocation in the larger dots for annealing at higher temperatures where it would be energetically easier to from the dislocations. One can therefore conclude that the dots observed, at least at the beginning of ripening, were still too small to form these dislocations and therefore, the different magnitude of film force decreases at different annealing temperature is due to different ripening mechanisms. To determine the ripening process of quantum dots, investigators often try to fit an experimentally obtained island radius distribution to the LSW theoretical models. However, this procedure does not always yield a clear determination of the ripening process. For instance, for annealing of InAs quantum dots, Krzyzewski et al. [75], using STM images taken at different annealing times, found that the evolution of the average dot size as a function of time cannot be described by any of the the models developed by LSW.

In order to perform modeling to determine the ripening process, it must first be clarified that the total volume of all quantum dots remains constant. If this is not the case, large deviation from standard Ostwald ripening can occur and models, that were for instance used in the previous two references, would fail. The total volume of all quantum dots during annealing was extracted carefully by analyzing a large number of samples specifically prepared for atomic force microscopy studies. The results are shown in Fig. 5.4. As one can clearly see, the total volume for ripening at temperatures below 470 °C remains fairly constant. One can therefore use models for standard ripening. In the following work, by extending the LSW and Vengrenovitch's models, a new approach is presented to determine the ripening process by not fitting only the average dot radius but rather by fitting the complete time evolution of the dot radius distribution function to experimental data. The involved ripening mechanism is determined by fitting film force relaxation curves obtained during the annealing phase of the growth.

5.2 Modeling of film force curves

As introduced in the chapter 2, the classical theory developed by Lifshitz, Slyozov [49, 50] and Wagner [51] is based on the assumption that the total volume of particles remains constant during ripening process. The process proposed by Vengrenovitch [53, 54] which describes ripening of semiconductor quantum dots is derived from LSW theory. In order to realize the simulation, in a first approximation, a constant surface tension σ for the dots is assumed

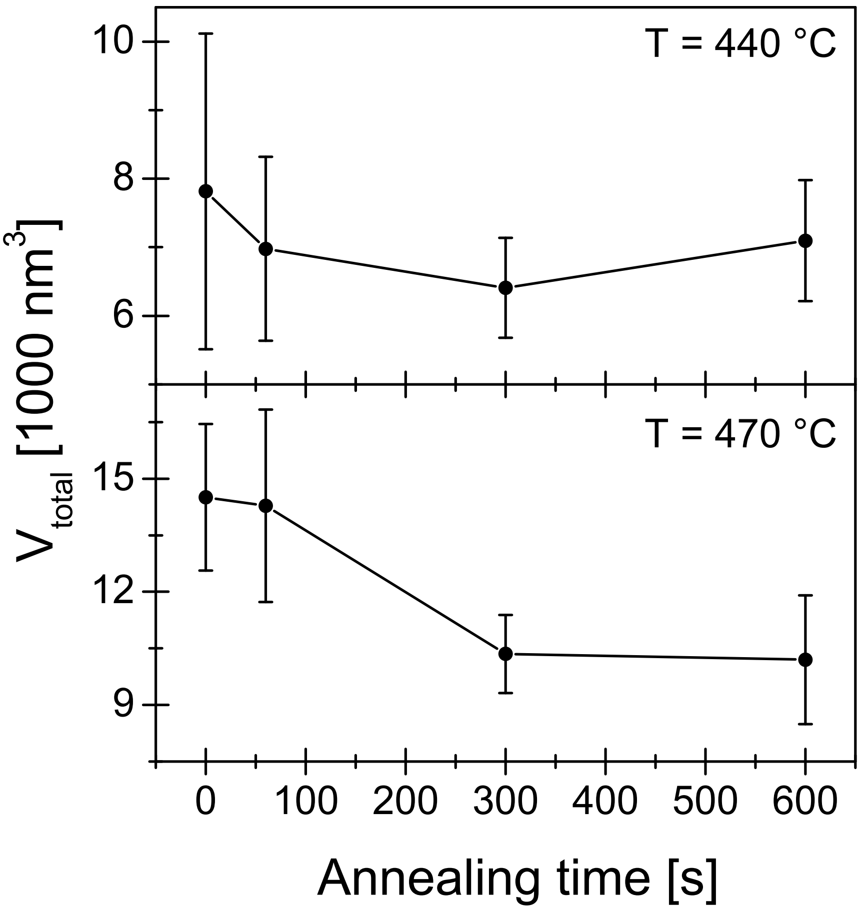

Figure 5.4: The total volume of quantum dots extracted from the AFM images taken at the various annealing stages, (a) for the quantum dots annealed at 440 °C and (b) for the quantum dots annealed at 470 °C.

while the total surface area of the dots A_{dots} is changing with time. For such a situation, the film force is given by

$$FF(t) \propto \sigma * A_{dots}(t)/A_{subs}, \tag{5.1}$$

where A_{subs} is the constant surface area of the substrate. According to the model developed by Vengrenovitch, at a given time t, the maximum radius of the particles r_g is given by

$$r_{g_n}(t) = a_n(t+b_n)^{\frac{1}{n+1}} \quad \text{with} \quad b_n = r_{0g}^{n+1}/a_n, \tag{5.2}$$

where r_{0g} is the initial value of the upper particle size limit for the corresponding ripening mechanism. For n = 1,

$$a_1 = \frac{2\sigma C_x \upsilon_m^2 K}{\nu RT}, \tag{5.3}$$

the ripening will be controlled by attachment or detachment of atoms on the dot surface. For n = 2, the mechanism for quantum dots ripening is limited by surface diffusion of atoms and

$$a_2 = \frac{\sigma C_x \upsilon_m^2 D_\nu}{RT}. \tag{5.4}$$

For ripening controlled by diffusion of atoms along grain boundaries, n = 3 and

$$a_3 = \frac{2\sigma C_x \omega \upsilon_m^2 D_{gb}}{3ABRT}. \tag{5.5}$$

For the already known system, r_{0g} and a_n is constant. The distribution of particle sizes r at time t is then calculated as:

$$f_n(r,t) = const_n \frac{g_n(r/r_{g_n}(t))}{r_{g_n}(t)^4} \tag{5.6}$$

with distribution functions

$$g_1(u) = u(1-u)^{-4} exp(-2/(1-u)),$$

$$g_2(u) = u(1-u)^{-28/9}(u+2)^{-17/9}exp[-2/(3(1-u))]$$

and

$$g_3(u) = \frac{u^3 exp[-\frac{1}{3(1-u)}]exp[-\frac{1}{9\sqrt{2}}arctan(\frac{u+1}{\sqrt{2}})]}{(1-u)^{25/9}(u^2+2u+3)^{29/18}},$$

which were derived by Vengrenovitch [53, 54]. The overall dot surface area $A_{dots_n}(t)$ is then:

$$A_{dots_n}(t) \propto \pi \int_0^{r_{gn}(t)} r^2 f_n(r,t)dr \tag{5.7}$$

During the calculation for each model, a_n is normalized. Different b_n were chosen to fit the experimental curves and get the value of b_n according to the minimum of relative errors.

The calculation results are shown in Fig. 5.5. For annealing at 440 °C, model 3 yields the best fit to the experimental curve, i.e. ripening is controlled by atom diffusion along dot boundaries fits. However, the other two models also closely fit the experimental data. It is therefore difficult to clearly distinguish which mechanism really limits the ripening process of dots or if a combination of two or more mechanisms governs the process. On the other hand, for annealing at 455 °C and 470 °C, model 1 fits the experimental data very well, indicating that the kinetic process, in which attachment/detachment of atoms on the dot surface is the limiting step, is the mechanism for dot ripening. Considering that diffusion is typically a limiting factor at lower temperature and kinetic processes are the limiting factors at higher temperatures, the results appear reasonable. It must be noted, that the film force curves obtained at 455 °C and 470 °C also contain a contribution of changes in the wetting layer during annealing, however these changes are relatively small and are not dominant at the beginning of annealing where the largest change in film force is due to the ripening of the dots. Curves were also fitted for which the contribution of the wetting layer was subtracted and obtained again the same models. This can be explained by the fact that the fits are more sensitive to the beginning part of the film force curves and therefore fitting of the original data sets is still valid. Due to the employed fitting of the experimental data with a model which incorporates the whole time evolution of the dot distribution function rather than only an average dot

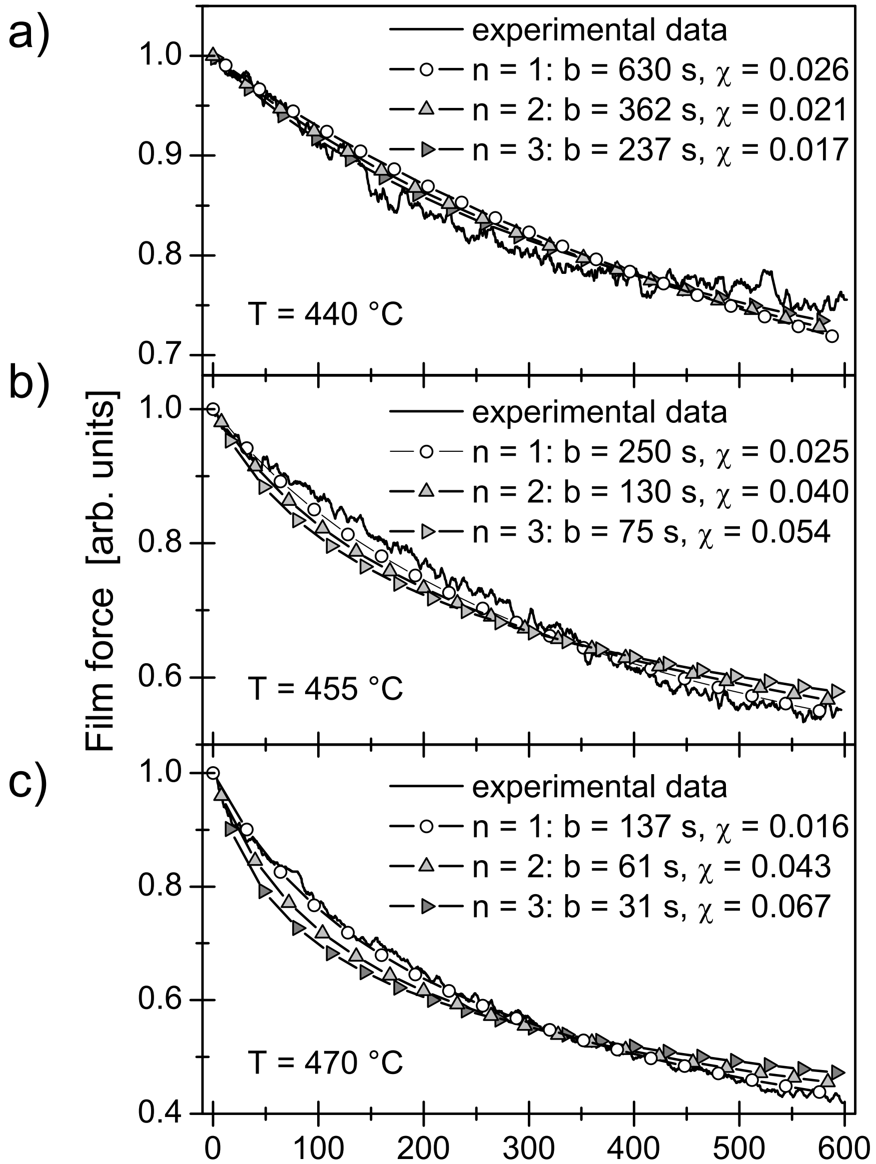

Figure 5.5: Fits to the film force curves measured as a function of annealing time at a) 440 °C, b) 455 °C and c) at 470 °C, respectively.

radius, these results are more compelling in determining the ripening process compared to previously published work.

5.3 Summary

The ripening of InAs quantum dots grown on GaAs(001) substrates was investigated by measuring *in-situ* the film force curve during annealing. A simulation based on Ostwald-ripening was developed that allows a fitting of the relaxation curves and a determination of which mechanism plays the major role. It was found that, for annealing InAs/GaAs(001) at 440 °C, it is difficult to determine the ripening process clearly, but still a model describing ripening controlled by atom diffusion along dot boundaries fits the experimental data best. On the other hand, for annealing at 470 °C, it was found that the ripening process is clearly limited by atom attachment/detachment on the dot surface.

Chapter 6

Film force curves obtained during quantum dots annealing at high temperature

In this chapter, the behavior of InAs quantum dots annealed at high temperature is carefully studied by AFM, film force curves and photoluminescence measurements. It is found that the quantum dots disappear for annealing at temperatures above 470 °C. Based on the above data, a new model is developed to explain the dissolution of InAs quantum dots.

6.1 Experimental results

Figure 6.1 shows the film force curves measured during annealing of a quantum dots sample at 500 °C. During annealing, the film force accumulated during growth decreases. After annealing for 600 s, the film force drops to 62 % of its original value from 2.5 N/m to 0.8 N/m, which corresponds to ~0.57 ML InAs. The film force of a wetting layer sample annealed at 500 °C is measured for comparison with the film force of quantum dot sample. As shown in Fig. 6.1b, the film force of the wetting layer sample decreases less than the film force of quantum dot sample after 600 s annealing. For the quantum dot sample, the film force curve decreases with a gradually decreasing slope and drops to a value lower than the value of the wetting layer curve after 120 s annealing. Then the film force proceeds with the same slope as the wetting layer's after 240 s annealing. The film force of the quantum dots sample decreases more than the film force of wetting layer during annealing, indicating that the existing dots promote the film force decrease.

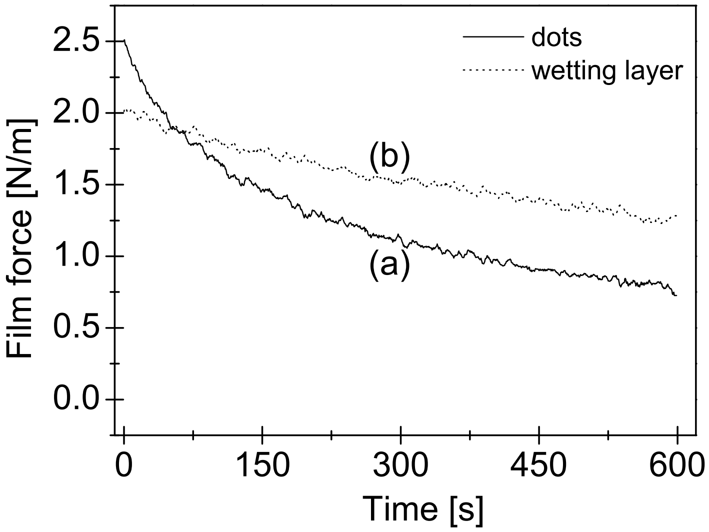

Figure 6.1: The film force measured during annealing of the InAs film for 600 s at 500 °C. (a) 2.1 ML QD film, (b) 1.5 ML wetting layer film.

One possibility for the dots leading to a decrease in the film force is the formation of dislocations during annealing. However, HRTEM images, shown in Fig. 6.2, reveal that every atom is in the perfect crystal site, indicating that there were no dislocations present after dot formation and after annealing procedure. This was confirmed by observing large area scans in titled-plan view geometry, in which no dislocations were found either, as shown in Fig. 6.3.

Another possibility for the additional decrease in the film force of the quantum dots films annealed at 500 °C is desorption of In, which would lead to a continuous decrease in the average height of the quantum dots during annealing. To investigate this possibility, AFM images were recorded at various annealing times. To obtain these AFM images, the samples were annealed for a given time and then rapidly quenched to room temperature.

Figure 6.4 shows these AFM images. The mean radius and height of the quantum dots were extracted from AFM images and are shown in Fig. 6.5 and Fig. 6.6. The mean radius of the quantum dots increases while the mean height of quantum dots decreases after the first 60 s of annealing. With an-

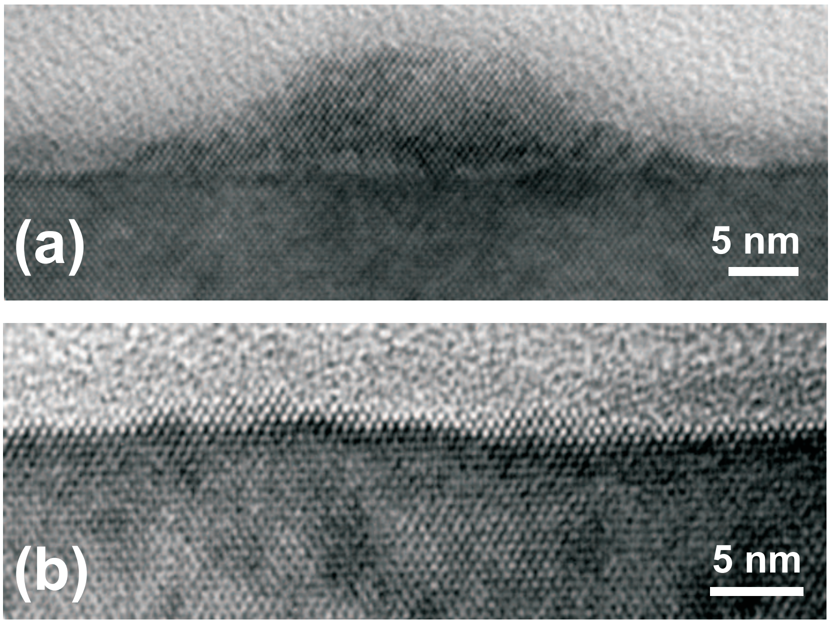

Figure 6.2: Cross-sectional HRTEM images of InAs quantum dots on GaAs. (a) Before annealing and (b) after 600 s annealing at 500 °C.

other 90 s of annealing, the mean radius and the mean height of the dots both decrease. Then the mean radius slightly decreases and the mean height of dots slightly increases followed by the mean height and mean radius of quantum dots remaining almost constant while the density of the dots decreases during further annealing. Eventually the dots dissolve.

6.2 Discussion

For InAs quantum dots on GaAs(001) annealed at high temperature, dissolution of quantum dots occurs as Heyn and Lee et al. [76, 77] observed by reflection high energy electron diffraction (RHEED) and AFM, respectively. They attributed the dissolution of InAs quantum dots to the desorption of In. However, desorption of In alone cannot explain these results. It is usually observed, that during post growth annealing, once a dot grows bigger, its height and radius all increase. Therefore, the increase in mean radius of the quantum dots with a decrease in the mean height of the quantum dots after the first 60 s of annealing indicates that the ripening must be concurrent with the desorption of In. Furthermore, this also indicates that high In concentration on the top of quantum dots. After another 90 s annealing,

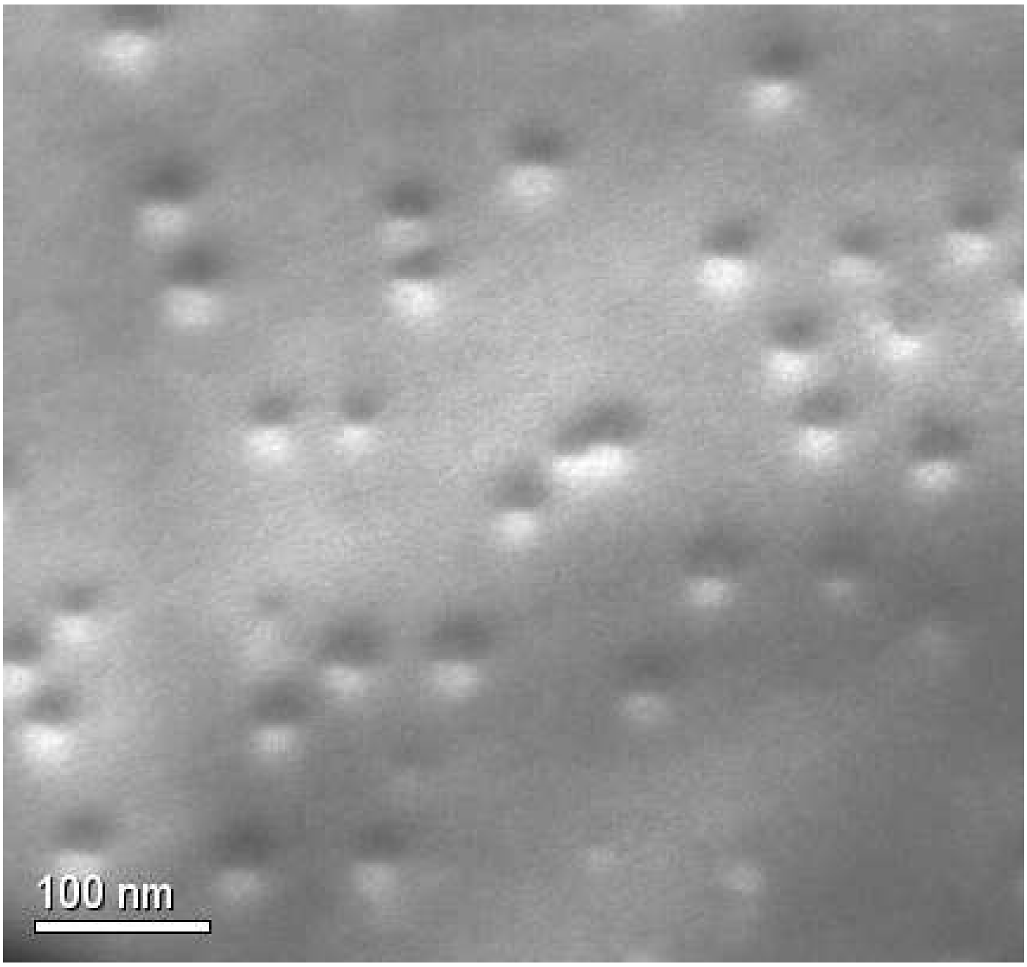

Figure 6.3: (100) plan-view TEM micrography of InAs QDs on GaAs(001).

the mean size and height of quantum dots both decrease. This reveals that during this annealing stage, the desorption of In is still significant and the ripening of the quantum dots is limited because of the decrease of mobility of In due to its desorption. The mean size changes with a larger magnitude than the mean height compared to the changes occurred after the first 60 s annealing, i.e. the mean size and height decrease from 39 nm to 29 nm and from 5.2 nm to 4.6 nm respectively at this annealing stage while the mean size increases from 28.5 nm to 39 nm and the mean height decreases from 7.7 nm to 5.2 nm after the first 60 s annealing stage. This reveals that the dots tend to go into their equilibrium shape under this condition. It is corroborated by the morphological evolution during later annealing stage. As

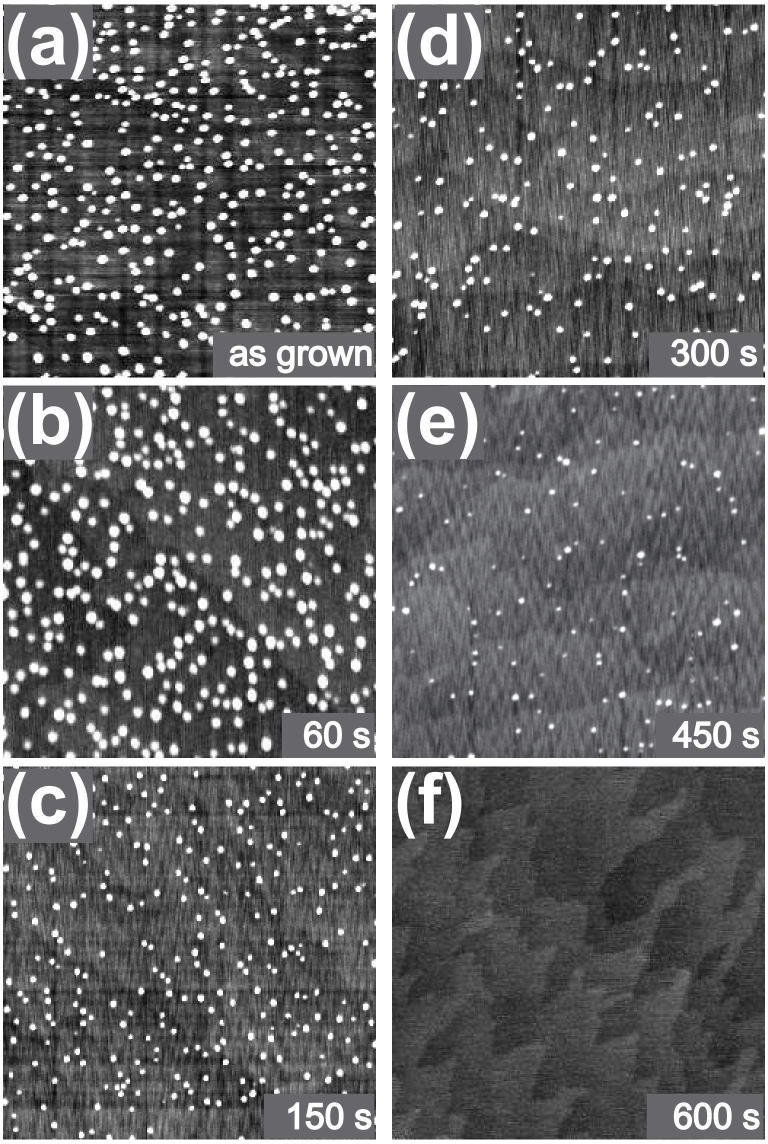

Figure 6.4: AFM images of 2.1 ML InAs deposited at 500 °C (a) before annealing, (b) post-growth annealing for 60 s, (c) 150 s, (d) 300 s, (e) 450 s, and (f) 600 s.

shown in AFM images, upon further annealing, the mean radius of quantum dots almost remains constant while the mean height slightly increases and the density of quantum dots decreases up to the dissolution of quantum dots. These facts indicate that the desorption of In cannot be attributed to the dissolution of quantum dots alone.

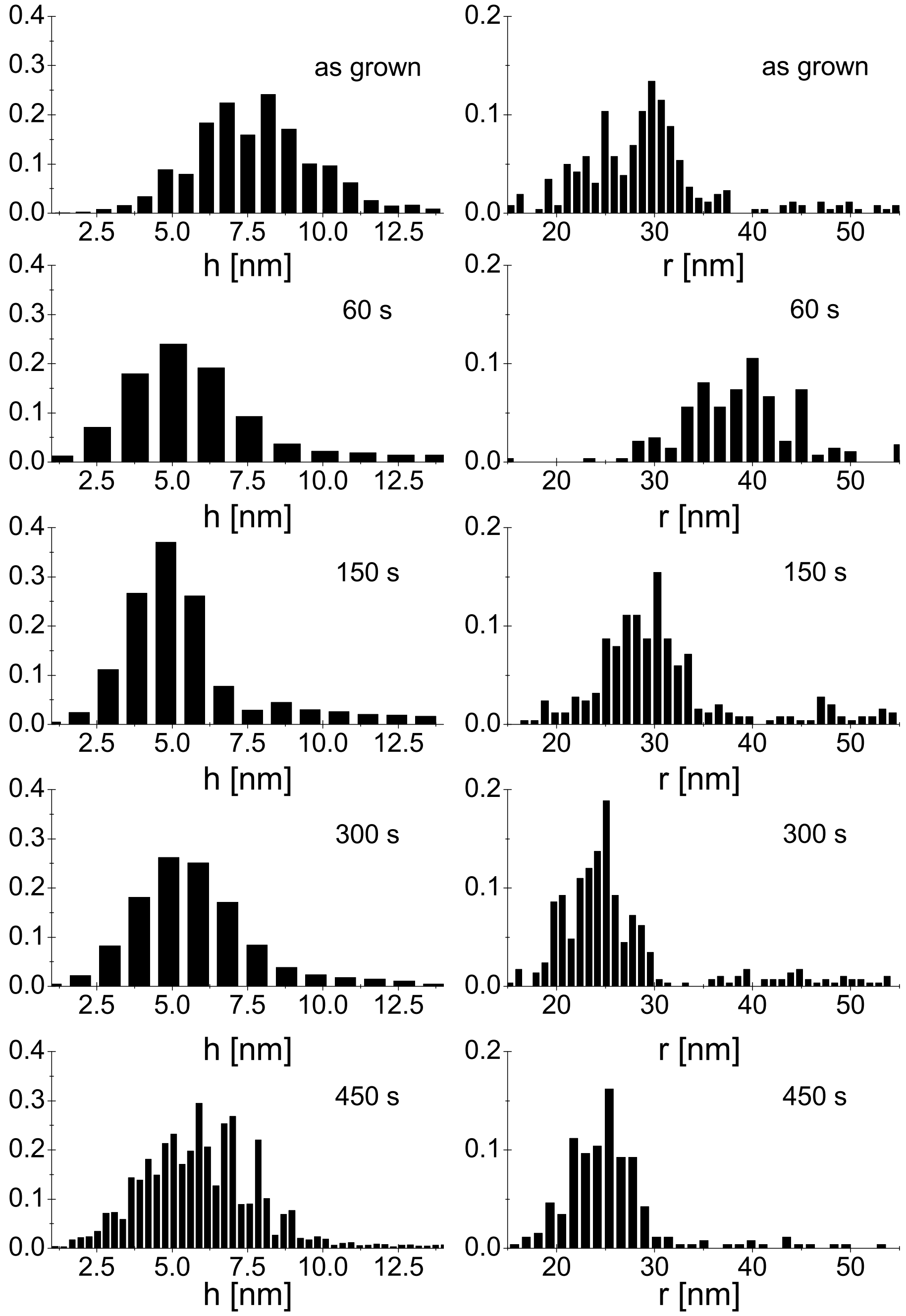

Figure 6.5: Distribution of the height(a) and the size(b) of InAs dots with annealing time annealed at 500 °C.

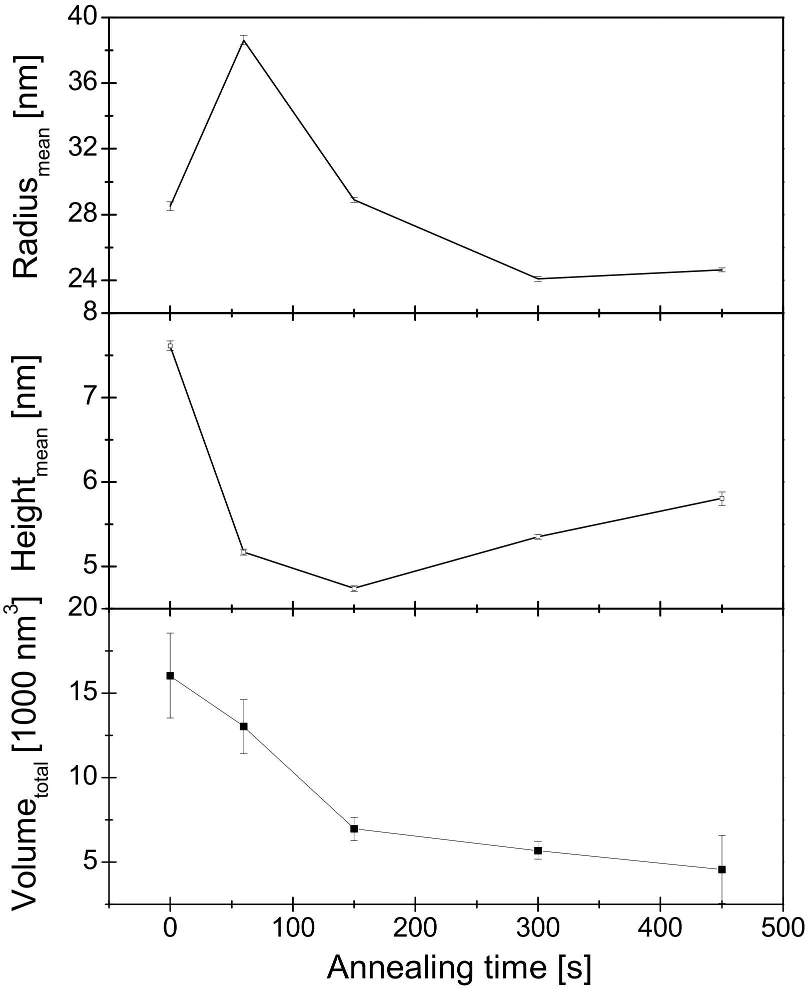

Figure 6.6: Evolution of the height(a) and the size(b) of the dots with annealing time.

According to the AFM images taken at different annealing stages and the film force curve, after 150 s annealing, In almost does not desorb. Furthermore, intermixing of GaAs with InAs has been established experimentally by many groups. For instance, it was found that the dot volume increases due to the additionally incorporated GaAs [78]. Further, it was found that interdiffusion has a pronounced effect on the dissolution of embedded InAs quantum dots in GaAs [79], but no report has been published thus far that investigates the influence of interdiffusion on the ripening of uncapped quantum dots.

6.3 Model

Ripening of particles, i.e. the growth of larger grains by dissolution of smaller grains, can be explained in the following way. For a supersaturated solid solution, to each degree of the supersaturation Δ of grains, there exists a critical radius $r_{cr} = \alpha/\Delta$ (α is a constant associated with the interphase surface tension) at which the grain is in equilibrium with the solution. When the particle radius is larger than the critical size, it grows. Otherwise it dissolves. Based on this fundamental theory for ripening of particles, considering interdiffusion between Ga and In, the unusual morphological evolution of the quantum dots annealed at 500 °C can be explained as the following. Typically, Δ is the concentration of In in the quantum dots and is typically constant. For annealing at high temperature of 500 °C, interdiffusion between Ga and In is strong [80]. At the beginning of annealing, the In concentration in the dots is high, leading to a small critical size. Ripening of dots can still be observed. With further annealing, due to desorption of In and interdiffusion between Ga and In, the In concentration decreases and the critical size increases. Eventually, the increase of critical size exceeds the increase of the dot size, i. e. $dr_{cr}/dt > dr/dt$. Dots with sizes smaller than the critical size shrink and eventually dissolve. After a certain time, the critical size becomes larger than the largest dot size, i. e. $r_{cr} > r$. At this point, all dots dissolve. This process is clearly seen in the AFM images taken at later annealing stages.

It should be emphasized that the desorption of In(As) at higher annealing temperature would accelerate the dot dissolution. A closer look on the results given by Heyn indicates that for the annealing conditions employed in this study, the lifetime of the dots is much longer than the annealing times used here. Therefore, the dissolution of the dots cannot be explained only by desorption of In. Note that the results coming from the film force curve of the quantum dots sample is consistent with AFM images taken at different annealing times. The film force drops drastically during first 180 s annealing, corresponding to the dots ripening and In desorption. As shown by AFM images in which the mean dot radius increases while the mean height decreases. With further annealing, the film force curve proceeds with a stable slope corresponds to the fact that desorption of In is insignificant. As shown in AFM images, the mean radius and mean height almost remain constant. Furthermore, the 0.8 N/m film force corresponds to 0.75 ML thick epitaxial InAs on GaAs(001) at this temperature. This means that only 33% of deposited 2.1 ML InAs are left. This amount of InAs is less than the amount of InAs in wetting layer (~1.5 ML), indicating that about 50% In in wetting layer goes into the dots and then desorbs. It is interesting to notice that the dot shape and size does not change much during annealing, but rather their density drops, as shown in Fig. 6.7. As mentioned above, it is expected that the In contents constantly drops during annealing. Therefore, this annealing procedure might open up a new possibility to control carefully the emission wavelength of the quantum dots while keeping the emission peak width small. Furthermore, since the density of the quantum dots drops to very low values, micro-photoluminescence measurements become possible without placing masks on the sample surface, which is known to possibly alter the quantum confinement due to a change of the Fermi level pinning at the surface. It was, however, not the intention in this study to proceed in these directions, but rather to confirm and to understand the involved ripening processes. Therefore, in the next section, the optical properties were investigated on a basic level and not with regard to device optimization or application.

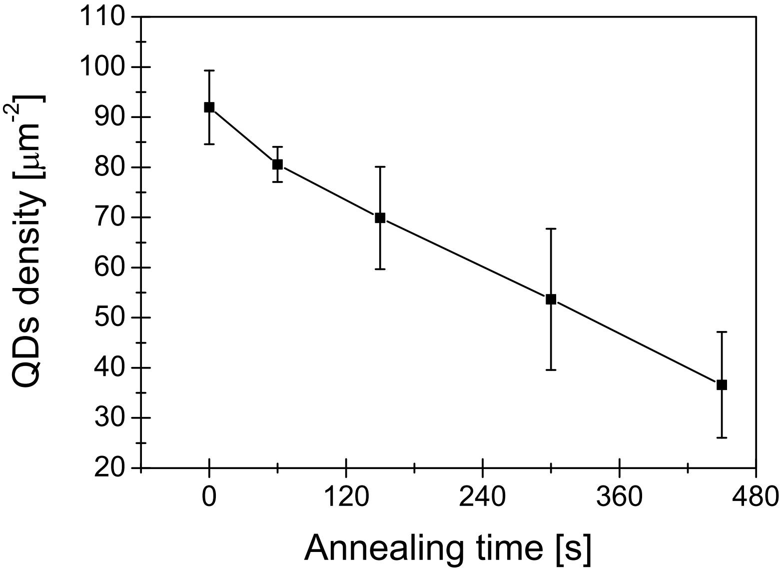

Figure 6.7: Evolution of the dot density with annealing time.

6.4 Optical properties

According to the new model above for the explanation of unusual annealing behavior of the InAs quantum dots annealed at 500 °C, it is interesting to investigate the optical properties of InAs quantum dots since a peak shift in the photoluminescence of the quantum dots is expected. For the PL measurements, a 50 nm GaAs capping layer was deposited immediately after the certain time annealing. The PL measurements were performed at 5 K. The results are shown in Fig. 6.8.

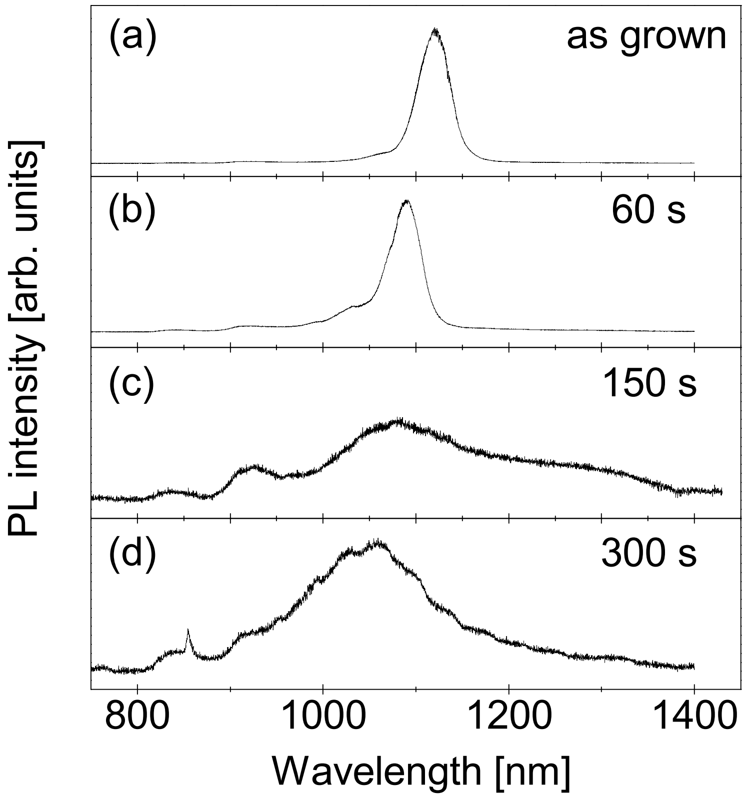

Figure 6.8: PL spectra measured at 5 K of 2.1 ML InAs deposited at 500 °C followed by annealing for (a) 0 s, (b) 60 s, (c) 150 s, and (d) 300 s.

For the as grown sample, the quantum dots' related peak is located at 1120 nm. After 60 s of annealing, the quantum dots' related peak shifts to 1087 nm. With further annealing, the peak position continuously shifts to 1071 nm and 1068 nm for annealing of 150 s and 300 s, respectively. For the sample annealed for 450 s, no peak is detectable with the instrument. This is due to very low density of quantum dots and it is out of the resolution of the PL setup. A plot of the peak position with annealing time is shown in Fig. 6.9. The wavelength shifts 33 nm after first 60 s of annealing. Compared to the wavelength shift obtained from annealing of 60 s to 150 s and from 150 s to 300 s - in these two cases, the wavelength changes by about 16 nm and 3 nm - though the annealing time 60 s is the shortest, the shift of PL peak is the largest. This is easy to be explained by the above model that the In concentration in the quantum dots is high once deposition stops. Thus, In desorbs fast at the beginning of annealing. With further annealing accompanied with a decrease in In concentration, In desorbs slower and slower. Therefore, the shift in the PL peak points becomes smaller and smaller.

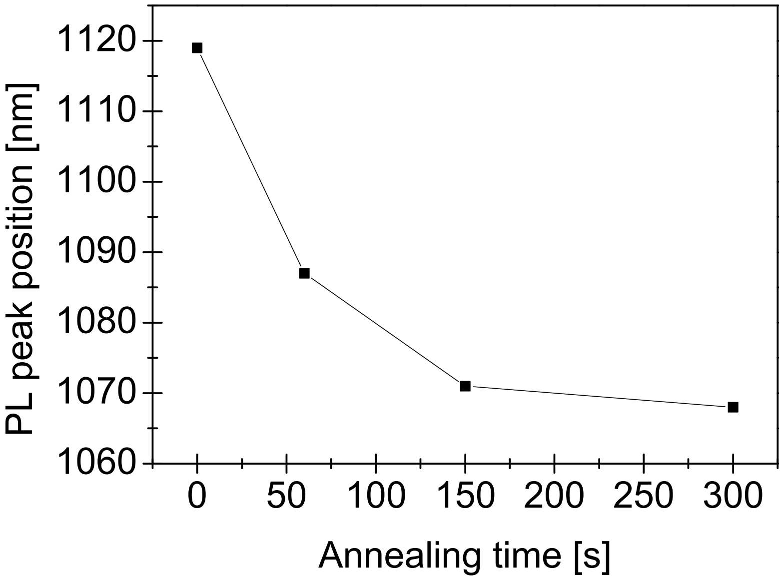

Figure 6.9: Variation of the position of the PL peaks of InAs quantum dots with annealing time annealed at 500 °C.

Note that the density of quantum dots decreases with annealing time, as shown in Fig. 6.7. Therefore, micro-PL can be directly performed on the sample and it is not necessary to mask part of the dots by a metal mask. This has a big advantage, since the deposition of a metal on the top surface changes the Fermi level alignment and therefore the band alignment in the dots. Thus, by not using this metal mask, the dots can directly be studied in an as-grown situation. For demonstration purposes, micro-photoluminescence spectra were recorded for a sample annealed for 300 s. The spectra were measured at 10 K and are shown in Fig. 6.10. The spectrum of a single dot is easily obtained and clearly visible. At a low exictation power, a single sharp peak corresponding to the ground state is visible (marked by X_S). With increasing laser power, the biexiton state (marked by XX_S) and the first excited state (marked by X_P) become visible, demonstrating that the fabrication of quantum dots via annealing at higher temperatures can allow for a detailed micro-photoluminescence investigation.

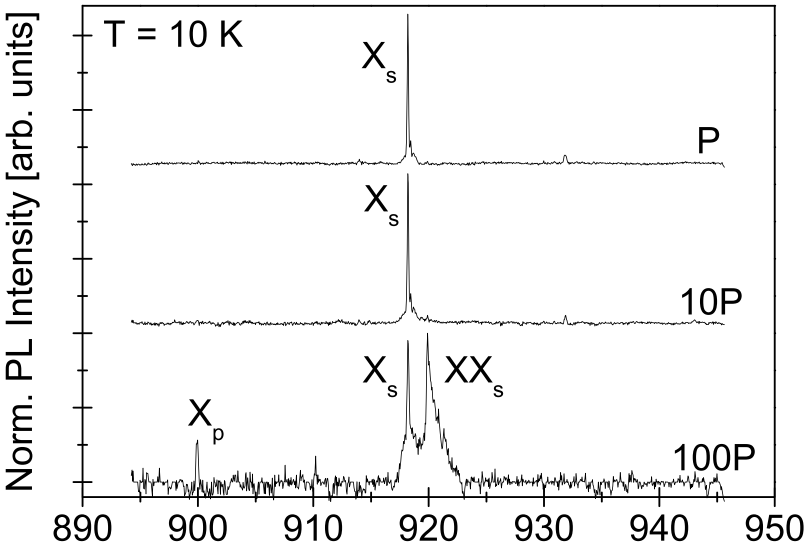

Figure 6.10: μ-PL spectra of a single InAs quantum dot with (a) low excitation power, (b) 10 times increased power, and (c) 100 times increased power.

6.5 Summary

The annealing behavior of InAs quantum dots on GaAs(001) at a high post growth annealing temperature was studied, namely 500 °C, using an *in-situ* cantilever beam measurement setup in combination with atomic force microscopy. The different evolution process comparing with quantum dots annealed at low temperatures can be explained by considering interdiffusion between Ga and In atoms and desorption of In. The eventual dissolution of quantum dots should be attributed to the interdiffusion between Ga and In. Photoluminescence of the samples at different annealing stages measured at 5 K corroborates the presented explanation. Annealing at high temperatures might open a new way to fabricate samples for micro-photoluminescence measurements due to the low dot density and the possibility to control the dot In composition while the dot shape and size remains constant.

Chapter 7

InAs growth on GaAs(001) under In-rich conditions

In contrast to the growth of InAs on GaAs(001) under As-rich conditions in which a morphological change from 2D to 3D takes place, the InAs film on GaAs(001) can be grown two dimensionally on the GaAs(001) surface within a narrow growth window. The restriction of In/As_4 flux ratio, substrate temperature, and deposition rate must be considered so that the growing front can reproduce the 4×2 symmetry. In this chapter, the stress evolution of InAs films grown under In-rich conditions is presented by using an *in-situ* cantilever beam setup to measure the film force curves.

7.1 Evolution of film force

The growth of InAs under In-rich conditions was performed in the same III-V semiconductor MBE chamber as the one in which InAs quantum dot was grown in the former chapters. The removal of oxide layer from GaAs(001) substrates and the growth of GaAs buffer layer were dealt with the same conditions as those which were used for InAs quantum dot growth. After GaAs buffer layer growth, the As pressure was decreased to be in the range of 8×10^{-8} - 2×10^{-7} mbar and the temperature of the substrates was kept at 470 °C and 500 °C, respectively.

Figure 7.1 shows AFM images of a 120 s deposition of InAs (nominal 6 ML thick) at 470 °C and 500 °C, respectively. The morphology of these two films are similar as observed by AFM. Both films are flat with long fingers directed along the [110] direction. This morphology remains the same with the longer deposition time, which was confirmed by obtaining AFM images for a sample that were deposited for 20 min. The same morphology was also obtained previously in the literature [81, 82, 83]. It is already well known that the morphology of mismatched system is related to the strain accumulated during growth. According to the morphology of InAs film grown under In-rich conditions, it is natural to get the idea to measure the film force in two perpendicular directions, i.e. the [110] and the [1$\bar{1}$0] directions. This was realized by cutting the GaAs(001) substrate such that the long edge is parallel to the [110] and the [1$\bar{1}$0] directions, respectively.

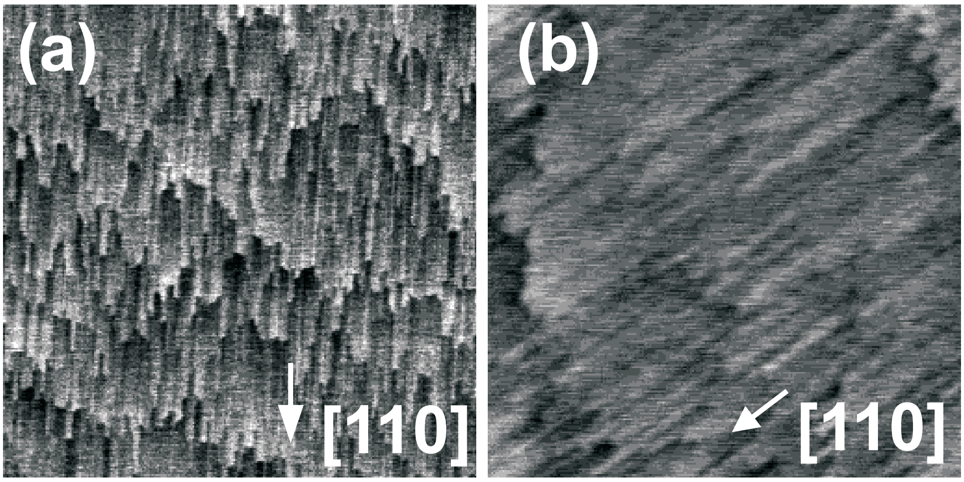

Figure 7.1: $2{\times}2\mu m^2$ AFM images of 120 s deposition of InAs with As pressure in the range of 8×10^{-8} - 2×10^{-7} mbar at (a) 470 °C and (b) 500 °C.

Figure 7.2 shows the two film force curves obtained during 1200 s growth of InAs on GaAs(001) measured along the [110] and the [1$\bar{1}$0] at 470 °C. The evolution of the film force is different along the [110] and the [1$\bar{1}$0] directions. A higher value of the film force is reached along the [110] direction as compared to the value of film force along the [1$\bar{1}$0] direction during deposition. For these curves, two stages of film force evolution can be distinguished. At the early deposition stage, the film force proceeds with a larger slope compared to the later one. The small curvature of the slope of film force at later deposition stage might be attributed to thermal drift or minor relaxation phenomena.

Carefully looking at the film force curves of the early deposition stage (Fig. 7.3), the film force along the [110] direction proceeds with a decreasing slope. The

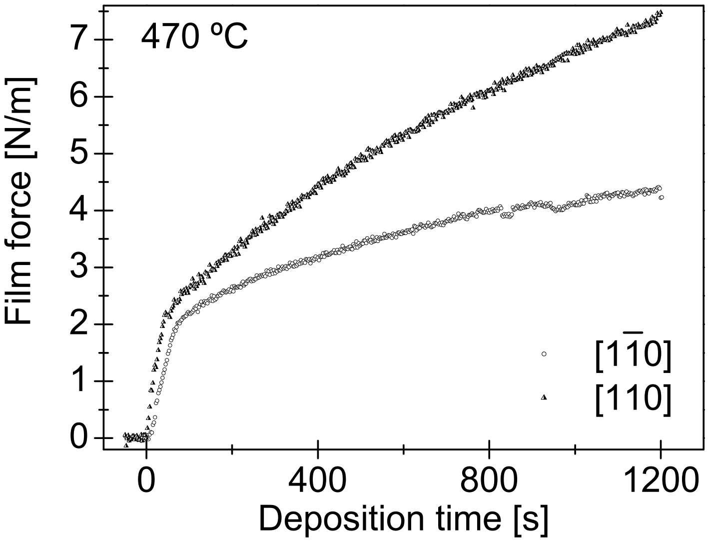

Figure 7.2: Film force curves during growth of InAs films on GaAs(001) with As pressure in the range of $8.0 \times 10^{-8} - 2.0 \times 10^{-7}$ mbar measured along two perpendicular directions [110] and [1$\bar{1}$0] at 470 °C.

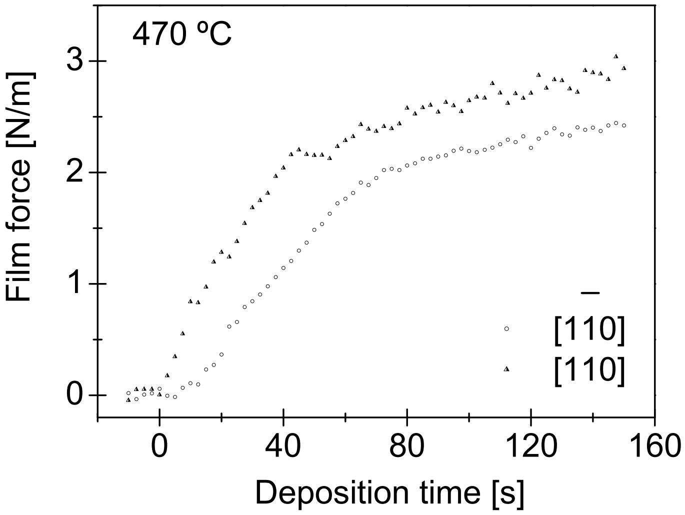

Figure 7.3: Magnified film force curves during early stage growth of InAs films on GaAs(001) at 470 °C.

slope continuously decreases till reaching a point where the stress is relaxed. After that the slope of film force becomes small and approximately remains constant. The decrease in the slope of the film force at the early stage cannot be attributed to thermal drift since the time scaler is very small, but is rather related to a real physical phenomenon. While the film force along the [110] direction proceeds with an increasing slope at the first 20 s deposition, it then remains constant till the stress relaxation point where the slope of film force drops and then approximately remains constant.

The same situation occurs to the film force curves measured at 500 °C except that the values of the film force are lower, as shown in Fig. 7.4 and 7.5. Note that the stress relaxation takes place earlier along the [110] direction than along the [1$\bar{1}$0] direction.

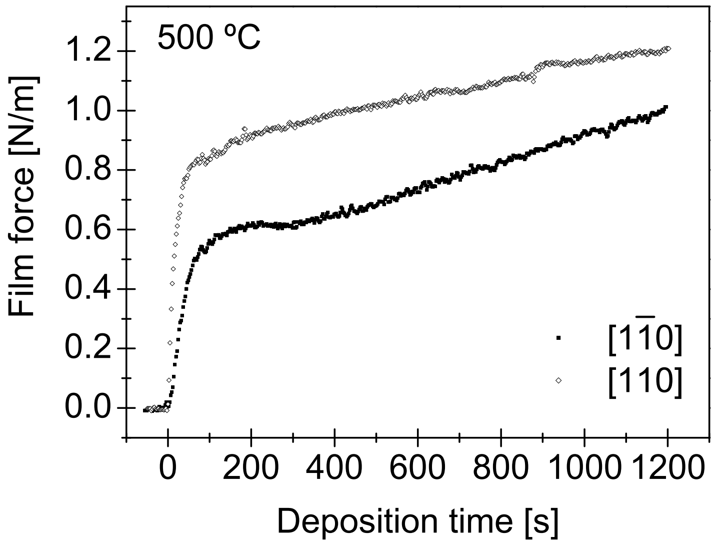

Figure 7.4: Film force curves during growth of InAs films on GaAs(001) with As pressure 1.0 $\times 10^{-8}$ mbar measured along two perpendicular directions [110] and [1$\bar{1}$0] at 500 °C.

A comparison of film force curves of InAs films grown at 470 °C under In-rich and As-rich conditions is given in Fig. 7.6 in the frame of film force versus deposition time. The reason for using deposition time is that the thickness of InAs film grown under In-rich conditions cannot be characterized with the techniques which were available in the present work due to the very

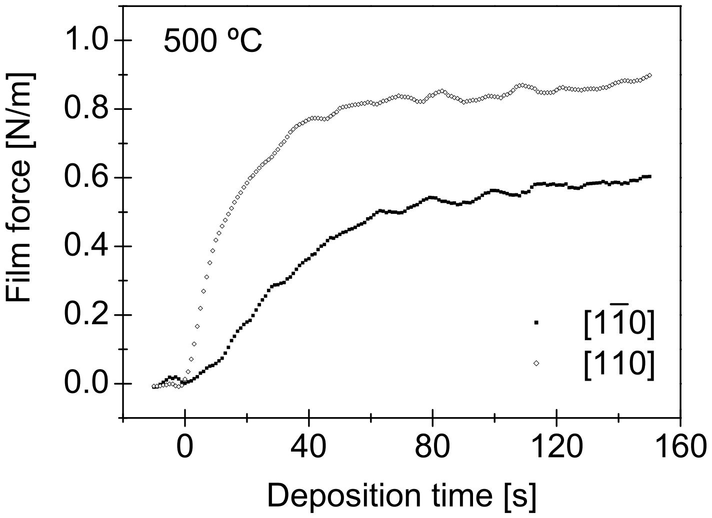

Figure 7.5: Magnified film force curves during early stage growth of InAs films on GaAs(001) at 500 °C.

thin film thickness in the case of growth under In-rich conditions. However, as expected the thickness of InAs films grown under In-rich conditions is thinner than the thickness grown under As-rich conditions with same deposition time. In droplets were observed on the samples grown under In-rich conditions although the In source temperature remained same at these two conditions. This indicates that almost all of the arriving In was incorporated into the InAs film in the case of growth under As-rich conditions while not all of In was incorporated into the InAs film in the case of growth under In-rich conditions and leads to the thinner thickness of InAs. According to this point of view, the stress of the InAs film grown under In-rich conditions along the [110] direction relaxes earlier than InAs film grown under As-rich conditions. However, as explained next, it is known that it is not clear that the stress relaxation of InAs film grown under In-rich conditions along the [1$\bar{1}$0] occurs earlier than InAs film grown under As-rich conditions or not.

For InAs on GaAs, the lattice mitfit is about 7.2%. In the case of InAs grown on GaAs(001) under In-rich conditions, this misfit still exists. For explaining the 2D layer by layer growth of InAs under In-rich conditions, Tournié et al. [84] used a model in which In is a virtual-surfactant. Snyder et al. [85] devoted the observed effects to the high surface tension and Bakhtizin et al. [81, 82] agreed with Snyder et al. They all found that the critical thickness

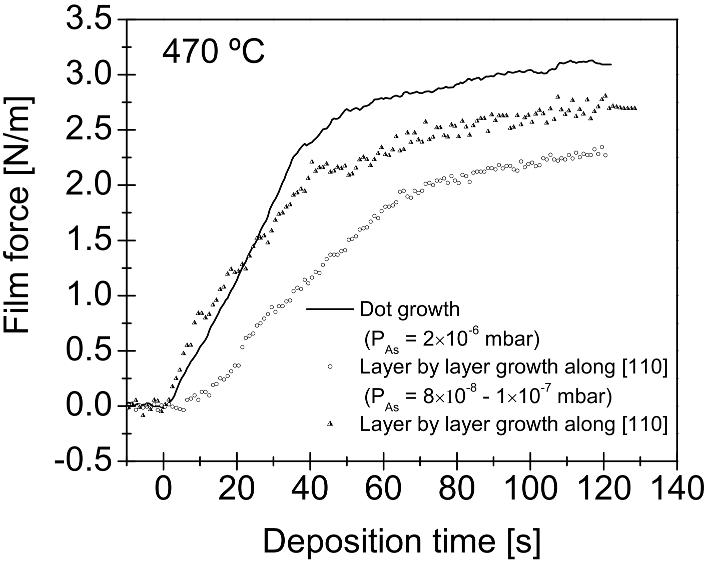

Figure 7.6: Comparison of film force curves during growth of InAs films on GaAs(001) at 470 °C under In-rich condition and As-rich condition.

for formation of dislocations increases in the case of InAs grown under In-rich conditions compared to the case of InAs grown under As-rich conditions. However, according to the results in this work, the stress was released early on during growth. Furthermore, the direction-dependence corresponds to the finger structure observed by AFM. A critical thickness for relaxation of the stress is also different along the [110] and the [$1\bar{1}0$] direction. The mechanism for relaxation of the elastic energy accumulated in the two dimensional epitaxial layer might therefore be best explained by the relaxation of surface stress as claimed by Trampert et al. [86] and Bakhtizin et al. [82], via a small relaxation of stress at the edges of each finger-like structure.

7.2 Summary

The stress evolution of InAs films grown under In-rich conditions is investigated by measuring the film force curves. The film force shows anisotropy along the [110] and the [$1\bar{1}0$] directions. The higher value of film force was reached along the [110] direction than along the [$1\bar{1}0$] direction. Furthermore, the stress relaxation occurs earlier along the [110] direction than along the [$1\bar{1}0$] direction as well as than in the case of the growth of InAs under As-rich conditions.

Chapter 8

Conclusions and outlooks

The stress evolution during the molecular-beam-epitaxy growth of InAs layer on GaAs(001) substrates was investigated by means of a cantilever beam measurement setup. Films that were grown under As-rich conditions and In-rich conditions were investigated. To complement the *in-situ* stress measurements, a range of *ex-situ* characterizations was performed. Mainly an atomic force microscopy was used to determine the morphology, a transmission electron microscopy was used to find and determine defects in the films and the photoluminescence was used to study the optical properties.

When InAs films were deposited under As-rich conditions, the well known Stranski-Krastanov growth mode was obtained, i.e. after the formation of a wetting layer, InAs quantum dots formed on the surface. A major part of this investigation dealt with the study of the stress evolution during the formation and especially during the subsequent annealing of these InAs quantum dots. While the stress was not directly measured, another quantity named film force was experimentally accessible through a cantilever beam setup. The stress is related to this quantity, namely it is the slope in a plot of the film force versus film thickness. During the growth of the InAs wetting layer, the observed stress is in reasonably good agreement with the theoretical misfit stress. When the quantum dots form, the stress is partially relieved. This stress relaxation process during the annealing phase was investigated at various temperatures.

For the annealing temperatures below 470 °C, the quantum dots showed standard Ostwald ripening behavior. However, the ripening processes take place temperature-dependently. By extending the ripening models existing in the literature to simulate the observed stress relaxation curves, a complete description of the ripening process was possible and it could even determine which process is the dominant one. For instance, at the lowest temperature investigated in this thesis (440 °C), the ripening process was mostly controlled by atom diffusion along the dot boundaries, while the ripening process at 470°C was governed by attachment/detachment on the dot surface. Compared to the typically employed procedure to determine the ripening process of quantum dots, the approach used in this thesis has several advantages. Typically, only the quantities such as an average dot radius are available from experiments, for instance from high resolution x-ray diffraction or atomic force/scanning force microscopy measurements. These quantities are then measured during ripening for a long time and then a power law is extracted. However, such an approach does not take into account that the dots may have complex shapes or the dot size distribution is multimodal. In contrast, the film force measured in this thesis contains the information of the whole dot ensemble, and therefore, an analysis of it will lead to a better determination of the mechanisms for the ripening process.

For annealing of dots at high temperatures, it was found that Ga-In interdiffusion and In desorption become dominant. Instead of observing standard ripening behavior, the dots grew first, then remained quite constant in the height and size while the density of dots dropped down to completely disappear. Using a combination of all experimental methods available for this work, it could be explained that the In content in each quantum dot dropped below a critical value for the dot stability. While the size and height distribution of the dots remained almost constant over long annealing time, the decrease in In content resulted in a well defined shift of the emission wavelengths of the dots. This opens up a new route for the control of the emission wavelengths of the group III alloy quantum dots, since the emission wavelength can be controlled simply by the annealing time. However, a disadvantage of such a method is the decrease in quantum dot density, and it is therefore required to create the stacked quantum dot layers. For InAs, it is well known that the dots align vertically, so one could imagine to use the above process to create a well defined first quantum dot layer, and then stacking enough additional quantum dot layers on the top to achieve a higher intensity. Another interesting application of the annealing procedure applies to more basic research. Since the dot density becomes very low at long annealing time, the dots are quite far separated. This allows one to perform micro-photoluminescence measurements without surface modification through a metal mask. Since again all remaining dots at a reasonably long annealing time have similar size, height and shape, but different In content, parallel studies on an individual quantum dot can be easily performed as was demonstrated by measuring a single dot in this thesis. For instance, the biexciton binding energy could then be determined as a function of the In content.

Besides investigating the As-rich growth of InAs on GaAs(001) and annealing behavior of the resulting quantum dots, In-rich growth of InAs on GaAs(001) were also studied preliminarily. Performing this study was complicated because of the narrow growth window and the difficulties in obtaining the uniform InAs films and the good RHEED images which were due to the measurement setup geometry. In order to achieve still the uniform samples, the growth area was further reduced and therefore resulted in a reduced signal to noise ratio. Nonetheless, it was found that the stress measured along the [110] direction is relieved earlier than in the Stranski-Krastanov growth mode. The surface morphology of these films showed the long finger structures and no formation of the 3D-like structures, and the mechanism for the stress relaxation might be best explained by the relaxation of the surface stress. Furthermore, it was also found that the stress was anisotropic. This can be explained by the difference in the surface diffusion constant of In along the different crystallographic directions. A detailed analysis, especially in a quantitative way, of these data requires however the additional measurements for which the current setup is not suitable. It would be highly desirable to be able to rotate the substrate during growth to achieve a better uniformity which would allow one to measure larger sample areas and to achieve a better signal to noise ration. Such a modification of the measurement setup was however outside the focus of this work and may be performed in subsequent studies.

Bibliography

[1] W. F. Brinkman and D. V. Lang. *Rev. Mod. Phys.*, 71:S480–S488, 1999.

[2] D. Leonard, K. Pond, and P. M. Petroff. *Phys. Rev. B*, 50:11687, 1994.

[3] N. N. Ledentsov, M. Grundmann, F. Heinrichsdorff, D. Bimberg, V. M. Ustinov, A. E. Zhukov, M. V. Maximov, Z. Alferov, and J. A. Lott. *IEEE J. Select. Topics Quantum Electron.*, 6:439, 2000.

[4] H. C. Liu, M. Gao, J. McCaffrey, Z. R. Wasilewski, and S. Fafard. *Appl. Phys. Lett.*, 78:79, 2001.

[5] D. Stiff-Roberts, S. Krishna, P. Bhattacharya, and S. Kennerly. *J. Vac. Sci. Tech., B*, 20:1185, 2002.

[6] M. Grundmann ed. *Nano-Optoelectronics.* Springer-Verlag, Berlin Heidelberg, 1st edition, 2002.

[7] M. A. Reed, R. T. Bate, K. Bradshaw, W. M. Duncan, W. M. Frensley, J. W. Lee, and H. D. Smith. *J. Vac. Sci. Technol. B*, 4(358):10891–10895, 1986.

[8] D. Bimberg, M. Grundmann, and N. N. Ledentsov. *Quantum Dot Heterostructures.* John Wiley & Sons, Chichester, 1998.

[9] W. J. Choi, J. D. Song, J. I. Lee, K. C. Kim, and T. G. Kim. *Physica B*, 376-377:886–889, 2006.

[10] L. Y. Karachinsky, T. Kettler, I. I. Novikov1, Y. M. Shernyakov, N. Y. Gordeev, M. V. Maximov, N. V. Kryzhanovskaya, A. E. Zhukov, E. S. Semenova, A. P. Vasil'ev, V. M. Ustinov, G. Fiol, M. Kuntz, A. Lochmann, O. Schulz, L. Reissmann, K. Posilovic, A. R. Kovsh, S. S. Mikhrin, V. A. Shchukin, N. N. Ledentsov, and D. Bimberg. *Semicond. Sci. Technol.*, 21:691–696, 2006.

[11] T. K. Sharma, M. Zorn, F. Bugge, R. Hülsewede, G. Erbert, and M. Weyers. *IEEE Photon. Technol. Lett.*, 14:887, 2002.

[12] N. Tansu, J. Y. Yeh, and L. J. Mawst. *Appl. Phys. Lett.*, 82:4038, 2003.

[13] J. R. Arthur. *Surf. Sci.*, 43:449, 1974.

[14] C. T. Foxon, M. R. Boudry, and B. A. Joyce. *Surf. Sci.*, 44:69, 1974.

[15] C. T. Foxon and B. A. Joyce. *Surf. Sci.*, 50:434, 1975.

[16] H. Kunzel and K. Ploog. *Appl. Phys. Lett.*, 37:416, 1980.

[17] C. G. Morgan, P. Kratzer, and M. Scheffler. *Phys. Rev. Lett.*, 82:4886, 1999.

[18] A. Kley, P. Ruggerone, and M. Scheffler. *Phys. Rev. Lett.*, 79:5278, 1997.

[19] E. S. Tok, J. H. Neave, J. Zhang, B. A. Joyce, and T. S. Jones. *Surf. Sci.*, 374:397, 1997.

[20] P. Kratzer, C. G. Morgan, and M. Scheffler. *Phys. Rev. B*, 59:15246, 1999.

[21] P. Kratzer, C. G. Morgan, and M. Scheffler. *Prog. Surf. Sci.*, 59:135, 1998.

[22] K. R. Evans, C. E. Stutz, D. K. Lorance, and R. L. Jones. *J. Crystal Growth*, 95:197, 1989.

[23] C. T. Foxon and B. A. Joyce. *Surf. Sci.*, 64:293, 1977.

[24] P. Kratzer, E. Penev, and M. Scheffler. *Appl. Phys. A*, 75:79–88, 2002.

[25] J. Zhang, E. M. Gibson, C. T. Foxon, and B. A. Joyce. *J. Cryst. Growth*, 111:93–97, 1991.

[26] H. Yang, V. P. LaBella, D. W. Bullock, Z. Ding, J. B. Smathers, and P. M. Thibado. *J. Cryst. Growth*, 201/202:88–92, 1999.

[27] B. A. Joyce, D. D. Vvedensky, A. R. Avery, J. G. Belk, H. T. Dobbs, and T. S. Jones. *Appl. Surf. Sci.*, 130-132:357, 1997.

[28] T. Hashizume, Q. K. Xue, J. Zhou, A. Ichimiya, and T. Sakurai. *Phys. Rev. Lett*, 73:2208, 1994.

[29] A. R. Avery, C. M. Goringe, D. M. Holmes, J. L. Sudijono, and T. S. Jones. *Phys. Rev. Lett*, 76:3344, 1996.

[30] J. Zou, X. Z. Liao, D. J. H. Cockayne, and R. Leon. *Phys. Rev. B*, 59: 12279, 1999.

[31] A. Rosenauer, U. Fischer, D. Gerthsen, and A. Förster. *Appl. Phys. Lett.*, 71:3868, 1997.

[32] B. A. Joyce, D. D. Vvedensky, G. R. Bell, J. G. Belk, M. Itoh, and T. S. Jones. *Mater. Sci. Eng.*, B67:7–16, 1999.

[33] J. G. Belk, J. L. Sudijono, D. M. Holmes, C. F. McConville, T. S. Jones, and B. A. Joyce. *Surf. Sci.*, 365:735–742, 1996.

[34] J. G. Belk, C. F. McConville, J. L. Sudijono, T. S. Jones, and B. A. Joyce. *Surf. Sci.*, 387:213–226, 1997.

[35] B. A. Joyce, J. L. Sudijono, J. G. Belk, H. Yamaguchi, X. M. Zhang, H. T. Dobbs, A. Zangwill, D. D. Vvedensky, and T. S. Jones. *Jpn. J. Appl. Phys.*, 36:4111–4117, 1997.

[36] B. A. Joyce, D. D. Vvedensky, A. R. Avery, J. G. Belk, H. T. Dobbs, and T. S. Jones. *Appl. Surf. Sci.*, 130-132:357–366, 1998.

[37] Y. Garreau, K. Aïd, M. Sauvage-Simkin, R. Pinchaux, C. F. McConville, T. S. Jones, J. L. Sudijono, and E. S. Tok. *Phys. Rev. B*, 58:16177–16185, 1998.

[38] B. A. Joyce, D. D. Vvedensky, T. S. Jones, M. Itoh, G. R. Bell, and J. G. Belk. *J. Cryst. Growth.*, 201/202:106–112, 1998.

[39] P. B. Joyce, T. J. Krzyzewski, G. R. Bell, A. A. Joyce, and T. S. Jones. *Phys. Rev. B*, 58:R15981–R15984, 1998.

[40] J. F. Nye. *Physical properties of Crystals.* Oxford: Oxford University Press, 1985.

[41] H. Ibach. *Surf. Sci. Rep*, 29:193, 1997.

[42] W. A. Brantley. *J. Appl. Phys.*, 44:534, 1973.

[43] F. C. Frank and J. Van der Merwe. *Proc. Roy. Soc.*, A198:216–225, 1949.

[44] C. A. B. Ball and J. H. van der Merwe. *Dislocations in solids.* Elsevier Science Publishing Company, North Holland, f. r. n. nabarro edition, 1983.

[45] J. W. Matthews. *Coherent interfaces and misfit dislocations, in Epitaxial growth, Part B.* Academic Press, New York, j. w. matthews edition, 1975.

[46] J. W. Matthews. *J. Vac. Sci. Techol.*, 12:126–133, 1975.

[47] W. Ostwald. *Z. Phys. Chem.*, 34:495, 1900.

[48] G. W. Greenwood. *Acta metall*, 4:243, 1956.

[49] I. M. Lifshitz and V. V. Slezov. *J. Phys. Chem. Solids*, 19:35, 1959.

[50] I. M. Lifshitz and V. V. Slezov. *Soviet Phys. Jetp*, 35:331, 1959.

[51] C. Wagner. *Z. Electrochem.*, 65:581, 1961.

[52] P. W. Voorhees. *Annu. Rev. Mater. Sci.*, 22:197, 1992.

[53] R. D. Vengrenovitch. *Acta metall.*, 30:1079, 1982.

[54] R. D. Vengrenovich, Yu. V. Gudyma, and S. V. Yarema. *Semiconductors*, 35:1378, 2001.

[55] J. E. Mahan, K. M. Geib, G. Y. Robinson, and R. G. Long. *J. Vac. Sci. Technol*, A 8:3692, 1990.

[56] W. Braun. *Applied RHEED.* Springer-Verlag, Berlin and Heidelberg, 1st edition, 1999.

[57] A. Ichimiya and P. I. Cohen. *Reflection High Energy Electron Diffraction.* Cambridge University Press, Cambridge CB2 2RU, UK, 1st edition, 2004.

[58] J. Wollschläger, J. Falta, and M. Henzler. *Appl. Phys. A*, 50:57, 1990.

[59] G. G. Stoney. *Proc. R. Soc.*, 32:172, 1909.

[60] A. J. Schell-Sorokin and R. M. Tromp. *Phys. Rev. Lett.*, 64:1039, 1990.

[61] R. E. Martinez, W. M. Augustyniak, and J. A. Golovchenko. *Phys. Rev. Lett.*, 64:1035, 1990.

[62] D. Sander, A. Enders, and J. Kirschner. *Rev. Sci. Instrum.*, 66:4743, 1995.

[63] R. Abermann and R. Koch. *Thin. Solid Films*, 129(1-2):71–78, 1985.

[64] J. A. Floro and E. Chason. *Appl. Phys. Lett.*, 69(25):3830–3832, 1996.

[65] A. Brenner and S. Senderoff. *J. Res. Nat. Bur. Stand.*, 42:105, 1949.

[66] P. M. Marcus. *Surf. Sci.*, 366:219, 1996.

[67] P. M. Marcus. *Phys. Rev. B*, 53:7460, 1996.

[68] P. M. Marcus. *J. Mag. Mag. Mat.*, 168:18, 1997.

[69] W. Lai and E.Saibel. *Elements of Mechanics of Elastic Solids.* Addison-Wesley, Massachusetts, 1st edition, 1965.

[70] Yu. A. Burenkov, S. Yu. Davydov, and S. P. Nikanorov. *Sov. Phys. Solid State*, 17(7):1446–1447, 1975.

[71] J. M. García, J. P. Silveira, and F. Briones. *Appl. Phys. Lett.*, 77:409, 2000.

[72] R. P. Mirin, A. Roshko, and M. van der Puijl. *J. Vac. Sci. Technol. B*, 20:1489, 2002.

[73] D. J. Bottomley. *Appl. Phys. Lett.*, 72:783, 1998.

[74] K. Poetschke, L. Mueller-Kirsch, R. Heitz, R. L. Sellin, U. W. Pohl, D. Bimberg, N. Zakharov, and P. Werner. *Physica. E*, 21:606, 2004.

[75] T. J. Krzyzewski and T. S. Jones. *J. Appl. Phys.*, 96:668, 2004.

[76] Ch. Heyn. *Phys. Rev. B*, 66:075307, 2002.

[77] H. Lee, R. R. Lowe-Webb, W. D. Yang, and P. C. Sercel. *Appl. Phys. Lett.*, 71:2325, 1997.

[78] B. A. Joyce, T. S. Jones, and J. G. Berk. *J. Vac. Sci. Technol. B*, 16: 2373, 2005.

[79] B. Lita, R. S. Goldman, J. D. Phillips, and P. K. Bhattacharya. *Surf. Rev. Lett.*, 7:539, 2000.

[80] P. B. Joyce, T. J. Krzyzewski, G. R. Bell, B. A. Joyce, and T. S. Jones. *Phys. Rev. B*, 58:15981, 1998.

[81] Q. K. Xue, Y. Hasegawa, T. Ogino, H. Kiyama, and T. Sakurai. *J. Vac. Sci. Technol. B*, 15(4):1270–1273, 1997.

[82] R. Z. Bakhtizin, Y. Hasegawa, Q. K. Xue, and T. Sakurai. *J. Experimental and theoretical Physics*, 91(5):1153–1166, 2000.

[83] K. G. Eyink, K. Mahalingam, J. Pitz, H. Smith, and L. Grazulis. *J. Vac. Sci. Technol. B*, 22(4):2261–2265, 2004.

[84] E. Tournié and K. H. Ploog. *Thin Solid Films*, 231:43–60, 1993.

[85] C. W. Snyder and B. G. Orr. *Appl. Phys. Lett.*, 62(1):46–48, 1993.

[86] A. Trampert, E. Tournié, and K. H. Ploog. *Appl. Phys. Lett.*, 66(1): 2265, 1995.

Acknowledgements

I received help, encouragement and support from many people during the course of my thesis work. It is my pleasure to express my gratitude especially to the following persons...

.....Prof. Dr. Klaus H. Ploog for giving me the opportunity to work at Paul-Drude Institute, for his continued interest in my work and for providing the financial means during my stay at PDI. It is an honor that I can finish this work under his guidance.

.....Prof. Dr. W. Ted Masselink and Prof. Dr. Eric Tournié for taking their valuable time to review this work.

.....Dr. D. M. Schaadt for his consistent help, support and constant encouragement throughout this work.

.....Dr. T. Hesjedal for his kindness to give me tips on how to present my work and for useful discussions. I also thank him for his non-scientific help.

.....Ms S. Kraus for her technical help on the MBE system.

.....Dr. A. Trempert for his invaluable help and discussions during TEM measurements.

.....Dr. L. Schrottke and Dr. S. L. Lu for their kindness and help on the PL measurements.

.....Dr. O. Brandt and Dr. M. Ramsteiner for their help on micro-PL measurements and useful discussions.

.....Dr. R. Hey for his discussions and tips related to the MBE growth of InAs and GaAs. His patience and kindness constantly encourages me.

.....Dr. A. Das for his discussions and friendliness.

.....Dr. A. Koch for his encouragement.

.....Our librarians Mrs. D. Dormeyer, Mrs. S. Räther for their help in getting old articles and books.

.....Mrs. P. Grasnick for her help for everything starting from my arrival till my leaving. I would like to thank Mr. J Schönberg for his help with computers.

.....My Ph.D. colleagues, namely Dr. R. Engel-Herbert, Dr. G. Mußler, Dr. D. K. Satapathy, and Dr. J. Mohanty for many discussions and non-scientific suggestions.

.....My friends. Though they are spread all over the world, they encouraged me by calling or email during my work.

.....Lastly, my deep appreciation goes to my parents and my sisters. Their patience, love, sacrifice and support is beyond words.

Hier folgt dann eine Danksagung.

Curriculum vitae

Name: Dongzhi Hu

Birthday: 2nd October 1971

Birth place: Inner Mongolia, China

11.2002–07.2006	Ph.D. student Humboldt-University at Berlin and Paul-Drude Institute for solid state electronics Supervisor: Prof. Dr. K. H. Ploog
06.2002	Master of Condensed Matter Physics Department of Physics Fudan University, Shanghai, China.
08.1995–10.2002	Faculty Surface Physics Laboratory Fudan University, Shanghai, China.
07.1995	Bachelor of Physics Department of Physics Fudan University, Shanghai, China.
09.1991–07.1995	Undergraduate student Department of Physics Fudan University, Shanghai, China.
09.1990–07.1991	Military sevice Dalian army military college

Selbständigkeitserklärung

Hiermit erkläre ich, die vorliegende Arbeit selbständig ohne fremde Hilfe verfaßt und nur die angegebene Literatur und Hilfsmittel verwendet zu haben.

Dongzhi Hu

31. August 2006